SAND STATE AND PERFORMANCE ANALYSIS OF MICROPILES

By

SHANZHI SHU

A thesis submitted in partial fulfillment of
the requirements for the degree of

DOCTOR OF PHILOSOPHY IN CIVIL ENGINEERING

WASHINGTON STATE UNIVERSITY
Department of Civil and Environmental Engineering

December 2005

To the Faculty of Washington State University:

The members of the Committee appointed to examine the thesis of SHANZHI SHU find it satisfactory and recommend that it be accepted.

_____
Chair

_____

_____

_____

ACKNOWLEDGEMENT

First of all, I would like to express my great appreciation to Dr.Balasingam Muhunthan for his irreplaceable encouragement, guidance and support. He has been an inspiration to me since I started to apply for admission to Washington State University. A person of myriad skills, he has eased the way of my work by his wonderful contribution.

I would also like to express my thanks to Dr. X. S. Li at Hong Kong University of Science and Technology, for his help in my formulating the state dependent bounding surface sand model, Dr. Z. L. Wang at Geomatrix, for his beneficial discussion and instruction regarding bounding surface model and its implementation into FLAC, Dr. Edward Dzik at HCITASCA for his help in troubleshooting of FLAC3D and the constitutive model implementation, Drs. Jacques Garnier and Christophe Gaudin at LCPC, France, and Dr. H. Y. Ming, at Shenzhen University, China for his assistance in my coding the model. I wish to thank Drs. Adrian Rodriguez-Marek, Rafik Itani and William Cofer for serving in my committee.

The friendship and collaboration with a number of my fellow students has been invaluable. Especially Mr. Sasiharan provided lots of help with my research and finalization of my dissertation.

Financial support by the Federal Highway Administration and Washington State Department of Transportation is acknowledged with gratitude.

Last but certainly not least, I would like to express my deepest gratitude for the constant support, understanding, and love that I received from my wife Fang, my daughter Wendy and my family during the study.

SAND STATE AND PERFORMANCE ANALYSIS OF MICROPILES

Abstract

by SHANZHI SHU, Ph.D.
Washington State University
December 2005

Chair: Balasingam Muhunthan

The incomplete description of the state of sand in current micropile design and past full scale tests have resulted in a number of anomalous results. A state dependent bounding surface sand constitutive model within the framework of critical state soil mechanics is formulated here. The constitutive model is coded with C++ and implemented into the finite difference geotechnical software FLAC3D. The model and its implementation are verified by using laboratory triaxial tests on Toyoura, Ottawa, and Fontainbleau sands.

The performance of single, vertical group, and inclined network piles installed in sands with different initial state is studied systematically using the state dependent constitutive model. The finite difference grid in FLAC 3D for pile arrangement with the state dependent sand model was first validated using a full scale test on a micropile group on Fontainbleau sand. The FLAC3D model was then used to study the effect of key variables that control the performance of micropiles.

The results show that the side resistance of micropiles is influenced by the initial normal stress applied to the pile and its positive increment by shear induced dilation of

dilative sand and negative increment due to contraction of contractive sand. The load transfer in a group of piles is controlled by two mechanisms: one due to overlap of stresses induced by adjacent piles, and the other due to dilatancy. Overlap of shear stresses as determined by pile spacing might lead to a positive group effect on side resistance. Shear induced dilation in dilative sands contributes to a positive group effect on side resistance in bored piles with well developed interfaces; however its effect is negative for contractive sand. Both mechanisms contribute positively to the group effect on tip resistance. The studies also show that the effect of inclination on pile resistance is affected by the sand state. When considered as structure elements, outward inclined network pile groups have higher resistance than inward inclined pile groups.

TABLE OF CONTENTS

Page

LIST OF TABLES

Page

LIST OF FIGURES

Page

CHAPTER 1

INTRODUCTION

1.1 General

Bridges, road embankments, and viaduct infrastructure require sound performance of deep foundations. The increase in static and seismic loading demands imposed by codes in recent years has resulted in the need to retrofit many of the existing deep foundations. The selection of the type of retrofit is often influenced by site constraints such as limited access, overhead clearance, proximity to sensitive facilities, and the presence of hazardous materials in soils.

Micropiles are increasingly being used to retrofit deep foundations. This is due in part to their small boring diameter, which allows their construction with smaller equipment than those used for traditional piles. Micropiles can also be installed in almost any ground condition (Mascardi, 1982). In the current state of practice, micropiles are often installed in a group pattern with vertical elements. Installation of micropiles in a network pattern with some or all inclined members has also been advocated (Lizzi, 1982).

Experimental results of laboratory and full-scale experiments reported by various investigators indicate significantly different and apparently contradictory group effects on micropile as well as conventional pile systems (Lo, 1967; Vesic, 1969; O'Neil, 1983; Lizzi and Carnevale, 1979; Plumelle, 1984; and FOREVER, 2002). Lizzi and Carnevale (1979) showed a dramatic positive group effect (220%) on the capacity of reticulated micropile networks over those vertically installed micropile groups with the same number of piles with identical dimensions. This dramatic increase was not observed by other full-

scale experiments conducted to reexamine the results of Lizzi (FOREVER 2002). Many past field experiments on displacement piles have also shown positive as well as negative effects on bearing capacity (Bustamante & Gianeselli, 1993; Brown & Drew, 2000; NeSmith, 2002).

It is believed that the disagreements described above on the behavior of group and network piles are in part due to not accounting for the state of sand in the different test programs and in the interpretation of their results. Most full-scale tests replicate the sand with its field relative density (or the void ratio). Such replication is insufficient to account for the important effects of confinement stress and the fabric of sand (geometric arrangement of particles and voids). The manner and installation of micropile elements would affect the existing state of sand. Thus, it would be difficult to compare the results of laboratory and full-scale experiments from a unified perspective, without accounting for the state of sand.

Numerical analysis is an effective way to study the behavior of micropiles as, once a model is verified, conditions can be changed with little effort to conduct a parametric study on the system variables. Foerster and Modaressi (1995), Estephan and Frank (2001), Sadek (2002), and Sadek & Shahrour (2004) have performed numerical analyses of micropiles under various conditions. Most of them have, however, not focused on the effects of sand state on the performance of a micropile, group, or network.

A constitutive model with explicit accounting of the soil state is needed in order to numerically analyze soil resistance to micropiles under different initial soil states. The concept of critical state (Roscoe et al., 1958) has been successfully applied to modeling the behavior of cohesive soils. However, many studies have shown that it is very limited

for applications in sand because, unlike clay, sand does not possess a unique relationship between the void ratio *e* and effective confining pressure *p* for a particular stress ratio $\eta=q/p$ in triaxial testing (Manzari and Dafalias 1997).

A comprehensive bounding surface sand model has been formulated within a critical-state framework by Li (2002). The state parameter ψ (Been & Jefferies, 1985) expressed as the difference between the current void ratio and the void ratio at the critical state at the same confining pressure was explicitly incorporated into this model. The model assumes the dilatancy of a granular soil to be dependent not only on the stress ratio $\eta=q/p$, where q and p are the deviatoric and mean effective normal stresses respectively, but also on the state parameter. It has the potential to capture the effects of sand state on the performance of micropiles.

This study uses the widely used commercial 3-dimensional geotechnical software FLAC3D developed by HC Itasca to study micropile and group network performance. The user interface feature of FLAC3D is used to incorporate the state based constitutive sand model.

1.2 Objectives and Scope of Study

The objectives of this study are to:

1. Formulate a state parameter based constitutive model for sand behavior.
2. Implement the constitutive model into FLAC3D.
3. Verify the model using laboratory element and model tests on micropiles, and
4. Use the FLAC3D model to investigate the effects of sand state on the performance of single, group, and network micropiles.

1.3 Organization of the Thesis

Chapter 2 presents a review of the current state of performance of micropiles. Classification and the type of applications of micropiles are reviewed. Previous results Studies on group effect of micropiles and piles conducted by are summarized. The review also includes the state of research on network effects and displacement effects of micropiles.

The basic framework of critical state soil mechanics is briefly presented in Chapter 3. Concepts such as the critical state, dilative, and contractive behavior and state parameter are introduced. The relationship between resistance of piles and state parameter of sand are discussed.

Chapter 4 presents details of the state parameter based model formulated in the study. It is a critical state soil mechanics based bounding surface sand model (Li & Dafalias, 2000; Li, 2002). The basic features of the bounding surface plasticity theory and an early version of the model is presented in Appendix A. Chapter 4 is completed with the presentation on the determination of the model parameters.

The implementation of the constitutive model into FLAC3D is detailed in Chapter 5. The Explicit, Dynamic Solution (EDS) scheme used in Itasca series software is introduced. The mechanical time step for numerical stability and mixed discretization technique are presented as well. The procedures of implementation of the model into FLAC3D are provided. The listing of the constitutive code in the C++ language is provided in Appendix B.

The verification of the FLAC3D model is presented in Chapter 6. The model is used to simulate element test results in the laboratory as well as the load displacement characteristics of a model test conducted by the FOREVER program.

FLAC3D with the new constitutive model is used in Chapter 8 to simulate the state dependent performance of micropiles under vertical load. The analyses are subsequently extended to study the effect of spacing and initial state on the performance of groups of piles and network groups of piles.

A summary and findings of the study as well as some recommendations for further research are presented in Chapter 8.

CHAPTER 2

MICROPILES: STATE OF PERFORMANCE

2.1 Micropiles

Micropiles are defined as small diameter, drilled, cast-in-place, or grouted piles that are typically reinforced. It is widely assumed that the range of diameter of micropiles is limited to less than 300 mm.

Micropiles can withstand axial and/or lateral loads, and may be considered as a substitute for conventional piles or as one component in a composite soil/pile mass, depending upon the design concept employed. Due to its relatively large flexibility, it can be effective in resisting seismic loads. Construction of micropiles is less limited by site conditions, so they can be effective for underpinning.

Most of the applied load on conventional cast-in-place replacement piles is structurally resisted by the reinforced concrete; increased structural capacity is achieved by an increase in cross-sectional and surface areas. Micropiles, by comparison, structurally derive a large portion of their stiffness and strength from high capacity steel reinforcement elements, which may occupy as much as 50% of the bore volume (Misra & Chen, 2004). The special drilling and grouting methods used in micropile installation allow for high grout/ground bond values along the interface. The grout transfers the load through friction from the reinforcement to the ground in the micropile bond zone in a manner similar to that of ground anchors. Due to the small pile diameter, the end-bearing contribution in micropiles is generally neglected. Primarily, the ground type and grouting method used, i.e., pressure grouting or the gravity feed, influences the grout/ground bond

strength achieved. The role of the drilling method is also influential, although less well quantified (Sharma, 2001).

A major advantage when using micropiles for underpinning is that the system can be designed to have very low settlements. The earliest piles were constructed with diameters of 100 mm and they were tested to loads of more than 400 kN with no record of grout-ground interfacial failures (Bruce et al. 1995). It is common for these piles to develop settlements on the order of a few millimeters or less under working loads. Under these conditions, its bearing capacity is not fully mobilized (Ellis 1985). Another advantage when using micropiles for underpinning is that the drilling and grouting procedures used to construct a micropile induces much less vibration and reduces adverse effects to a structure compared with other conventional pile installation techniques. Micropiles can be installed with as little as 1.5 m headroom if casing for drilling is used in short segments that can be screwed together (Ellis 1985)

Primary applications of micropiles can be classified into two main categories:

A. *As Structural Support*

- Foundation for new structures
- Seismic retrofitting
- Underpinning of existing foundation
- Repair / Replacement of existing foundations
- Arresting / Prevention of movement
- Upgrading of foundation capacity

B. *For In Situ Reinforcement*

- Embankment, slope and landslide stabilization
- Soil strengthening and protection

- Settlement reduction
- Structural stability.

The current micropile classification system is based on two criteria: i) philosophy of behavior (design) and ii) method of grouting (construction). The philosophy of behavior dictates the method employed in designing the micropile. The method of grouting defines the grout/ground bond capacity, which is generally the major constructional control over pile capacity.

Design philosophy

The design of an individual or group of micropiles differs greatly from that of a network of closely spaced reticulated micropiles. This led to the definition of CASE 1 micropile elements, which are loaded directly and where the pile reinforcement resists the majority of the applied load (Figure 2-1). CASE 2 micropile elements circumscribe and internally reinforce the soil to make a reinforced soil composite that resists the applied load (Figure 2-2).

CASE 1 micropiles can be used as substitutes for more conventional types of piles to transfer structural loads to a deeper, more competent or stable stratum. Such directly loaded piles, whether for axial or lateral loading conditions, are referred to as CASE 1 elements. The load is primarily resisted structurally by the steel reinforcement and geotechnically by the grout/ground bond zone of the individual piles. At least 90 percent of all international applications to date, and virtually all of the projects in North America have involved CASE 1 micropiles. Such piles are designed to act individually, although, they may be installed in groups.

The remaining applications involve networks of reticulated micropiles as components of a reinforced soil mass, which is used for stabilization and support. These

micropiles are referred to as CASE 2 elements. The structural loads are applied to the entire reinforced soil mass, as opposed to individual piles. CASE 2 micropiles are lightly reinforced because they are not individually loaded as CASE 1 elements. They serve to circumscribe and then to internally strengthen the reinforced soil composite. Note that the description of CASE 1 and 2 is not complete. There are a number of cases where a combination of the two cases will be necessary to describe a micropile group (Pearlman, et al, 1992).

Method of Grouting

The micropile classification based on the method of grouting consists of a letter designation (A through D) based primarily on the method of placement and pressure under which grouting is used during construction (Juran et. al, 1999). The classification is shown schematically in Figure2-3.

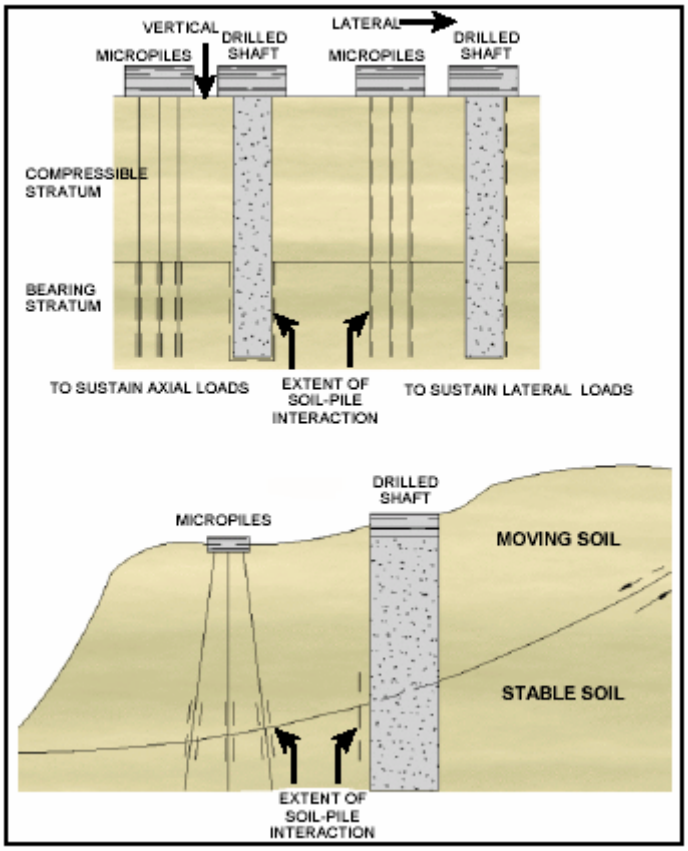

Figure 2-1. CASE 1 Micropiles (directly loaded) (Sharma, 2001)

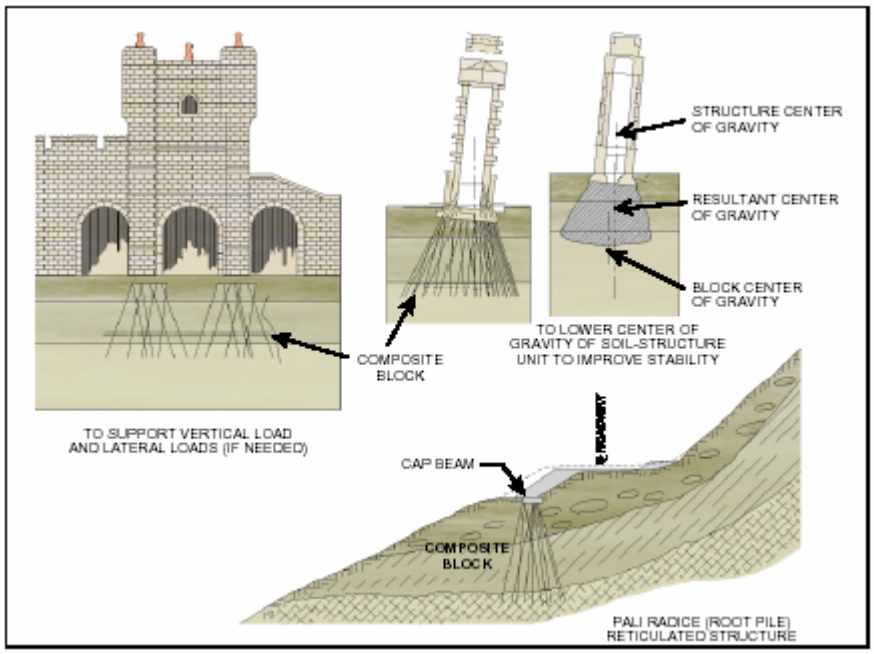

Figure 2-2. CASE 2 Micropiles % Reticulated Pile Network with Reinforced Soil Mass Loaded or Engaged (Sharma, 2001)

Type A: The type A classification indicates that grout is placed under gravity head only. Sand-cement mortars, as well as neat cement grouts, can be used because the grout column is not pressurized. The pile hole may be underreamed to increase tensile capacity, although this technique is not common or used with any other pile type.

Type B: Type B indicates that neat cement grout is placed into the hole under pressure as the temporary steel drill casing is withdrawn. Injection pressures typically range from 0.5 to 1 MPa, and are limited to avoid hydro fracturing the surrounding ground or causing excessive grout takes, and to maintain a seal around the casing during its withdrawal, where possible.

Type C: Type C indicates a two-step process of grouting: 1) neat cement grout is placed under gravity head as with Type A, and 2) prior to hardening of the primary grout (after approximately 15 to 25 minutes), similar grout is injected one time via a sleeved grout pipe without the use of a packer (at the bond zone interface) at a pressure of at least 1 MPa. This pile type appears to be used only in France, and is referred to as IGU (Injection Globale et Unitaire).

Type D: Type D indicates a two-step process of grouting similar to Type C with modifications to Step 2. Neat cement grout is placed under gravity head as with Types A and C and may be pressurized as in Type B. After hardening of the initially placed grout, additional grout is injected via a sleeved grout pipe at a pressure of 2 to 8 MPa. A packer may be used inside the sleeved pipe so that specific horizons can be treated several times, if required. This pile type is used commonly worldwide, and is referred to in France as the IRS (Injection Répétitive et Sélective).

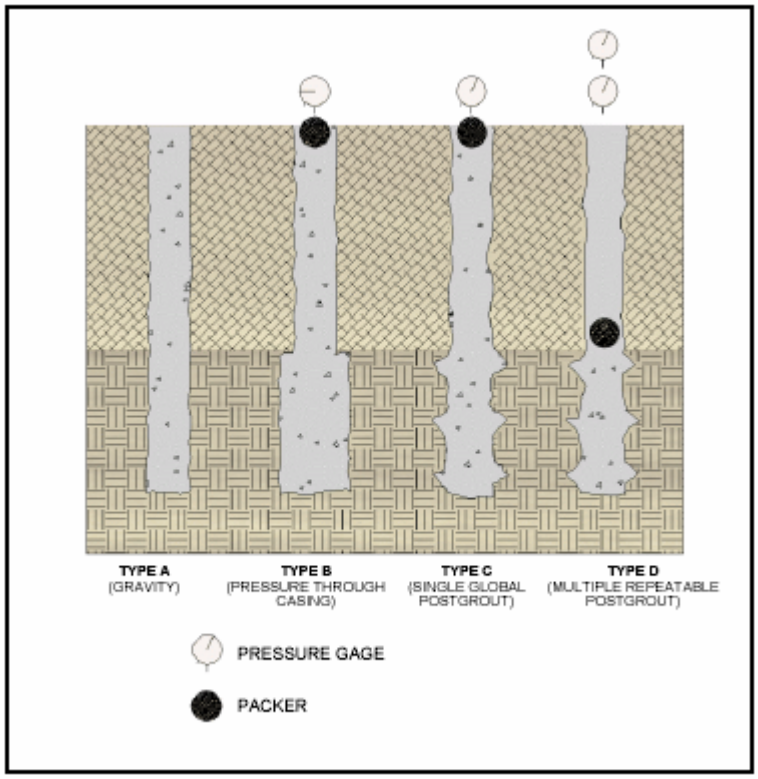

Figure 2-3. Micropile Classification Based on Type of Grouting (Sharma, 2001)

2.2 Performances of Micropiles

2.2.1 Group and Network Effects

Micropiles support loads individually, as a group, or as a network. In cases of groups and networks, the micropiles and the surrounding soil will form a composite block to resist the applied loads. This may lead to a group capacity or network capacity that is different from the total capacity of individual piles consisting of the group or network. As structural elements, micropiles are considered as equivalent to conventional piles. Thus, the group effect on micropile performance can be examined by observing conventional piles.

The group effect of piles in granular soil has been studied by many researchers. The results have been inconsistent and a plausible explanation has not been made up to now.

In the study piles under vertical loading, a parameter termed as efficiency is often used to evaluate the group effect:

$$\eta = \frac{Q_g}{nQ_s} \tag{1-1}$$

where η is the number of group piles, Q_g is the capacity of the group piles, and Q_s is the capacity of a reference pile that is identical to a group pile but is isolated from the group. The group effect is called positive if $\eta > 1$ and negative if $\eta < 1$.

Lo (1967) presented group efficiencies of piles versus spacing under different numbers of micropiles in the group, sand density, and micropile roughness, which were measured by different researchers. The results are shown in Figure 2-4, where it can be found that the group effect is not consistent, but most of piles present positive group effect.

Vesic (1969) presented group efficiencies against pile spacing for different pile numbers in the group (Figure 2-5). All tested piles presented positive group effects, however, unfortunately density states of the sand are unknown for the tests.

O'Neil (1983) made a comprehensive study of the behavior of pile groups under axial loading. Figure 2-6 shows a compilation of results of reduced scale model tests where piles were driven into friction soils. It was concluded that, for loose soils, the efficiency coefficient of the group is always higher than 1 and reaches a maximum for spacing of S/B=2. The coefficient also increases with the number of piles. On the other hand, for dense soils, with a spacing 2<S/B<4 (typical case) the efficiency coefficient is slightly greater than unity, as long as the piles are installed without boring or injection.

Lizzi & Carnevale (1979) and Lizzi (1985) reported some model test results of group effect on micropiles on coarse sand. The layout of the test is indicated in Figure 2-7. The experimental program consisted of four series of tests, with piles length of 50,100,150, and 200 pile diameter, respectively. Each series consisted of 6 groups of 3 piles each, spaced at 2 to 7 diameters, plus additional single piles. The results of the tests are as summarized in the Figure 2-7. It can be seen that for spacing between 2 and 7 diameters, the load bearing capacity of the piles in groups is higher than the load bearing capacity of a single pile.

Another result of model tests reported by Lizzi is on the added beneficial 'network effect' for a reticulated *pali radice* micropiles. Tests were carried out on three groups of piles: one formed by three vertical piles, spaced at 17.5 diameters; the second formed by 18 vertical piles, spaced at 7 diameters; and the third formed by 18 piles again spaced 7 diameters, but arranged in a basket like network (Figure 2-8). Assuming the value of load bearing capacity for a pile belonging to group No. 1 as 100% (widely spaced piles), the efficiency of group of 18 vertical piles was 68%. The corresponding efficiency for an 18-pile network was122%.

The FOREVER (2002) National Project conducted in France through 1993 to 2001 presented several experimental studies in full-scale conditions and on reduced scale models (Table 2-1). These tests were aimed to investigate the influence of pile spacing on the group effect. In all 54 vertical loading tests performed on groups of vertical micropiles. The majority had an efficient less than or close to 1, but only the groups with a large number of micropiles had efficiency greater than unity.

Ismael (2003) reported some axial load tests on bored piles and pile groups in medium dense to very dense cemented sands. It was found that the group efficiency was equal to 1.22 when the pile spacing was two-pile diameter increasing to 1.93 for a spacing of three-pile diameters.

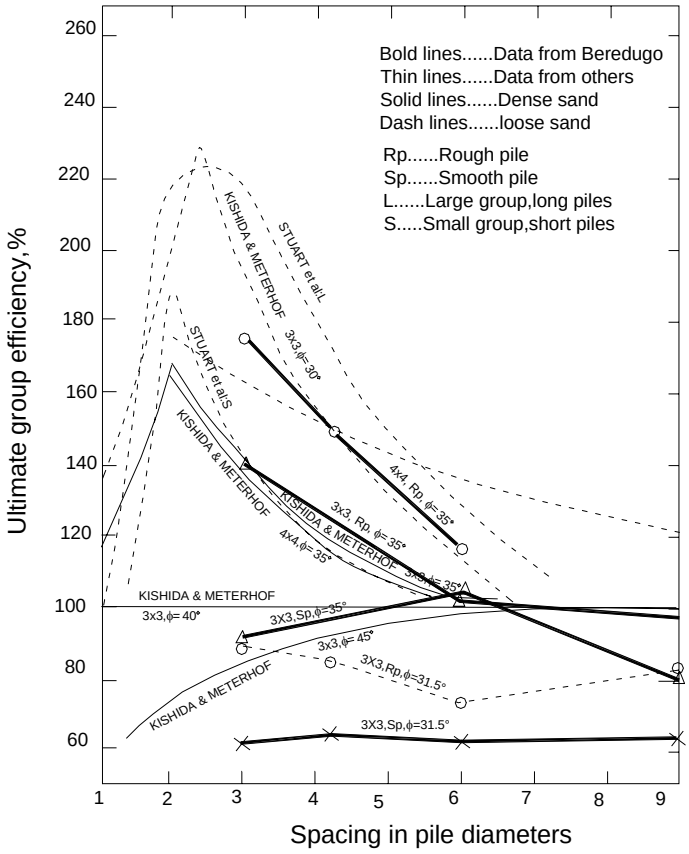

Figure 2-4. Measured values of efficiency coefficients for groups of piles in sand (Lo, 1967)

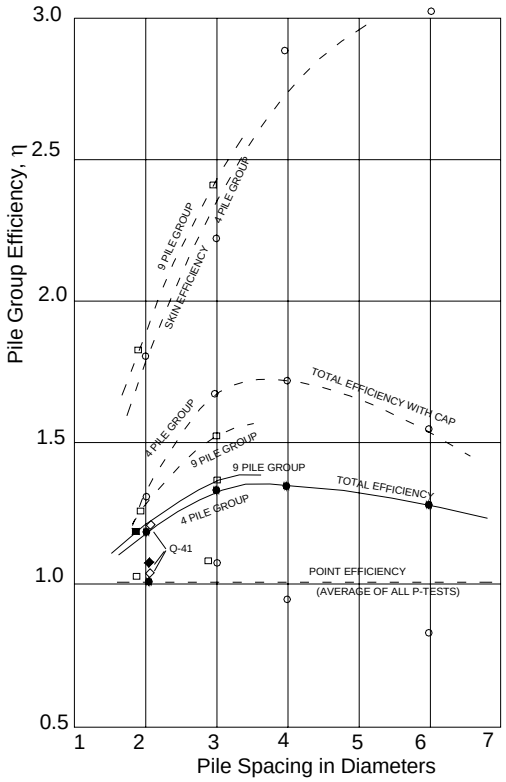

Figure 2-5. Measured values of efficiency coefficients for groups of piles (Vesic, 1969)

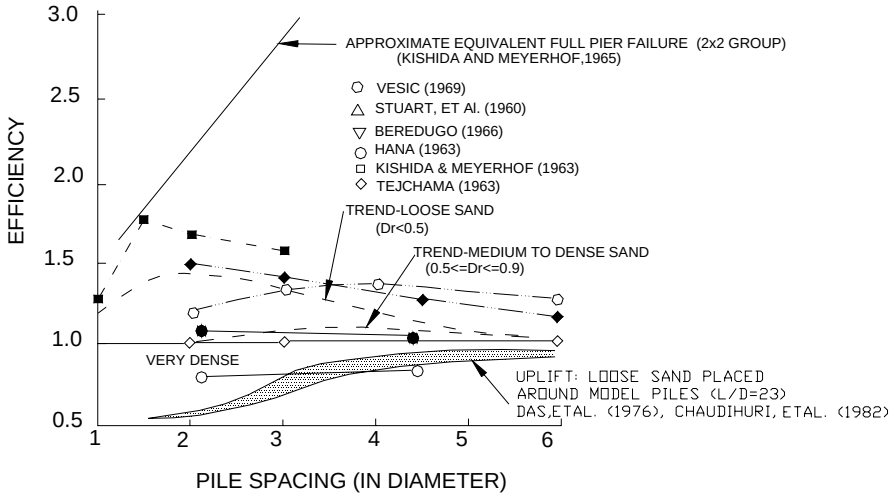

A. 4-PILE GROUPS

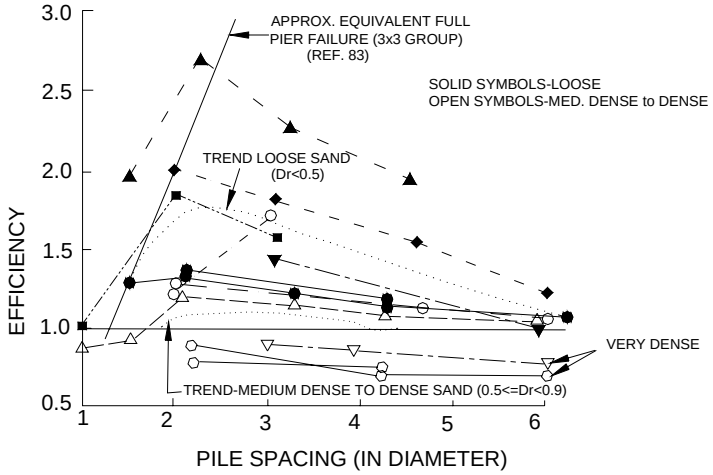

Figure 2-6. Measured values of efficiency coefficients for pile groups in sand (O'Neill, 1983)

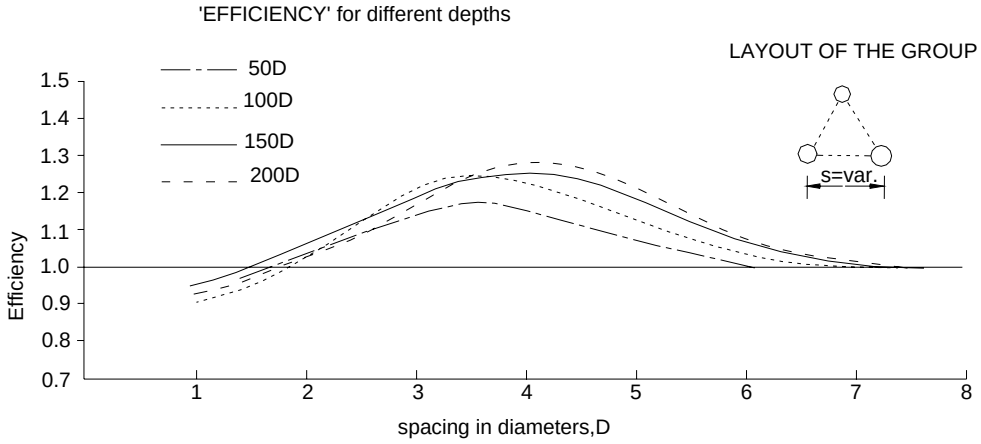

Figure 2-7. Efficiency of piles in groups (after Lizzi, 1985)

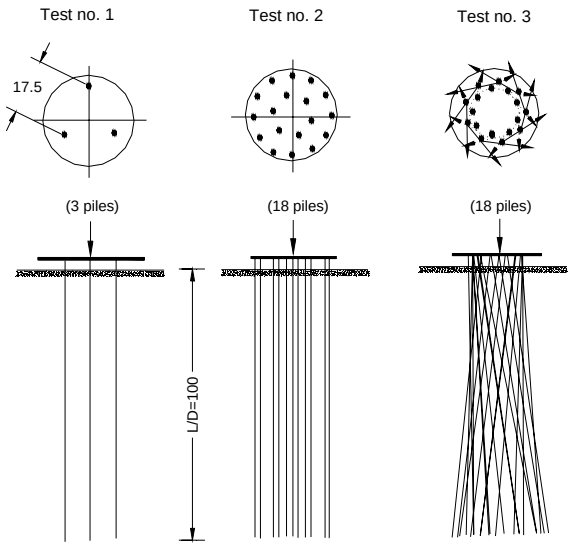

Figure 2-8. Group effect and network effect: Layout of the tests (after Lizzi, 1985)

Table 2-1. Values of the efficiency coefficient for different micropiles groups tested in the FOREVER National Project (Fontainebleau sand)

Organization	Type of test	N	Installation method	Spacing S/B	D m	B cm	I_D	Efficiency η
CEBTP	Full-scale site	4	Boring	2	5	10	0.57	0.8-1.1
LCPC	Centrifuge 10g	3	Jacking	1.5-3	0.5	1.2	0.65	0.76-1.05
LCPC	Centrifuge 20g	9-36	Jacking	4-10	0.25	6	0.57	1.18-1.53
LCPC	Centrifuge 10g	18	Cast-in-place	7	0.2	0.2	0.8	1.56-1.61
L3S	Experimental tank	4	Jacking	2, 3	1.5	2.5	0.5	0.8-1.1
L3S	Experimental Tank	18	Jacking	3.5, 7	1	2	0.45/0.5	1.6-2.2
CERMS	Mini-calibration chamber	5	Jacking	2.1	0.2	1.12	0.36/0.5/0.76	0.59-0.95
CERMS	Mini-calibration chamber	5	Jacking	2.8	0.5	2	0.45/ 0.55/0.8	0.75-0.87
CERMS (2001)	Mini-calibration chamber	5	Cast-in-place	4	0.5	1	0.55	0.63-0.74

2.2.2 Displacement Effect

The effects of displacement on driven piles have been widely investigated. It is agreed that the displacement effect caused by driven pile or displacement pile leads to increase of bearing capacity of pile in loose sand but a decrease in dense sand. The displacement effect is essentially reflected in the group effect of driven or displaced pile as well, where group effect of piles in loose sand is positive, but might be negative in dense sand. Micropiles are often considered as a kind of drilled, cast-in-place, small diameter grouted piles. When micropiles are installed in network due to their inclination it is still possible to develop a displacement effect. In practice, Auger displacement piles (the displacement drill tool as shown in Figure 1-19) are often used in loose sand to increase bearing capacity of piles (Bustamante & Gianeselli, 1993; Brown & Drew, 2000; NeSmith, 2002). It has been hypothesized that the installation results in densification and a change in the coefficient of earth pressure from its rest value K_0 to its passive value K_p. This condition would result in increased shaft resistance in soils.

The effect of displacement on pile performances in sand is determined by sand state. Therefore, the displacement effect, group effect and network effect of micropiles in sand soil cannot be explained by traditional theory of pile-soil interaction neglecting state-dependence strength of sand. It is essential that a "state parameter" should be considered in the evaluation of performances of micropiles in sand.

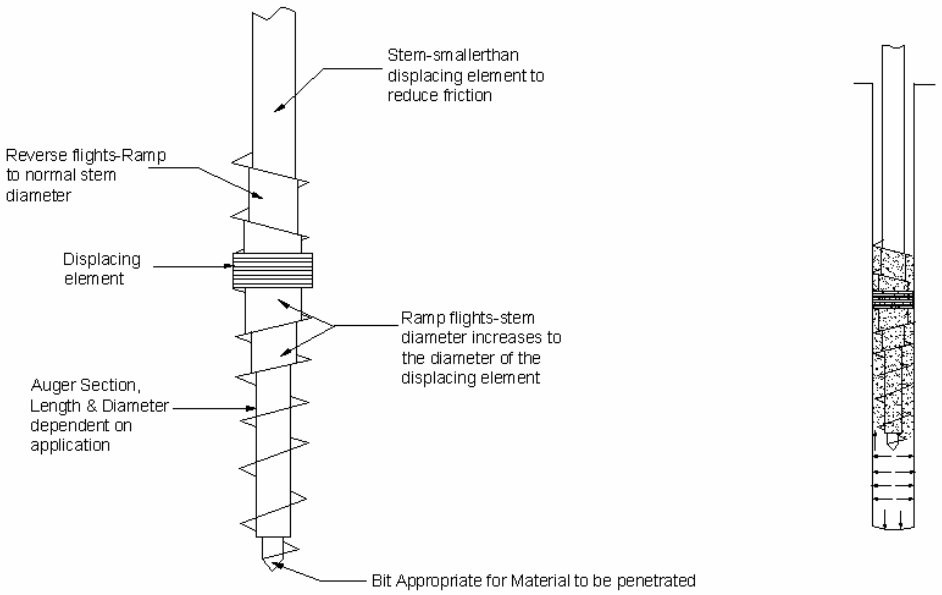

Figure 2-9. Displacement Drill Tool

CHAPTER 3

MODELING THE STATE OF SOIL AND ITS RESPONSE

3.1 General

The comprehensive description of the state of a granular soil must take into account its void ratio (or the relative density), confining stress, and its fabric. Critical state soil mechanics (Schofield and Wroth, 1968) has made a significant contribution to the description of a state of soil in this regard. It considers the state of soil to be determined by the combination of both void ratio *e* and effective confining pressure *p*. It neglects the consideration of fabric, which has been shown recently to affect the behavior of sand significantly (Masad and Muhunthan, 2000; Dafalias et al. 2004). Following the critical state framework, this study first considers the state description in terms of void ratio and mean stress. This will be extended to consider the effect of fabric as necessary.

3.2 Critical State and State Parameters

The critical state is generally defined in a three dimensional mean effective stress, deviator stress and specific volume (p′, q, v) space, where:

the mean normal effective stress, p′, is defined in principal stress space by:

$$p' = \frac{1}{3}\left(\sigma'_1 + \sigma'_2 + \sigma'_3\right) \tag{3-1}$$

and the deviator stress, q, by:

$$q = \frac{1}{\sqrt{2}}\left(\left(\sigma'_2 - \sigma'_3\right)^2 + \left(\sigma'_3 - \sigma'_1\right)^2 + \left(\sigma'_1 - \sigma'_2\right)^2\right)^{\frac{1}{2}} \tag{3-2}$$

σ_1', σ_2', σ_3' are the principal effective stresses. For a triaxial compression test conditions, $\sigma_2' = \sigma_3'$, and Eqs. (3-1) and (3-2) reduce to:

$$p' = \frac{1}{3}\left(\sigma_1' + 2\sigma_3'\right) \tag{3-3}$$

$$q = \sigma_1' - \sigma_3' \tag{3-4}$$

The specific volume v is defined by:

$$v = 1 + e \tag{3-5}$$

Roscoe, Schofield and Wroth (1958) quoted experimental evidence that the ultimate state of any soil specimen during a continuous remolding and shear flow will lie on a critical state line with equation:

$$\Gamma = v + \lambda \ln p' = v_\kappa + (\lambda - \kappa) \ln p' \tag{3-6}$$

shown in Figure 3-1. The critical state line with equation $(v + \lambda \ln p') = \Gamma$ can be seen as one of a family of parallel lines with equation $(v + \lambda \ln p') = v_\lambda$.

The critical state line can be used to distinguish the two different types of behavior of soils. There are states for which the combinations of specific volume v and mean normal effective stress p′ lie further away from the origin than the line of critical states, so that,

$$v + \lambda \ln p' > \Gamma \text{ , or } v_k + (\lambda - \kappa) \ln p' > \Gamma \text{ , or } v_\lambda > \Gamma \tag{3.7}$$

and these states have been called “wetter than critical”; shearing there causes aggregates to compress to more dense packing and emit water with ductile stable yielding of a test specimen and this type of soil may be called contractive soil. There are also states of specific volume v and mean normal effective stress p′ such that

$$v + \lambda \ln p' < \Gamma \text{ , or } v_k + (\lambda - \kappa) \ln p' < \Gamma \text{ , or } v_\lambda < \Gamma \tag{3-8}$$

and these states have been called “drier than critical”; where shearing causes aggregates to dilate and suck in water and ground slips at peak strength with unstable failures and this type of soil may be called dilative soil.

Therefore, the critical state line can be used to develop a state parameter that combines the effect of void ratio and effective confining pressure. This idea was proposed by Wroth and Basset (1965) but the proposal to use a state parameter became widely accepted after the publication of Been and Jefferies (1985). Since then many variations of the parameter have been adopted in practice (Atkinson 1993).

A state parameter ψ (Wroth and Basset, 1965; Been and Jefferies, 1985) is defined by the difference of the void ratio and the critical state void ratio corresponding to an effective confining pressure (Figure 3-2). It was demonstrated that sand characteristics are dependent on the state parameter and its use provided a powerful means to describe its features.

The ratio of current mean effective stress to mean effective stress at critical state for current void ratio ($R_s = \frac{p'_0}{p'_{cs}}$), has also been used as a state parameter (Klotz & Coop, 2001; Jovicic & Coop, 1997, Wang, 2002). If the slope of the critical state line and the series of consolidation lines are assumed parallel, then R_s and ψ are related by:

$$R_s = e^{\frac{\psi}{\lambda}} \tag{3-9}$$

Where λ is the slope of the critical state line.

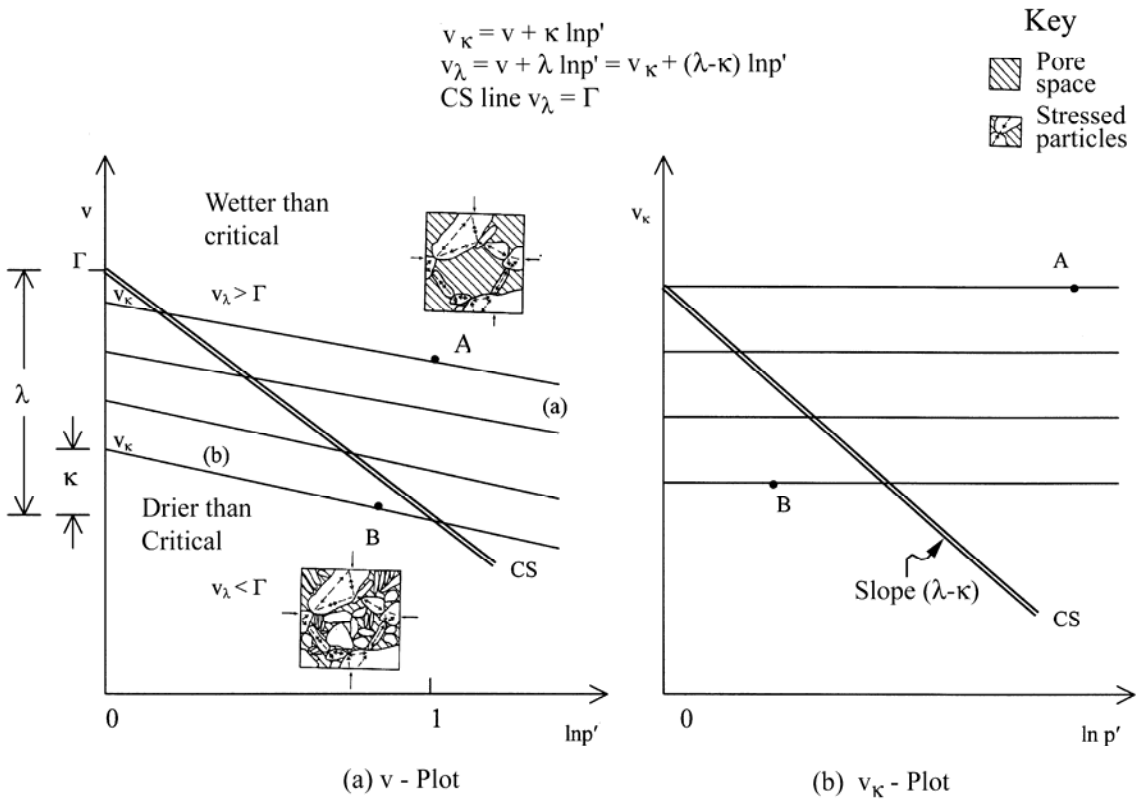

Figure 3-1 The Critical State line in v-lnp ′and v_k-lnp′ space.

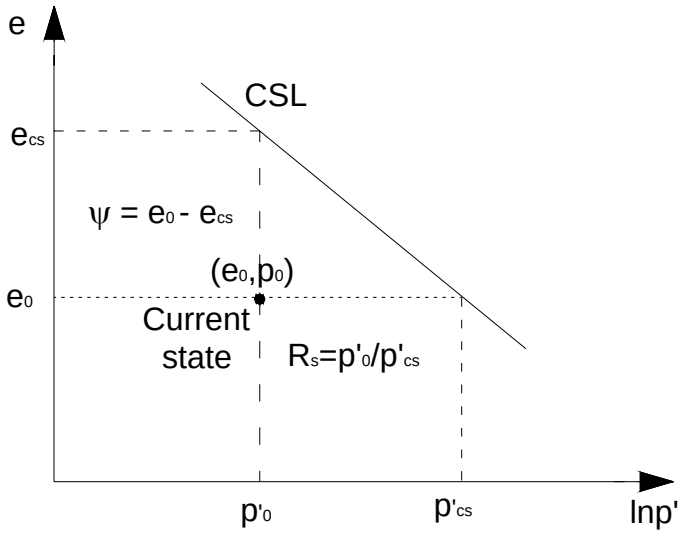

Figure 3-2 Definition of state parameters

3.3 Soil Resistance to State Parameter

Been et. al. (1986) examined the interpretation of the cone penetration test in sand in terms of the state parameter ψ. Existing data obtained from calibration chamber tests were reinterpreted to provide the relationship of cone tip resistance with the state parameter. It was found that the normalized cone tip resistance correlated well with the state parameter. Been et. al. (1987) expanded the range of application for several types of sand, and proposed a normalized cone resistance- ψ relationships for normally consolidated sands as

$$\frac{q_c - p}{p'} = k \exp(-m\psi) \tag{3-10}$$

where p is mean normal total stress, p' is mean normal effective stress, m is the slope of the normalized $q_c - \psi$ relationship and k is the normalized q_c value at $\psi = 0$. Since λ is a significant variable in controlling the resistance of sand to cone penetration, relationships between λ and m, k were obtained by plotting the m and k against λ for different sands as:

$$m = 8.1 - \ln \lambda \tag{3-11}$$

$$k = 8 + \frac{0.55}{\lambda - 0.01} \tag{3-12}$$

Equations (3-10)-(3-12) may be combined to provide a complete relationship for cone resistance in terms of the key factors controlling sand behavior during shear (ψ and λ) as follows

$$\frac{q_c - p}{p'} = \left(8 + \frac{0.55}{\lambda - 0.01}\right) \exp\left[-(8.1 - \ln \lambda)\psi\right] \tag{3-13}$$

Equation (3-13) correlates cone penetration resistance q_c to state parameter through λ and p.

Since the study by Been et al (1986) several researchers have correlated the resistance of granular soils to pile and penetrometers in terms of the soil state parameter ψ (Carriglio et. al., 1990; Konrad, 1998; Klotz & Coop, 2000). Carriglio, et. al. (1989) also showed a relationship between normalized cone resistance and ψ obtained from calibration chamber in situ tests performed on pluvially deposited, predominantly silica Ticino as:

$$\frac{q_c - p}{p'} = 33.9 \exp(-3.06\overline{\psi}) \tag{3-14}$$

Note that $\overline{\psi} = \dfrac{\psi}{e_{\max} - e_{\min}}$.

Klotz & Coop (2001) investigated the behavior of driven piles in sand by means of physical model testing. An instrumented model pile was developed, which was tested in two sands: a typical quartzitic sand (Leighton Buzzard sand) and a carbonate sand (Dog's Bay sand). It was found that both normalized base resistance and normalized shaft friction of the two sands correlated well to the state parameter $R_s = \dfrac{p'_0}{p'_{cs}}$. However, the results obtained from the study indicated that there are no correlations existing between either normalized base resistance or normalized shaft friction of the two sand and the state parameter ψ. The sand state in the study was limited in the zone denser than critical state discussed by Pillai & Muhunthan (2002). Therefore, further studies are needed to investigate the correlation between bearing capacity of pile and sand state.

CHAPTER 4

STATE-DEPENDENT BOUNDING SURFACE MODEL

4.1 General

It is well appreciated that, whilst the original Cambridge, critical state models work well for normally consolidated clays, significantly more complex models are required to capture the essential properties of the mechanics of sands. There is now a vast literature both on the experimentally determined behavior of sands and the construction of mathematical models, which attempt to predict this behavior. It is generally agreed that non-associated flow rules, some form of shear hardening, induced anisotropy, and the improved modeling of dilatancy, must be added to the basic structure of critical state soil mechanics in order to obtain an acceptable degree of realism in these models. Many of these models make use of the "state parameter" concept proposed by Been and Jefferies (1985). In these models the void ratio e is replaced by a "state parameter" as the fundamental variable, which determines the size of the yield surface and the flow rule.

Li & Dafalias (2000) and Li (2002) developed a comprehensive bounding surface sand model that is formulated within a critical-state framework. The basic formulations of bounding surface plasticity theory are presented in Appendix A. The dilatancy of granular soils is assumed to depend not only on the stress ratio $\eta = \frac{q}{p}$, where q and p are the deviatoric and mean effective normal stresses respectively, but also on the current material internal state in reference to the critical state in $e - p - \eta$ space. The material internal state is defined in the model by state parameter ψ (Been & Jefferies, 1985). The model was shown to simulate well both contractive and dilative responses of granular

soils over a wide range of variations in stress and material internal states in general multi-dimension space under different loading and drained conditions. It is used here to investigate the effects of material internal states on the performance of micropiles.

4.2 Dilatancy

It has been well observed in triaxial tests that, subjected to a shear under drained conditions, dense sand dilates accompanied by strain softening and loose sand contracts accompanied by straining hardening, as shown in Figure 4-1. The dilation or contraction of sand under different states is in essence the coupling between shear and volumetric strains, or, more appropriately, defined by the dilatancy, *D*, the ratio of plastic volumetric strain increment to plastic deviatoric strain increment. In triaxial space and multi-dimensional space, the dilatancy is defined, respectively, as:

$$D = \frac{d\varepsilon_v^p}{d\varepsilon_q^p} \tag{4-1a}$$

$$D = \frac{d\varepsilon_{kk}^p}{\sqrt{\frac{2}{3} de_{ij}^p de_{ij}^p}} \tag{4-1b}$$

where $\varepsilon_{kk}^p = \varepsilon_v^p$ is the plastic volumetric strain which is defined as compression positive, and $e_{ij}^p = \varepsilon_{ij}^p - \varepsilon_{kk}^p \delta_{ij} / 3$ are the components of the plastic deviatoric strain tensor.

Rowe (1962) suggested an expression for dilatancy *D* based on the theory of least rate of internal work as:

$$D = \frac{9(M - \eta)}{9 + 3M - 2M\eta} \tag{4-2}$$

Eq. (4-2) is similar to the original and modified Cam-clay flow rules:

$$D = M - \eta \tag{4-3a}$$

$$D = \frac{M^2 - \eta^2}{2\eta} \tag{4-3b}$$

The similarity is the result of assuming a unique relationship between the stress ratio η and the dilatancy $D = \frac{d\varepsilon_v^p}{d\varepsilon_q^p}$. Mathematically, this relationship can be written in a general form as:

$$D = f(\eta, C) \tag{4-4}$$

where C is a set of intrinsic material constants. The function expressed by Equation (4-4) implies that a soil yielding at $\eta = M$ is coincident with $D = 0$; i.e., whenever a plastic deformation takes place at $\eta = M$ the material reaches its ultimate failure. This, however, is not always in agreement with experimental observations. Especially in dense sands D may become zero well before the sand reaches its critical state. On the other hand, in Equations (4-2) and (4-3), C only refers to the stress ratio M of soil in critical state that is determined by friction between the mineral surfaces of the particles. Thus, Equations (4-2) and (4-3) do not reflect the important dependence of dilatancy on density and pressure because they ignore material internal state. In fact, ignorance of the dependence of dilatancy on the internal state of the material in the classical stress-dilatancy relations is the major obstacle to unified modeling of sand behavior.

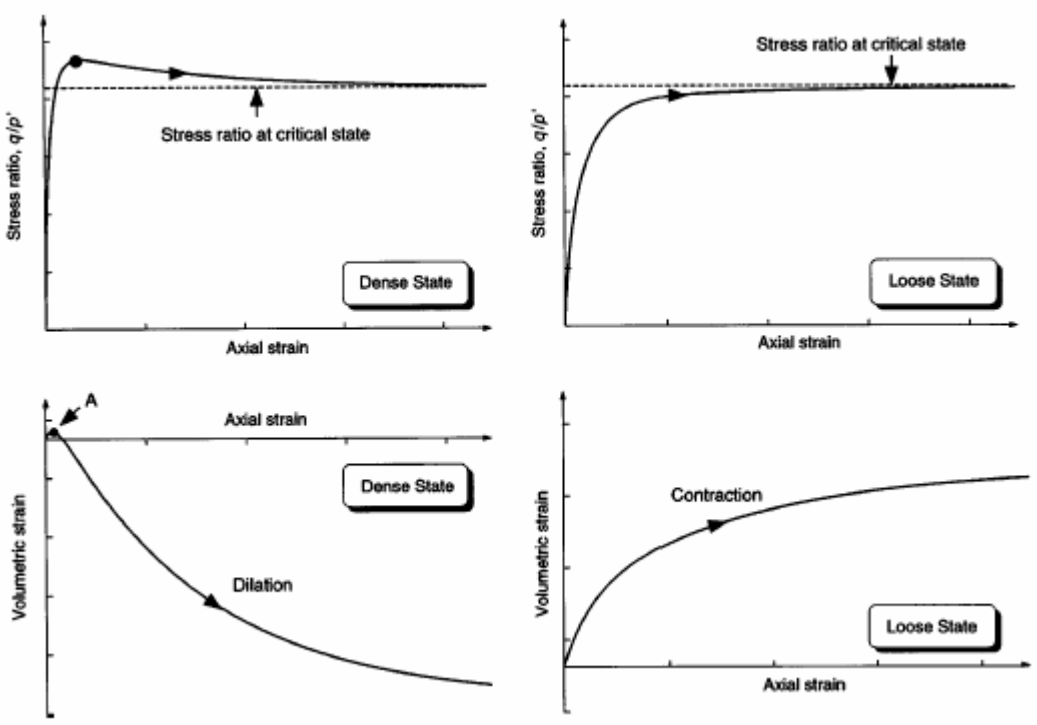

Figure 4-1 Typical response of sand in loose and dense states in triaxial compression

Li & Dafalias (2000) proposed a general form of the state-dependent dilatancy in triaxial compression space, which can be generalized to multi-axial space as follows:

$$D = D(R, \theta, e, Q, C) \tag{4-5}$$

where θ is the Lode angle, varying from -30^0 for triaxial compression to $+30^0$ for triaxial extension; and R is a stress ratio invariant defined as:

$$R = \sqrt{\frac{3}{2} r_{ij} r_{ij}} = \frac{\sqrt{3J_{2D}}}{p} \tag{4-6}$$

$J_{2D} = {s_{ij}s_{ij}}/{2}$. Note that R here is a slightly different from that defined by Wang, et. al (1990) as described in Appendix A. e is void ratio; Q and C, as collective terms, denote internal state variables other than the void ratio e and intrinsic material constants,

respectively. At the critical state, $e = e_c$ and the stress ratio $R = M(\theta)$, where M is the critical stress ratio for the shear mode characterized by θ. Therefore, at the critical state:

$$D[R = M(\theta), e = e_c, Q, C] = 0 \tag{4-7}$$

4.3 General Framework

There are two bounding surfaces in the model defined in $\sqrt{J_{2D}} - \theta - p$ space: a cone with straight meridians and a flat cap, as shown in Figure 4-2(a). The cone-shaped surface is associated with plastic loading induced by a change in stress ratio, r_{ij}, and the cap is associated with the plastic loading due to a change in p under a constant r_{ij}. Because the surface meridians are straight, the cone can be fully described by a cross-section in the $R - \theta$ plane, as shown in Figure 4-2(b).

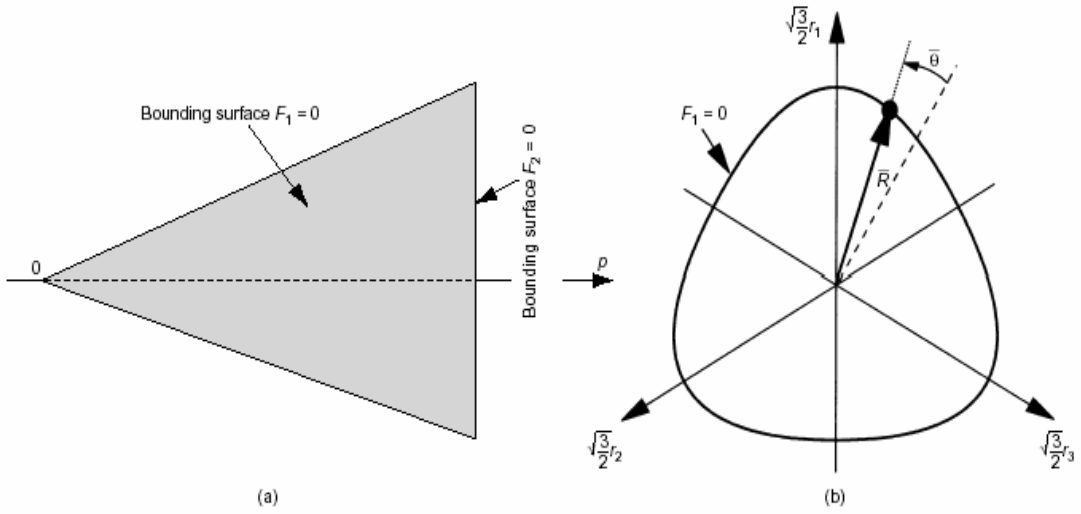

Figure 4-2 Shear bounding surfaces F_1 and bounding cap surface F_2

The cone-shaped bounding surface is analytically expressed by:

$$F_1 = \frac{\bar{R}}{g(\bar{\theta})} - H_1 = 0 \tag{4-8}$$

where the superposed bar indicates that the quantity is evaluated on the bounding surfaces. $\bar{R} = \bar{R}(\bar{r}_{ij})$, $\bar{\theta} = \bar{\theta}(\bar{r}_{ij})$ are two non-trivial invariants of the image stress ratio tensor $\bar{r}_{ij}$ on F_1, and H_1 defines the size of the cone and is a function of the internal state variables that are associated with the evolution of F_1. $g(\bar{\theta})$ represents the variation of $\bar{R}$ on the bounding surface with $\bar{\theta}$ and it is defined as:

$$g(\bar{\theta}) = \frac{2c}{(1+c)-(1-c)\cos 3\bar{\theta}} \tag{4-9}$$

where *c* is a material constant. $g(\bar{\theta})$ varies smoothly from unity for triaxial compression ($\bar{\theta} = -30^0$) to *c* for triaxial extension ($\bar{\theta} = 30^0$) for all evolving bounding surfaces including the ones at the critical state. Thus, *c* in effect defines the ratio of $\bar{R}$ at triaxial extension over that at triaxial compression for all evolving bounding surfaces and can simply be expressed as $c = \frac{M_e}{M_c}$. Note that F_2 (Fig. 4-2) is a straight line form with F_2= p-H_2=0.

The consistency condition of Equation (4-8) requires $dF_1 = 0$ leading to:

$$p\bar{n}_{ij} d\bar{r}_{ij} - \bar{K}_{p1} dL_1 = 0 \tag{4-10}$$

or, in terms of the actual stress ratio increment,

$$p\bar{n}_{ij} dr_{ij} - K_{p1} dL_1 = 0 \tag{4-11}$$

where $\bar{n}_{ij}$ is a zero-trace unit tensor normal to F_1 at the image stress ratio $\bar{r}_{ij}$, K_{p1} (as well as $\bar{K}_{p1}$) is the plastic modulus controlling the evolution of F_1, and dL_1 is a scalar loading index. Note that K_{p1} is related to $\bar{K}_{p1}$ in such a way that when the stress ratio is on F_1 (i.e. $r_{ij} = \bar{r}_{ij}$), $K_{p1} = \bar{K}_{p1}$.

The consistency condition for the cap, $dF_2 = 0$, results in:

$$d\bar{p} - \bar{K}_{p2} dL_2 = 0 \tag{4-12}$$

or, in terms of the actual mean normal stress increment as:

$$dp - K_{p2} dL_2 = 0 \tag{4-13}$$

where K_{p2} (as well as $\bar{K}_{p2}$) is a plastic hardening modulus that controls the evolution of the cap, and dL_2 is a scalar loading index associated with it. K_{p2} is related to $\bar{K}_{p2}$ in such a way that when the mean normal stress, p, is on the cap F_2 (i.e. $p = \bar{p}$), $K_{p2} = \bar{K}_{p2}$.

Assuming that the associative flow rule applies to a constant p subspace (Baker & Desai, 1982):

$$de_{ij}^{p} = de_{ij}^{p1} + de_{ij}^{p2} = \bar{n}_{ij} dL_1 + \bar{m}_{ij} dL_2 \tag{4-14}$$

where de_{ij}^{p1} and de_{ij}^{p2} are the plastic deviatoric strain increments associated with the loading indices dL_1 and dL_2, respectively. $\bar{m}_{ij}$ is a unit tensor that defines the direction of plastic deviatoric strain increment due to a change in p under a constant stress ratio r_{ij}. Wang, et. al. (1990) proposed that $\bar{m}_{ij} = r_{ij} \Big/ |r_{ij}|$ (See Appendix A).

Assuming that a plastic volumetric strain increment can be decomposed into two parts, $d\varepsilon_v^{p1}$ and $d\varepsilon_v^{p2}$, they are paired with de_{ij}^{p1} and de_{ij}^{p2} respectively, as:

$$d\varepsilon_v^{p} = d\varepsilon_v^{p1} + d\varepsilon_v^{p2} = \sqrt{\frac{2}{3}}\left(D_1 \sqrt{de_{ij}^{p1} de_{ij}^{p1}} + D_2 \sqrt{de_{ij}^{p2} de_{ij}^{p2}}\right) = \sqrt{\frac{2}{3}}\left(D_1 dL_1 + D_2 dL_2\right) \tag{4-15}$$

where D_1 and D_2 are the two dilatancy functions associated with $d\varepsilon_v^{p1}$ and $d\varepsilon_v^{p2}$ respectively.

Assuming that the elastic responses are based on Hooke's law, the elastic incremental strains can be expressed as:

$$d\varepsilon_{ij}^{e} = \frac{p dr_{ij}}{2G} + \frac{r_{ij} dp}{2G} \tag{4-16a}$$

$$d\varepsilon_{v}^{e} = \frac{dp}{K} \tag{4-16b}$$

Using Equations (4-13) (4-15) and (4-16b), dL_2 can be determined:

$$dL_2 = \frac{K d\varepsilon_v - \sqrt{\frac{2}{3}} K D_1 dL_1}{\sqrt{\frac{2}{3}} K D_2 + K_{p2}} \tag{4-17}$$

Combining Equations (4-11), (4-14), (4-15), (4-16) results in:

$$\left(2G\bar{n}_{ij} de_{ij} - K d\varepsilon_v \bar{n}_{ij} r_{ij}\right) - \left(2G - \sqrt{2/3} K D_1 \bar{n}_{ij} r_{ij} + K_{p1}\right) dL_1 - \left(2G\bar{n}_{ij}\bar{m}_{ij} - \sqrt{2/3} K D_2 \bar{n}_{ij} r_{ij}\right) dL_2 = 0 \tag{4-18}$$

Substituting Equation (4-17) into the above equation and solving for dL_1 leads to:

$$dL_1 = \Theta_{ij} d\varepsilon_{ij} \tag{4-19}$$

where

$$\Theta_{ij} = \frac{2G\bar{n}_{ij} - K\left(\bar{n}_{rs} + B\right)\delta_{ij}}{2G - \sqrt{2/3} K D_1 \left(\bar{n}_{pq} r_{pq} + B\right) + K_{p1}} \tag{4-20}$$

in which

$$B = \frac{2G\bar{n}_{ij}\bar{m}_{ij} - \sqrt{2/3} K D_2 \bar{n}_{ij} r_{ij}}{\sqrt{2/3} K D_2 + K_{p2}} \tag{4-21}$$

and substitution of Equation (4-19) into Equation (4-17) yields

$$dL_2 = Z_{ij} d\varepsilon_{ij} \tag{4-22}$$

where

$$Z_{ij} = \frac{K\delta_{ij} - \sqrt{2/3}KD_1\Theta_{ij}}{\sqrt{2/3}KD_2 + K_{p2}} \tag{4-23}$$

The incremental stress-strain relationship can be written as

$$d\sigma_{ij} = E_{ijkl} d\varepsilon^e_{kl} = E_{ijkl}\left(d\varepsilon_{kl} - d\varepsilon^p_{kl}\right) = E_{ijkl}\left[d\varepsilon_{kl} - \left(\bar{n}_{kl} + \sqrt{2/3}D_1\delta_{kl}\right)dL_1 - \left(\bar{m}_{kl} + \sqrt{2/27}D_2\delta_{kl}\right)dL_2\right] \tag{4-24}$$

where E_{ijkl} is the elastic stiffness tensor, defined by the elastic moduli G and K. By substituting Equations (4-19) and (4-22) into Equation (4-24), one has

$$d\sigma_{ij} = \Lambda_{ijkl} d\varepsilon_{kl} \tag{4-25}$$

where the elastoplastic stiffness tensor is given by

$$\Lambda_{ijkl} = E_{ijpq}\left[\delta_{pk}\delta_{ql} - \left(\bar{n}_{pq} + \sqrt{2/27}D_1\delta_{pq}\right)\Theta_{kl} - \left(\bar{m}_{pq} + \sqrt{2/27}D_2\delta_{pq}\right)Z_{kl}\right] \tag{4-26}$$

It can be seen from Equations (4-26) (4-20) (4-21) (4-23) that the elastoplastic stiffness tensor is determined by the elastic parameters G and K, the plastic moduli K_{p1} and K_{p2}, the dilatancy function D_1 and D_2, and the zero-trace unit tensors $\bar{n}_{ij}$ and $\bar{m}_{ij}$.

4.4 Mapping Rules

Mapping rules by which the current stress state is projected to an image stress state on the bounding surface play a very important role in bounding surface plasticity. The unit tensors $\bar{n}_{ij}$ and $\bar{m}_{ij}$, the dilatancy function D_1 and D_2, and the plastic moduli K_{p1} and K_{p2} in the elastoplastic stiffness matrix are all dependent on the image stress

state. So, the mapping rules in the model determine the constitutive properties of the soil. Since the yielding is governed by two stress components, r_{ij} and p, two mapping rules are needed.

For $\bar{r}_{ij}$ mapping, a relocatable projection center, α_{ij}, is defined in the deviatoric space as the stress ratio at which the last reversal of loading direction from loading to unloading took place. The loading direction reversal is signaled by the change of the sign of dL_1 from positive to negative. The image stress ratio $\bar{r}_{ij}$ is obtained by projecting r_{ij} to the bounding surface F_1 from projection center, α_{ij} as shown in Figure 4.3. According to Equation (4-11), the negative dL_1 occurs when the tensor dr_{ij} is inward to the loading surface, which leads to projection center, α_{ij}, relocated as shown in Figure (4-4). The projection center relocation immediately brings dL_1 back to positive again. This means that plastic deformation is always produced whenever $dL_1 \neq 0$. Note that, even though there are two approaches to calculate the value of dL_1 (one is from stress increment Equation (4-10), another one is from strain increment Equation (4-19)), it is suggested that Equation (4-19) be used to avoid false unloading caused by strain softening. Additional details of the projection rule are found in Wang (1990).

According to Equation (4-10), with positive dL_1 and non-zero plastic modulus $\bar{K}_{p1}$ at the image stress state ensures a non-zero $\dot{n}_{ij} d\bar{r}_{ij}$. The sign of $\dot{n}_{ij} d\bar{r}_{ij}$ is dependent on that of $\bar{K}_{p1}$. Negative $\bar{K}_{p1}$ corresponds to soil softening and contraction of the bounding surface F_1. On the contrary, positive $\bar{K}_{p1}$ corresponds to soil hardening and expansion of the bounding surface F_1.

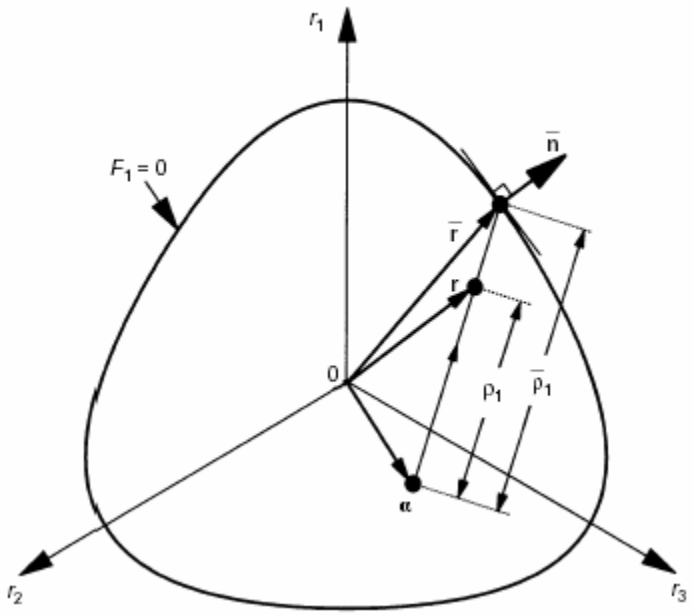

Figure 4-3 Mapping rule in deviatoric stress ratio space

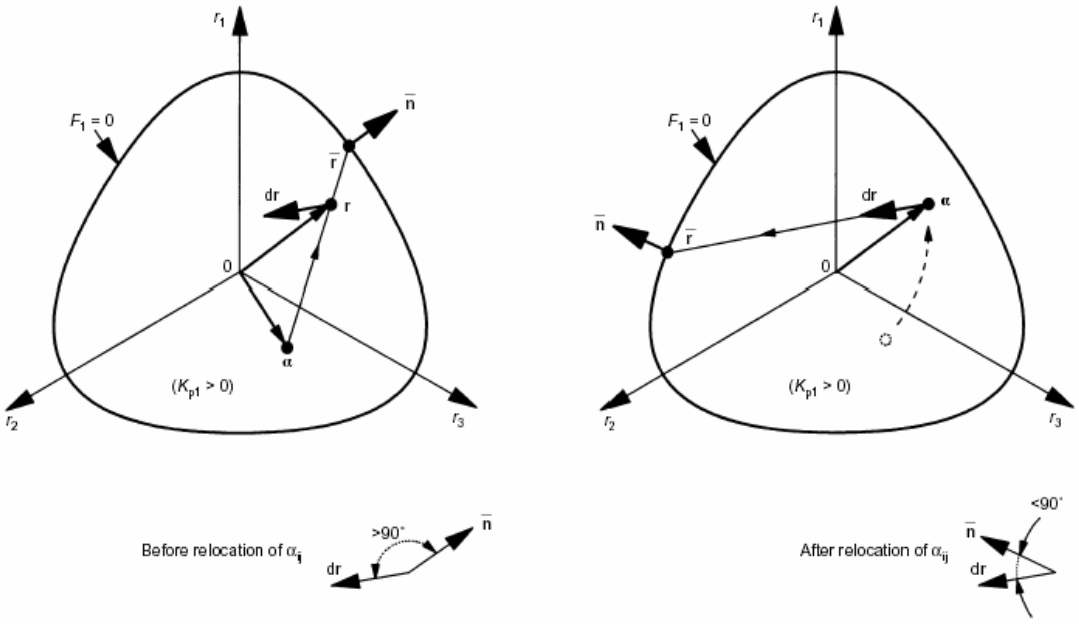

Figure 4-4 Relocation mechanism of projection center, α_{ij}

Figure 4-5 shows the mapping scheme of $\bar{p}$. As seen for $\bar{p}$ mapping, another relocatable projection center, β, is defined on the hydrostatic axis with an initial position set at zero. The projection center β will stay at the current position until the mean normal stress increment, dp, changes its sign. In this case, β jumps to the reversal point. The image mean normal stress, $\bar{p}$, is either on the cap F_2, if $dp > 0$, or at the origin, $\bar{p} = 0$ if $dp < 0$. Similar to $\bar{r}_{ij}$ mapping, $dL_2 \geq 0$ is ensured by assuming that the sign of K_{p2} is same as that of dp and the moving direction of the cap F_2 is associated with the sign of dp.

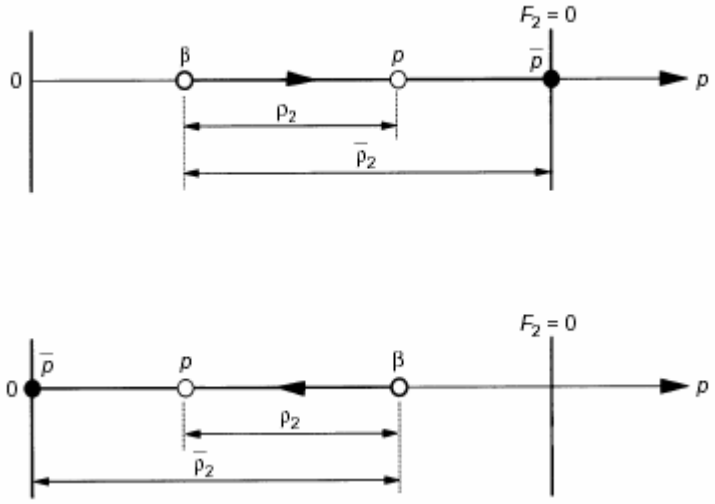

Figure 4-5 Mapping rule for p under constant r_{ij}

4.5 Model Variables and Parameters

The following gives a summary of the model parameters.

4.5.1 Elastic Moduli

The elastic shear modulus, G, is calculated using following empirical equation (Richart et al., 1970):

$$G = G_0 \frac{(2.97 - e)^2}{1 + e} \sqrt{p p_r} \tag{4-27}$$

where G_0 is a material constant, and p_r is a reference pressure, taken as $101 KP_a$ (the atmospheric pressure at sea level). In the equation, the current void ratio, e, is used instead of the initial void ratio. The elastic bulk modulus, K, is equal to:

$$K = G \frac{2(1+\nu)}{3(1-2\nu)} \tag{4-28}$$

where ν is Poisson's ratio, assumed to be a constant.

4.5.2 State Parameter ψ

The state parameter in the model is defined as follows (Li and Wang, 1998)

$$\psi = e - e_c = e - \left[e_\Gamma - \lambda_c \left(p / p_r \right)^\xi \right] \tag{4-29}$$

where e_Γ, λ_c, ξ are the material constants determining a straight critical-state line in the $e - p^\xi$ space.

4.5.3 Plastic Modulus K_{p1} *and Dilatancy* D_1

The plastic modulus associated with a stress ratio increment takes the following form:

$$K_{p1} = \frac{Gh}{\bar{R}} \left[M_c g(\bar{\theta}) \exp^{-n\psi} - \bar{R} \right] \tag{4-30}$$

where n is a model constant (a scaling factor for ψ), and Gh is a scaling factor for the modulus. The elastic shear modulus, G, serves as a reference quantity, rendering h a dimensionless parameter. It was found that a h value that varies with soil density and loading history fitted the experimental data notably better (Li 2002). Accordingly, the following empirical function was suggested:

$$h = (h_1 - h_2 e)\left\{(\rho_1/\bar{\rho}_1)^k + h_3 f(L_1)\left[1 - (\rho_1/\bar{\rho}_1)^k\right]\right\} \tag{4-31}$$

where h_1, h_2 and h_3 are material constants. The power k is an arbitrary but large number, say 10, which makes the term $(\rho_1/\bar{\rho}_1)^k \approx 0$ unless ρ_1 approaches $\bar{\rho}_1$ very closely. $f(L_1)$ is a function of the accumulated loading index, $L_1 = \int dL_1$, a measure of the magnitude of the accumulated plastic deformation due to changes in stress ratio. This function is incorporated to better reflect the influence of previous loading cycles. The following function was suggested for this purpose:

$$f(L_1) = \frac{(1 - b_3)}{\sqrt{(1 - L_1/b_1)^2 + (L_1/b_1)/b_2^2}} + b_3 \tag{4-32}$$

where b_1, b_2 and b_3 are parameters for the fine adjustment of the reverse loading responses.

The plastic modulus, $\bar{K}_{p1}$, can be obtained by letting $\rho_1 = \bar{\rho}_1$ in Equation (4-30).

The dilatancy function was suggested as follows.

$$D_1 = \frac{d_1}{M_c g(\theta)}\left[M_c g(\theta)\exp^{m\psi}\sqrt{\frac{\bar{\rho}_1}{\rho_1}} - R\right] \tag{4-33}$$

in which d_1 and m are two positive model constants.

4.5.4 Plastic Modulus K_{p2} and Dilatancy D_2

The plastic modulus under a constant stress ratio takes the following form:

$$K_{p2} = Gh_4\left[\frac{M_c g(\theta)}{R}\right]\left(\frac{\bar{\rho}_2}{\rho_2}\right)^a \frac{dp}{|dp|} \tag{4-34}$$

and

$$\bar{K}_{p2} = \begin{cases} K_{p2} & \text{if } p=\bar{p} \text{ and } dp>0 \\ 0 & \text{otherwise} \end{cases} \tag{4-35}$$

where h_4 and a are two positive models constants. The elastic shear modulus, G, serves as a reference again, rendering h_4 dimensionless.

The dilatancy associated with a dp-induced plastic deformation is as follows:

$$D_2 = d_2 \left\langle \frac{M_c g(\theta)}{R} - 1 \right\rangle \frac{dp}{|dp|} \tag{4-36}$$

where d_2 is a positive model constant. Note that D_2 is not ψ-dependent, therefore the dilatancy along a constant stress ratio $\eta = R/g(\theta)$ is uniquely related to that stress ratio.

4.5.5 Unit Tensors $\bar{n}_{ij}$ $\bar{m}_{ij}$

For each stress state r_{ij}, the corresponding image stress, $\bar{r}_{ij}$, is obtained by projecting, r_{ij}, to the bounding surface from the projection center, α_{ij}. The zero-trace unit tensor, $\bar{n}_{ij}$, is outward normal to F_1 at $\bar{r}_{ij}$.

$$\bar{n}_{ij} = \left(\frac{\partial F_1}{\partial \bar{r}_{ij}} - \frac{1}{3} \frac{\partial F_1}{\partial \bar{r}_{pq}} \delta_{pq} \delta_{ij} \right) \Bigg/ \left| \frac{\partial F_1}{\partial \bar{r}_{ij}} - \frac{1}{3} \frac{\partial F_1}{\partial \bar{r}_{pq}} \delta_{pq} \delta_{ij} \right| \tag{4-37}$$

where

$$\frac{\partial F_1}{\partial \bar{r}_{ij}} = \left[\sqrt{\frac{3}{2}} \frac{1}{\bar{R}} - \frac{27\sqrt{6}}{4} \frac{\bar{Q}}{\bar{R}^4} \frac{1}{g(\bar{\theta})} \frac{\partial g(\bar{\theta})}{\partial \sin 3\bar{\theta}} \right] \bar{r}_{ij} - \frac{9\sqrt{6}}{2} \frac{1}{\bar{R}^2 g(\bar{\theta})} \frac{\partial g(\bar{\theta})}{\partial \sin 3\bar{\theta}} r_{ik} r_{kj} \tag{4-38}$$

and $\bar{Q} = r_{ij} r_{jk} r_{ki}$

As discussed earlier, determination of $\bar{m}_{ij}$ is much easier. It is the unit tensor of $\bar{r}_{ij}$ and expressed as

$$\bar{m}_{ij} = r_{ij} \Big/ |r_{ij}| \tag{4-39}$$

4.6 Determination of Model Constants

The model parameters are summarized in Table 4-1. They constitute 2 elastic parameters, 5 critical state parameters, 6 parameters associated with plastic properties induced by increments of the stress ratio tensor, 2 parameters associated with plastic properties induced by increments of mean effective stresses, and 4 parameters which can be considered as internal parameters used to fine tune the reverse loading responses. Barring these 4 internal parameters, the 15 parameters are determined from triaxial tests as described by Li and Dafalias (2000) and Li (2002). A brief description is presented here.

Table 4-1 Summary of model parameters

Elastic parameters	Critical state parameters	Parameters associated with dr-mechanisms	Parameters associated with dp-mechanisms	Default parameters
G_0 ,ν	M, c, e_Γ , λ_c ,ξ	d_1, m, h_1, h_2 ,h_3, n	d_2 ,h_4	a=1, b_1=0.005 b_2=2,b_3=0.001

The five critical state parameters are determined by directly fitting the critical stress ratio and the critical state line in e - lnp' space.

Based on Equation (4-33):

$$m = \frac{1}{\psi^d} \ln \frac{M^d}{M} \tag{4-40}$$

where ψ^d and M^d are the values of ψ and η at the phase transform state, measured from drained or undrained test results.

Based on Equation (4-30)

$$n = \frac{1}{\psi^b} \ln \frac{M}{M^b} \tag{4-41}$$

where ψ^b and M^b are the values of ψ and η at drained peak stress state.

Ignoring the small elastic deformation in drained tests, the parameter d_0 can then be calibrated based on Equation (4-42) and the $\varepsilon_v - \varepsilon_q$ curves:

$$\frac{d\varepsilon_v}{d\varepsilon_q} \approx \frac{d\varepsilon_v^p}{d\varepsilon_q^p} = d_1\left(e^{m\psi} - \frac{\eta}{M}\right) \tag{4-42}$$

With all the material constants known inside the brackets in Equation (4-43), hG_0 can be calibrated based on the experimental $q - \varepsilon_q$ curves.

$$\frac{dq}{d\varepsilon_q} \approx \frac{dq}{d\varepsilon_q^p} = hG_0\left(\frac{(2.97-e)^2\sqrt{p'\,p_a}\left[(M/\eta) - e^{n\psi}\right]}{(1+e)\left[1-(dp'/dq)\eta\right]}\right) \tag{4-43}$$

In undrained tests, $d\varepsilon_v = 0$, which leads to following equation.

$$\frac{dq}{dp'} = \eta - \frac{3(1-2\nu)}{2G_0(1+\nu)}\left\{\frac{hG_0\left[(M/\eta) - e^{n\psi}\right]}{d}\right\} \tag{4-44}$$

$2G_0(1+\nu)/3(1-2\nu)$ can be obtained by fitting Equation (4-44) to the undrained p'–q curves.

If elastic response is very important, G_0 must be determined by some experimental methods. Otherwise, one may pick up a ν value first and then calculate G_0 and h. hG_0 or h, as we know, is reverse-proportionally related to the density of soil with parameters of h_1 and h_2 in the virgin loading case. Then h_1 and h_2 can be obtained with two different density experiments. h_3 control plastic modulus under during non-virgin loading and can be determined by best fitting $p - q$ or $p - \tau$ paths from undrained cyclic triaxial or simple shear tests.

d_2 is a parameter which characterizes the dilating response under the stress path of a constant stress ratio. The stress path of a constant stress ratio can be simulated by one-dimensional consolidation tests in which following relation exists.

$$\left(\frac{d\varepsilon_v}{d\varepsilon_q}\right)_{1D} = \left(\frac{d\varepsilon_v^e / d\varepsilon_q^p + D_2}{d\varepsilon_q^e / d\varepsilon_q^p + 1}\right)_{1D} = \frac{3}{2} \tag{4-45}$$

In the description of the model, we have known that d_2 and h_4 can be expressed as follows:

$$d_2 = D_2\left(\frac{M_c g(\theta)}{R} - 1\right)^{-1} \frac{|dp|}{dp} \tag{4-46}$$

$$h_4 = \sqrt{\frac{3}{2}} \frac{d\varepsilon_v^p}{dp} \frac{G}{d_2} \tag{4-47}$$

The sand model has been extensively verified through laboratory tests by Li & Dafalias (2000) and Li (2002).

CHAPTER5

MODEL IMPLEMENTATION

5.1 General

The Fast Lagrangian Analysis of Continua in 3 Dimensions (FLAC3D) developed by Itasca Consulting Group, Inc. is a widely used finite difference commercial code in the geotechnical field. It has been successfully used to numerically simulate a number of geotechnical problems. Besides many built-in soil constitutive models, it provides a user interface to implement new constitutive models. FLAC3D is therefore selected to implement the state dependent sand model.

5.2 Explicit, Dynamic Solution (EDS) Scheme

Numerical solution schemes face several difficulties when geomaterial models are implemented (Hart and Detournay, 2005). Three characteristics of geomaterials cause specific problems in implementing constitutive models.

1. Physical instability: Physical instability occurs in materials with softening behavior, such as rock, concrete and over-consolidated soils. The softening behavior occurs when the material fails and parts of it accelerate and the stored energy is released in the form of kinetic energy. Numerical solution schemes often have difficulties at this stage because the solution may fail to converge when a physical instability arises.
2. Path dependence of nonlinear materials: In most geo-mechanical systems, there are an infinite number of solutions that satisfy the equilibrium, compatibility and constitutive relations that describe the system. These solutions are corresponding to different stress paths, respectively. A correct solution needs to be identified for

the actual stress path. For example, if an excavation is made suddenly (e.g., by explosion) then the solution may be influenced by inertial effects that introduce additional failure of the material. This may not be seen if the excavation is made gradually. The numerical solution scheme should be able to accommodate different loading paths in order to apply the constitutive model properly.

3. Nonlinearity of the stress-strain relation. This is referred to as the dependence of the elastoplastic stiffness matrix on the stress state. The numerical scheme needs to be able to accommodate the various forms of nonlinearity.

In the Itasca series of software, an approach called explicit, dynamic solution (EDS) scheme is used. The above three characteristics of geo-materials, which cause difficulties in implementing the constitutive model, can all be addressed. The scheme allows the numerical analysis to follow the evolution of a geologic system in a realistic manner, without concerns about numerical instability problems. In the explicit, dynamic solution scheme, the full dynamic equations of motion are included in the formulation, and the static equilibrium state is reached by absorbing the energy in the system through inertial terms added in the formulation. During the 'collapse' failure process in softening materials, some of strain energy in the system is transferred into kinetic energy. The kinetic energy radiates from the source and dissipates through the inertial terms in the full dynamic formulations. Therefore, the numerical solution is always stable even when the system being modeled is unstable.

On the contrary, schemes that do not include inertial terms must use some numerical procedure to treat physical instabilities. Even if the procedure is successful at preventing numerical instability, the stress path taken may not be a realistic one.

However, the EDS scheme can follow the physical path and simulate the effect of the loading path on the constitutive response.

The EDS scheme also allows the implementation of strongly nonlinear constitutive models because the general calculation sequence allows the field quantities (velocities/displacements and forces/stresses) at each element in the model to be physically isolated from one another during one calculation step. This implementation in the general calculation sequence is described as follows.

The general calculation sequence for the EDS scheme is illustrated in Figure 5.1. The figure presents the calculation sequence of one loop calculation for one time step and for each tetrahedron element. In each sequence loop of the time step, the calculation solves two sets of equations: equilibrium of motion and constitutive relationships. The former is invoked to derive the new velocities and displacements from stresses and forces at each mass point. By application of the Gauss divergence theorem to the tetrahedron element, the derived velocities at each mass point are used to express the strain rates of the tetrahedron element. Then, the constitutive equations are used to calculate new stress from strain rates. The key feature here is that each box in Figure 5.1 updates all model variables from known values that remain fixed while control is within that box. For example, the lower box takes the set of velocities already calculated and, for each tetrahedron element, computes new stresses. The velocities and other variables are assumed to be frozen for the operation of the box, i.e., the newly calculated stresses do not affect the existing velocities. The assumption is valid provided the time step is so small that the calculated variables cannot propagate from one element to another during this time

step. This EDS approach makes the implementation of the non-linear constitutive model possible. All inputs of strain rates and other variables in one tetrahedron element, during the time step, they are fixed and not affected by the calculations in other elements. The stress increment calculation from strain rate is straightforward and there is no need to use any iteration process even if the constitutive law is highly nonlinear.

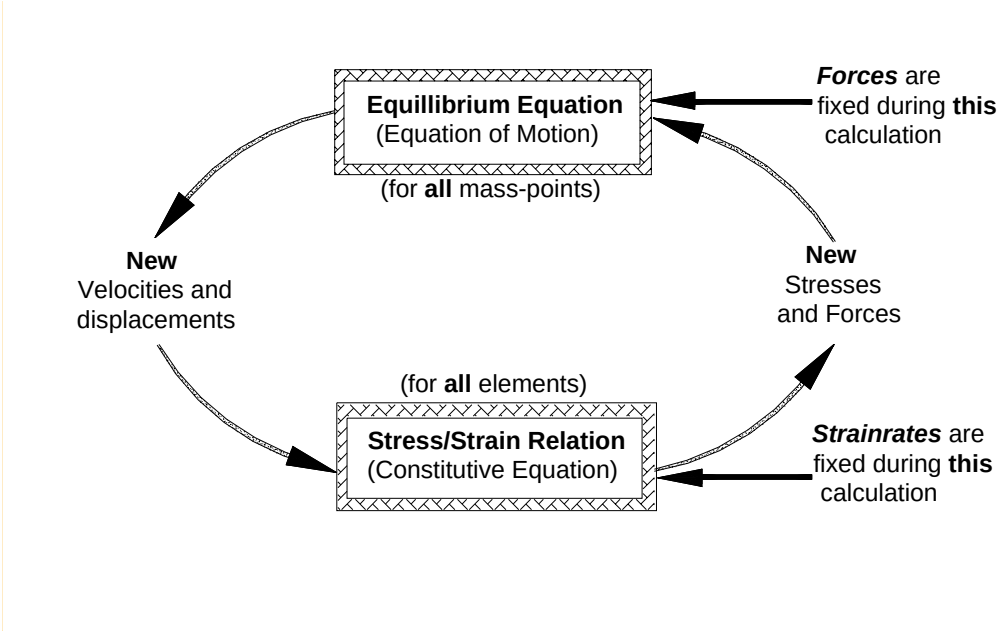

Figure 5.1 Calculation loop of EDS scheme in FLAC3D

5.3 Mechanical Time Step for Numerical Stability

The differential motion equations cannot provide valid answers unless the numerical scheme is stable. In FLAC, the idealized medium in the system is viewed as an assembly of point masses (located as the nodes) connected by linear springs. It was found from studying the oscillating mass-spring system with a finite difference

scheme that a time step must be used that does not exceed a critical time step related to the minimum eigenperiod of the total system. Similarly, The EDS scheme in implementing non-linear constitutive models requires that the time step is so small that the calculated variables cannot propagate from one element to another during the time step. Hence, the stability criterion for the numerical scheme must provide an upper bound for the values of the time steps used in the finite difference scheme.

In FLAC3D, a characteristic of the numerical scheme is that a uniform unit time step Δt is adopted for the whole system. And, the nodal masses in the motion equations are taken as variables and adjusted to fulfill the local stability conditions.

The one-dimensional, one series mass-spring system governed by the differential equation

$$-kx = m\frac{d^2x}{d^2t} \tag{5-1}$$

where k is the stiffness of the spring, and m is the point mass. The critical time step corresponding to a second-order finite difference scheme for the equation is given by

$$\Delta t = \sqrt{\frac{4m}{k}} \tag{5-2}$$

For an infinite series spring-mass case, the limit-stability criterion has the form

$$m = k(\Delta t)^2 \tag{5-3}$$

By selecting $\Delta t = 1$, the system will be stable if the magnitude of the point mass is greater than or equal to the spring stiffness. In FLAC3D, the validity of Equation (5-3) is extended to one tetrahedron by interpreting m as the nodal mass contribution m^l at local node l and k as the corresponding nodal stiffness contribution k^l. The nodal mass

contribution as derived from the infinite series criterion provides an upper-bound value for the system under consideration. In order to obtain a stable numerical scheme, the nodal mass contribution should be given a value that is equal to or larger than the nodal stiffness contribution. By a simple diagonalization technique of the local stiffness matrix, the nodal stiffness contribution at local node *l* is given by

$$k_{qq} = \frac{\alpha_1}{9V}\left[n_q^l S^l\right]^2 \tag{5-4}$$

where $\alpha_1 = K + 4/3G$, K is the bulk modulus, and G is the shear modulus. No summation is implied on repeated index q of k_{qq}, which runs from 1 to 3. Then the upper-bound value for the nodal stiffness contribution can be expressed as:

$$k^l = \max(k_{11}, k_{22}, k_{33}) \tag{5-5}$$

which yields the expression for the tetrahedron mass contribution at node *l*:

$$m^l = \frac{\alpha_1}{9V}\max\left(\left[n_i^{(l)} S^{(l)}\right]^2, i = 1,3\right) \tag{5-6}$$

to provide a numerically stable solution.

5.4 Mixed Discretization

The EDS scheme in FLAC3D is set up on the basis of tetrahedron elements. The tetrahedron element is a constant strain-rate, three-dimensional element and it has the advantage of not generating hourglass deformation compared to other constant strain-rate elements. However, these elements do not provide for enough modes of deformation. For example, they cannot deform individually without change of volume as required by certain important constitutive laws and exhibit an over-stiff response as compared to that expected from the theory. To overcome this problem, a process of mixed Discretization is applied in FLAC3D.

For the mixed discretization technique, more volumetric flexibility is applied to an element by proper adjustment of the first invariant of the tetrahedral strain-rate tensor. A coarser discretization in zones is superposed on a finer tetrahedral discretization. Then, the technique is accomplished by assigning the first strain-rate invariant and the first stress tensor invariant of any particular tetrahedron as the volumetric-average over all tetrahedra elements in a zone. As shown in Figure 5.2, the individual tetrahedron will not keep constant volume when subjected to the pattern of deformation, however the total volume of the assembly of the tetrahedral elements (i.e. the zone) remains constant under that deformation pattern.

In FLAC3D, the discretization starts with zones. Then, each zone is internally discretized into tetrahedral elements. An eight-node zone, for instance, can be discretized into two different configurations of five tetrahedral elements (corresponding to overlay1 and overlay2 in Figure 5-3). The calculation of nodal force can be carried out using one overlay or a combination of two overlays. The advantage of the two-overlay approach is to ensure symmetric response for symmetric loading.

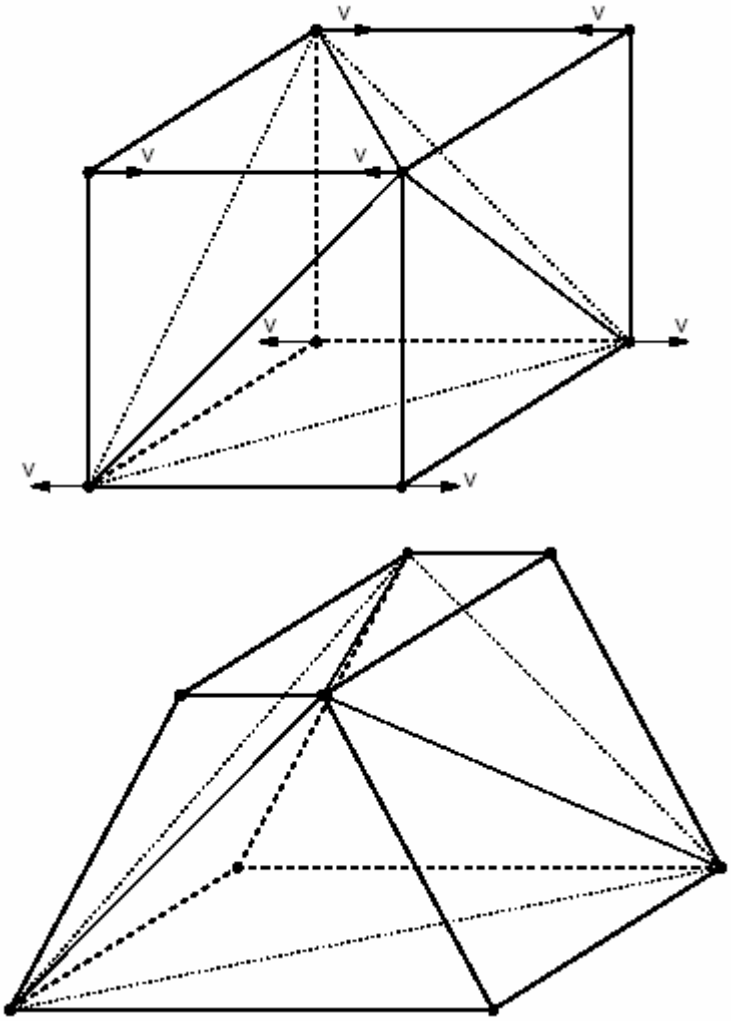

Figure 5-2 Deformation model for which mixed discretization would be most efficient

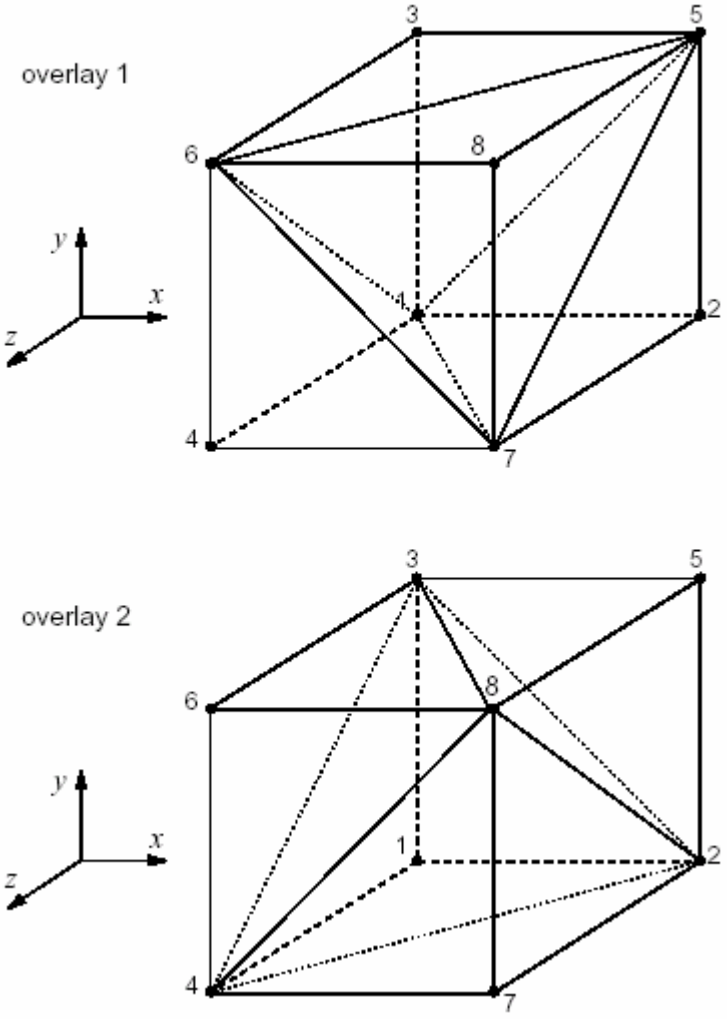

Figure 5-3 An 8-node zone with 2 overlays of 5 tetrahedra in each overlay

5.5 Model Implementation

External constitutive models can be written in C++ and compiled as DLL (dynamic link library) files that can be loaded whenever it is needed in FLAC3D simulation. The main function of the constitutive model is to return new stresses, given

strain increments. C++ is an object-oriented computer language using classes to represent objects. The data associated with an object are encapsulated by the object and are invisible outside the object. Communication with the object is by member functions that operate on the encapsulated data. In addition, there is strong support for a hierarchy of objects. New object types may be derived from a base object and the base-object's member functions may be superceded by similar functions provided by the derived objects. This arrangement confers a distinct benefit in term of program modularity and the program can access the derived classes through the base objects.

The emphasis of the object-oriented approach of C++ is to provide a base class that includes a framework for implementing constitutive models, which are classes derived from the base class. The base class, called 'ConstitutiveModel', is termed an 'abstract' class because it declares a number of 'pure virtual' member functions. This means that no object of the base class can be created and that any derived-class object must supply real member functions to replace each of the pure virtual functions of the base class. The methodology of writing a constitutive model in C++ for operation in FLAC3D includes descriptions of the base class, member functions, registration of models, information passed between the model and FLAC3D, and the model state indicators. The implementation is achieved by supplying real member functions to replace each of the pure virtual functions of the base class.

A member function " const char *Run(unsigned uDim, State *ps)" as a main interface is called for each sub-zone (up to ten per zone for a two-overlay case) at each cycle from within FLAC3D's zone scan. The model is coded within the member function and updates the stress tensor from the strain increment tensor for each sub-zone at each

cycle. The structure “ps” contains the current stress components and the computed strain increment components for the sub-zone being processed. For each sub-zone cycle, besides updated stress tensor, the state parameters must also be returned .

As opposed to the implementation of constitutive models based on the conventional plasticity, the trial-and-correction approach, which is adopted by all built-in models implementation in FLAC3D manual, is not used in the implementation of state-dependent bounding surface constitutive model. This is because the yielding surface that defines the pure elastic deformation range doesn’t occur in the bounding surface models. The main objective of the current model implementation is to calculate the elastoplastic stiffness matrix Λ_{ijkl} shown in Equation (3-26). Another difference is that some state parameters in the current model, such as the projection center, need to be updated in each cycle for each zone.

The flow chart for programming the state dependent sand model is shown in Figure 5.4. This program is included in the member function “ const char *Run(unsigned uDim, State *ps)”. Each tetrahedral element calls this member function for each cycle to update the stress state of the tetrahedron. After all tetrahedral elements in the zone are scanned, the state variables of the zone are modified according to the rule of the mixed discretization scheme. However, the modification of the stress state of the zone will be left for FLAC3D. The member function ConfineModulus(void) is used to return a value for its best estimate of the maximum confined modulus. This is used to determine the stable time step.

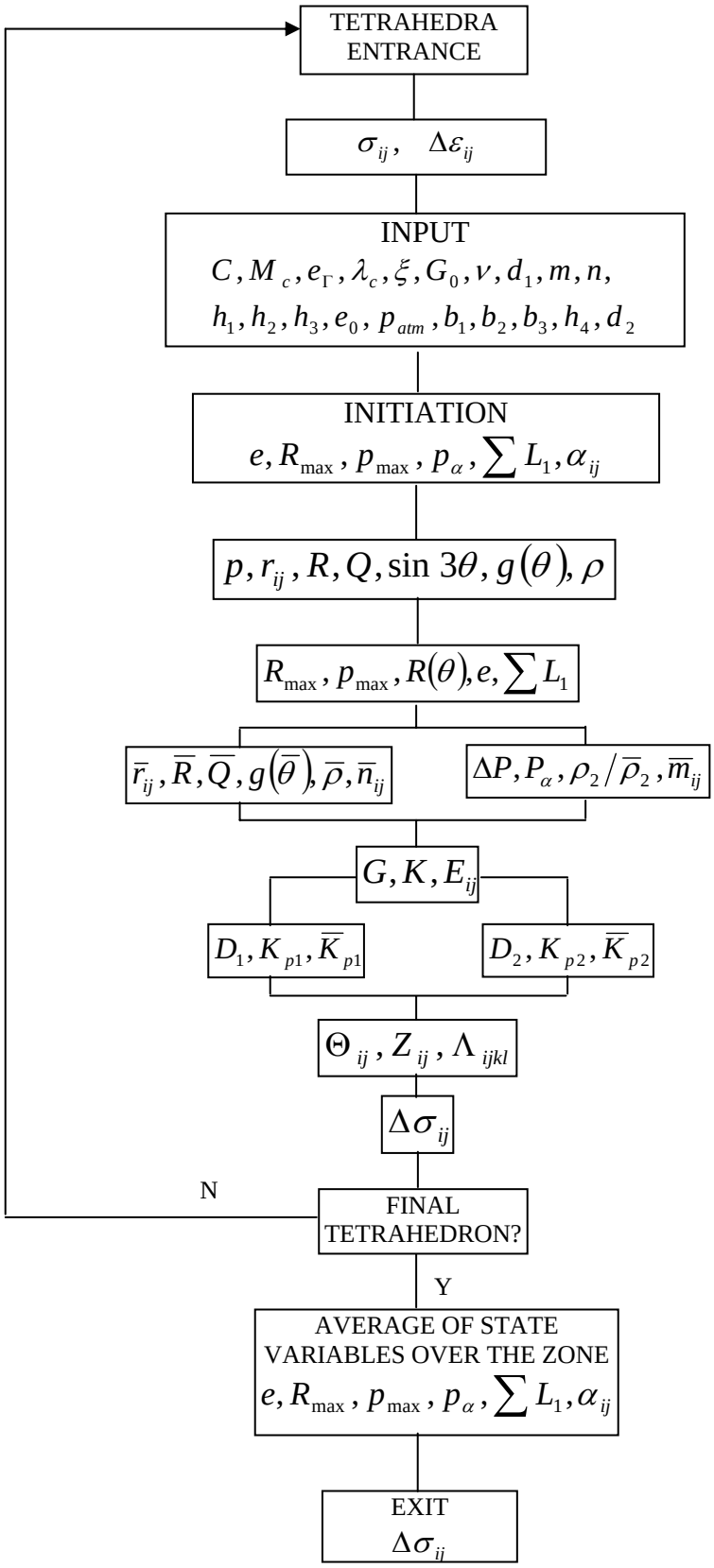

Figure 5-4 Flow chart for coding the constitutive model

CHAPTER 6

FLAC 3D MODEL VERIFICATION

The constitutive model implemented into the FLAC3D program was verified first by simulating a number of test results on Toyoura, Ottawa, and Fontainbleau sands. The FLAC 3D discretization was then verified using the full scale loading test result on a 4-pile micropile group conducted by the FOREVER program.

6.1 Stress path and deformation of Toyoura Sand

Li (2002) and Li and Dafalias (2000) have shown the constitutive model to predict the behavior of Toyoura sand under various test conditions. This prediction is repeated first to ensure that the FLAC 3D model coding was done properly. This study is restricted to the simulation of drained element tests with special emphasis on the effects of initial void ratio and Lode angle on sand behavior.

Three common shear modes which include conventional triaxial compression (TC), triaxial extension (TE) and plane strain compression (PS) were selected. An isotropic stress of 300 kPa was set as the initial stress state in all simulations. Two relative densities of 65% and 15% corresponding to “dilative” and “contractive” states, respectively, were used. The predicted response of the two specimens under the different shear modes are as shown in Figures 6-1 and 6-2, respectively.

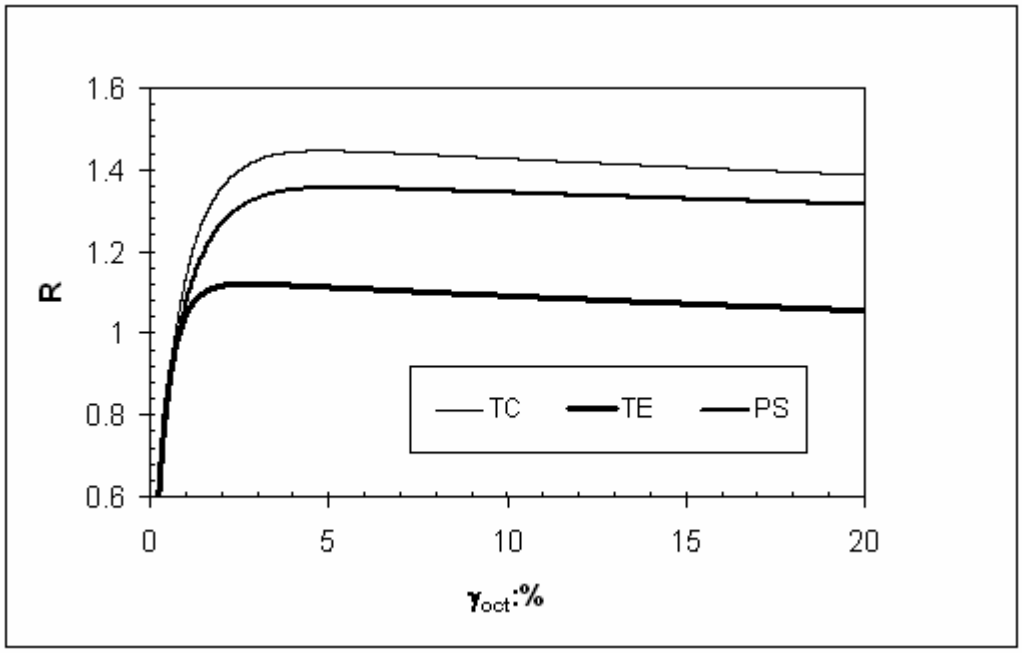

A. Stress ratio invariant response

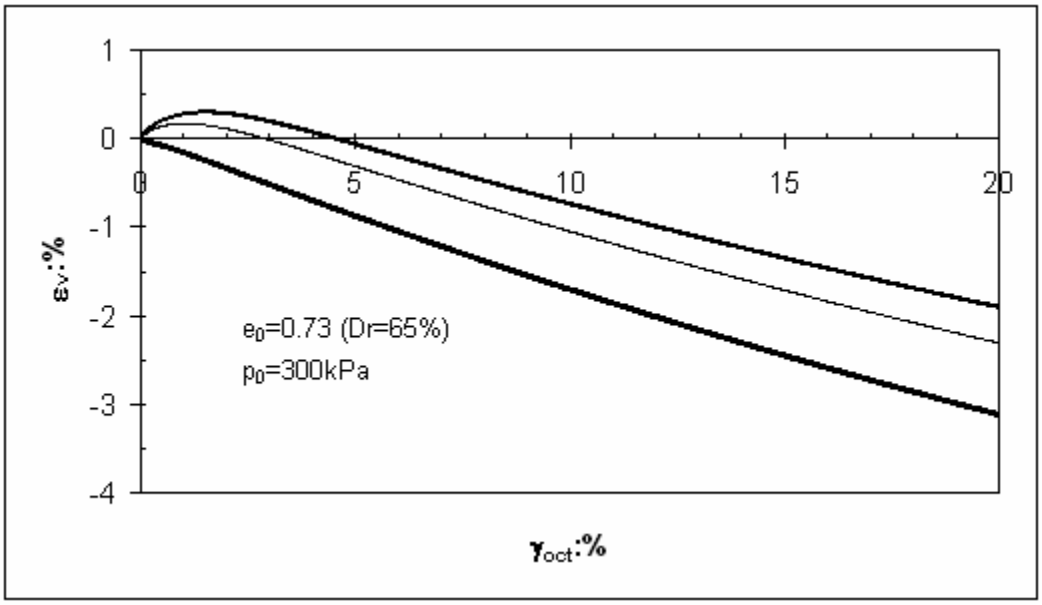

B. Volumetric strain response

Figure 6-1. Drained response of dense sand under various shear modes (D_r = 65%)

The set of model constants listed in Table 6-1 was used in the simulations.

Table 6-1 Model parameters for Toyoura sand (Li, 2002)

Elastic parameters	Critical state parameters	Parameters associated with dr-mechanisms	Parameters associated with dp-mechanisms	Default parameters
G_0=125 ν=0.25	M=1.25 c=0.75 e_I=0.934 λ_c=0.019 ξ=0.7	d_1=0.41 m=3.5 h_1=3.15 h_2=3.05 h_3=2.2 n=1.1	d_2=1 h_4=3.5	a=1 b_1=0.005 b_2=2 b_3=0.001

In the figures γ_{oct} is the octahedral shear strain and R is the stress ratio invariant defined earlier (Eq. 4-6). The predictions were identical to those values predicted by Li and Dafalias (2000). It is evident from the figures that the dense sand dilates with a peak stress ratio greater than critical stress ratio, and the loose sand contracts without such a peak. Different Lode angles associated with the shear modes also result in different peak and critical state stress ratios in terms of the invariant, *R*.

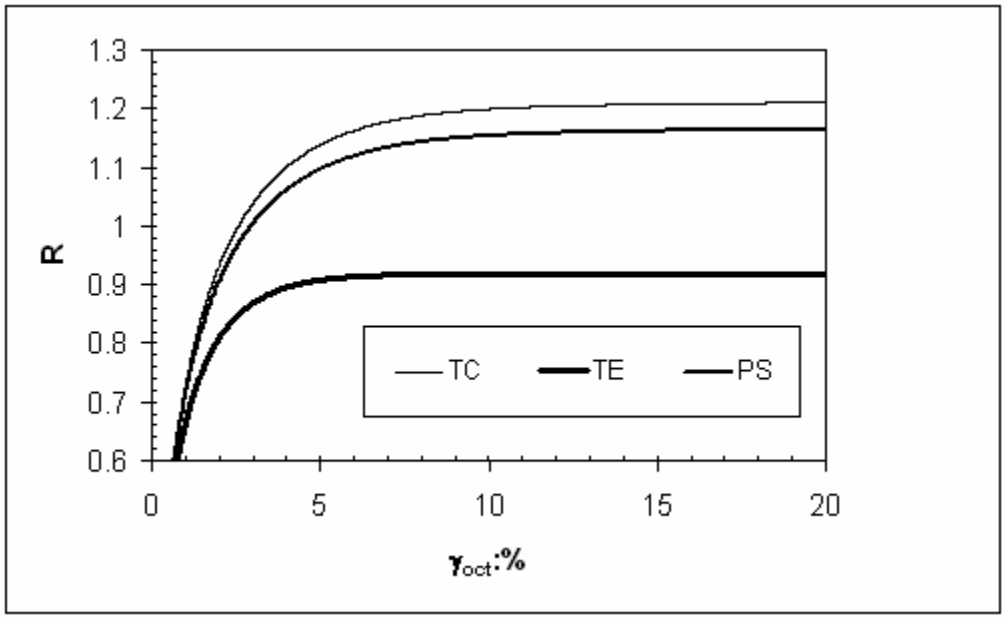

A. Stress ratio invariant response

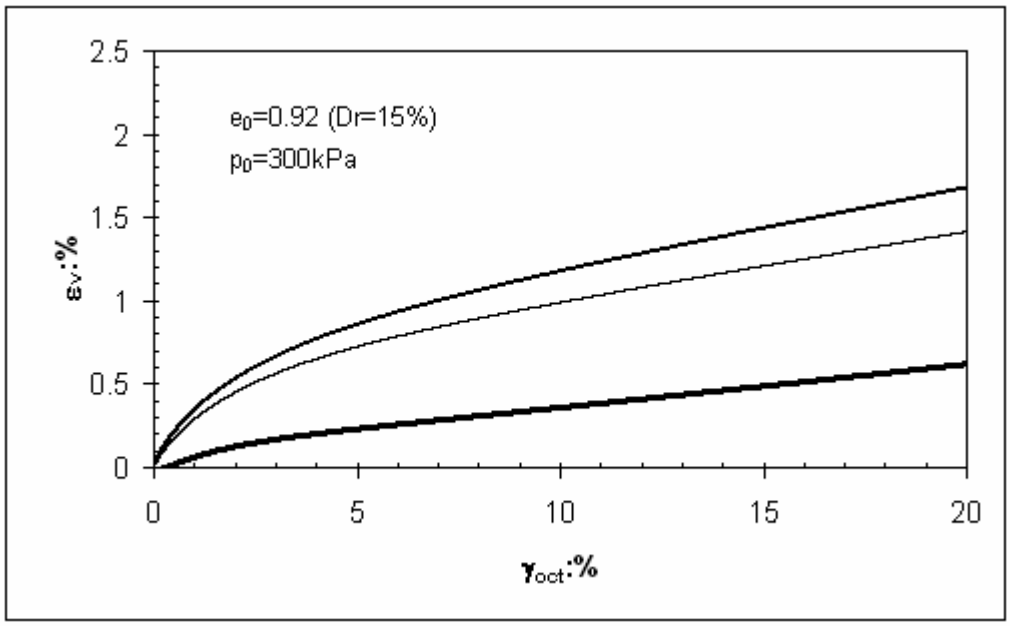

B. Volumetric strain response

Figure 6-2. Drained response of loose sand under various shear modes (D_r = 15%)

6.2 Ottawa Sand Tests

The FLAC3D model was also used to verify some triaxial tests conducted on Ottawa F-35 sand at Washington State University (Olcott, 2001). This sand is manufactured by U. S. Silica from Ottawa, Illinois and is a silica sand consisting of mostly rounded grains with a specific gravity of 2.65, a mean grain size of 0.44mm, a coefficient of uniformity of 1.51 and coefficient of curvature of 0.97.

The parameters for the model were determined using the procedure outlined in Chapter 4. Olcott (2001) established the critical state line in the in *e-lnp′* space. It is transformed onto the straight line in e-p^{ξ} space as shown in Figure 6-3 and a best fit line drawn to determine the critical state parameters e_Γ, λ_c and ξ (Eq. 4-29). M_c *and* M_e for this sand were reported as 1.14 and 0.85, respectively (Olcott, 2001). Thus, $C=M_e/M_c$ = 0.75.

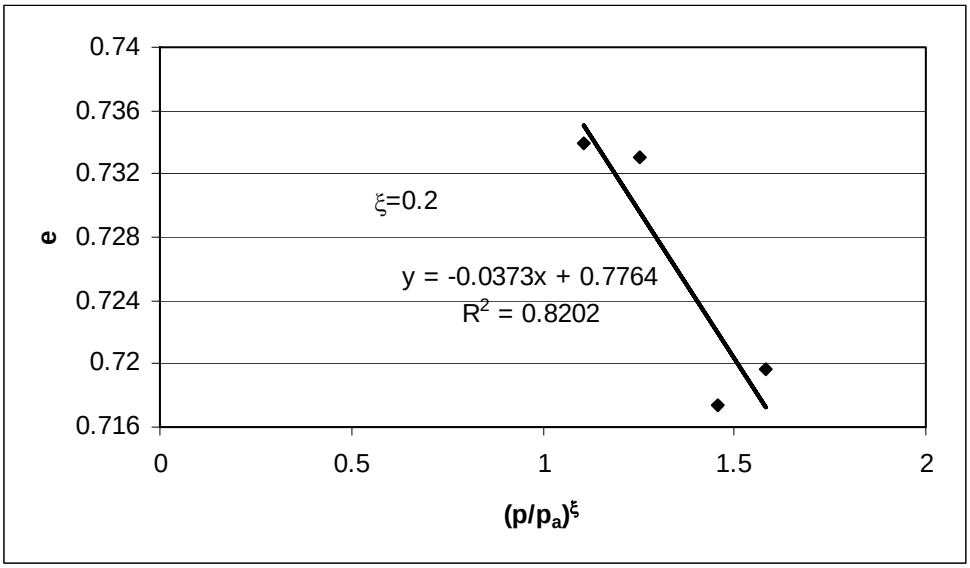

Figure 6-3 Critical state line in e-p^{ξ} space

The parameter *m* (Eq. 4-40) is determined from undrained tests. The typical stress path of undrained tests of Ottawa sand is as shown in Figure 6-4. Using the values of M_d,

and ψ_d for the phase transformation state, m can be calculated and its average is shown in Table 6-2.

Table 6-2 Determination of parameter m

Initial pressure (p', kpa)	Void ratio	M_d	ψ_d	m	Average of m
100	0.719	1.06	-0.0182	5.2	4.4
300		1.13	-0.0152	0.56	
400		0.94	-0.0298	7.34	

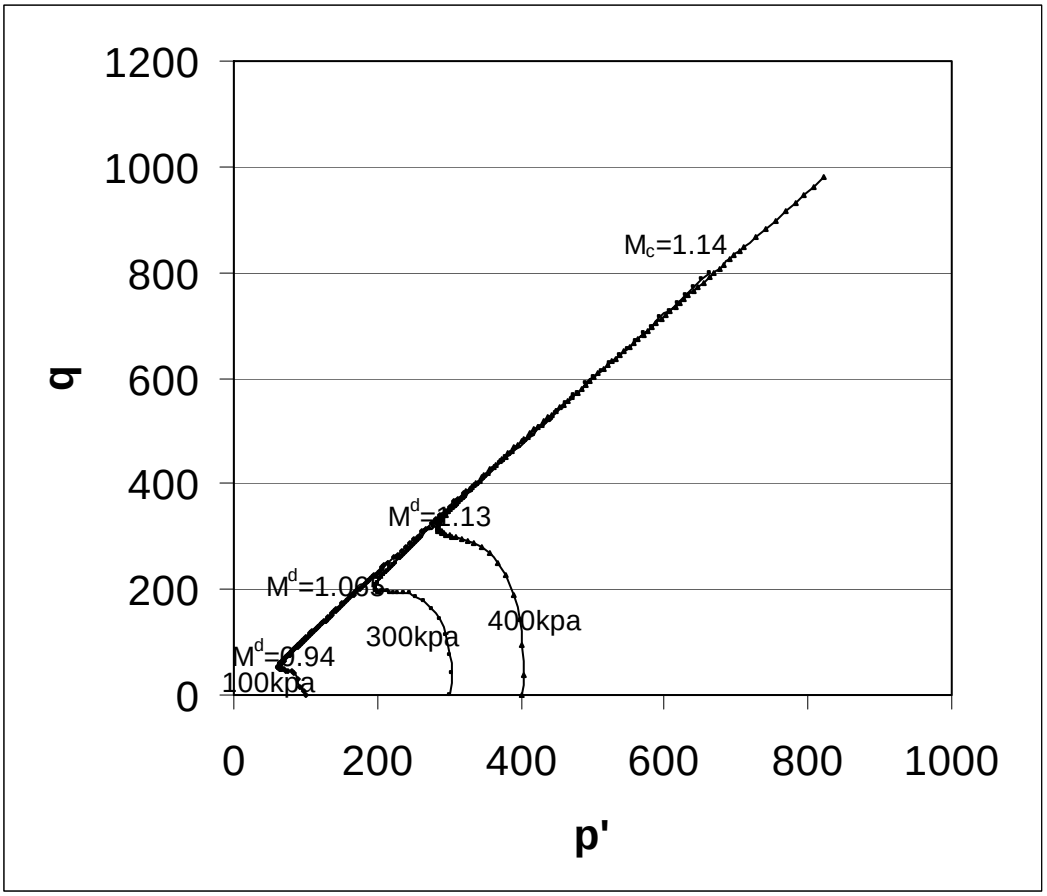

Figure 6.4 Stress path of undrained tests of Ottawa sand

Similarly the parameter *n* (Eq. 4-41) can be calculated and its average is as shown in Table 6-3.

Table 6-3 Determination of parameter *n*

Initial pressure (p', kpa)	Void ratio	M^b	ψ^b	*n*	Average of *n*
200	0.67	1.246	-0.0337	2.64	2.64
600		1.251	-0.035	2.64	

The parameter d_1 (Eq. 4-42) is determined by plotting the ratio of $\frac{d\varepsilon_v^p}{d\varepsilon_q^p}$ against $\left(e^{m\psi} - \frac{\eta}{M}\right)$ as shown in Figure 6-6.

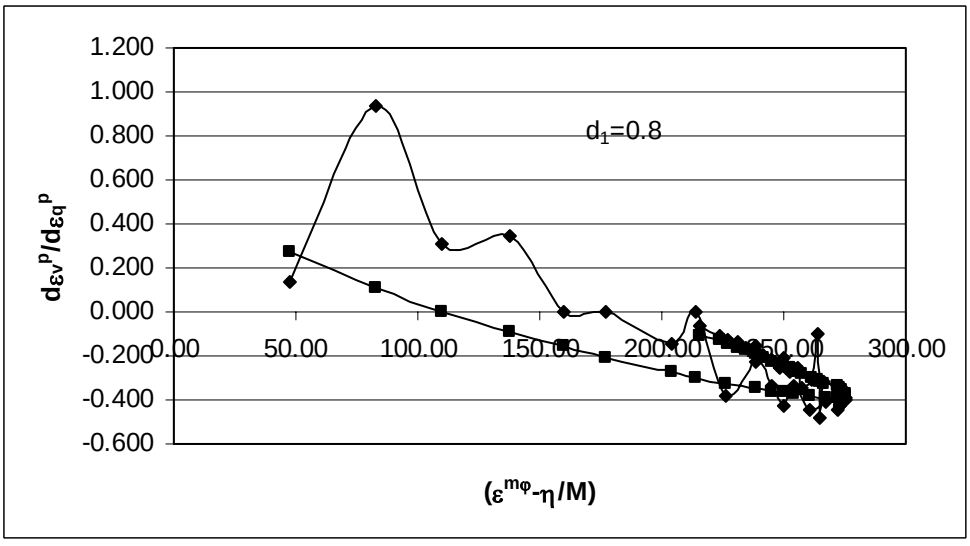

Figure 6.5 Determination of parameter d_1

Finally, the parameters h_1, h_2, h_3, d_2 and h_4 are empirically determined. The complete set of model parameters for Ottawa sand is shown in Table 6-4.

Table 6-4. Model parameters for Ottawa sand

Elastic parameters	Critical state parameters	Parameters associated with dr-mechanisms	Parameters associated with dp-mechanisms	Default parameters
G_0=60 ν=0.29	M=1.14 c=0.75 e_τ=0.776 λ_c=0.037 ξ=0.2	d_1=0.8 m=4.4 h_1=3.9 h_2=1.0 h_3=2.2 n=2.6	d_2=0.5 h_4=4.5	a=1 b_1=0.005 b_2=2 b_3=0.001

Drained tests corresponding to two initial states of the samples were selected to verify the model. The first initial state is 100 kPa effective isotropic stress and 0.644 void ratio and the second one is 600kPa effective isotropic stress and 0.73, which represent dilative and contractive states, respectively.

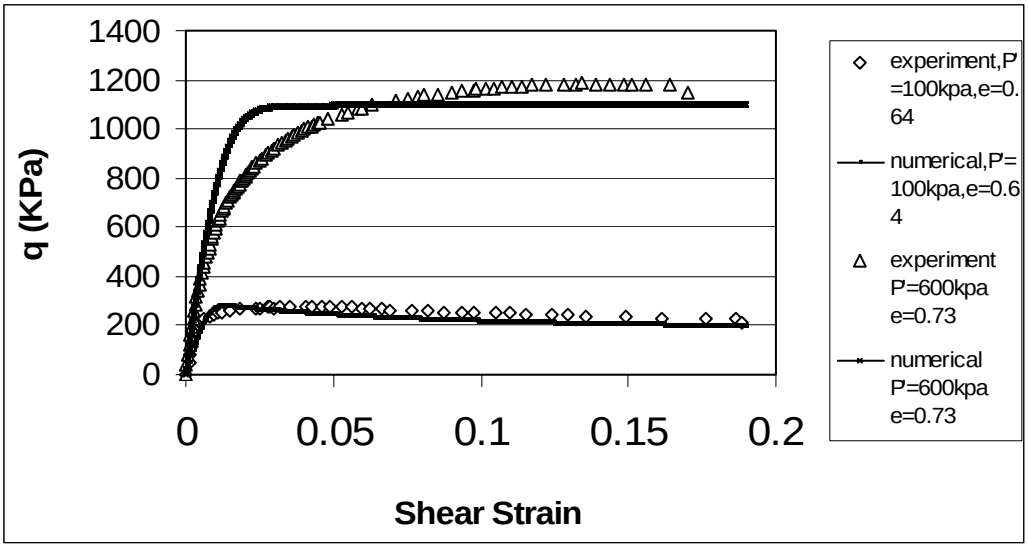

A. Stress strain response

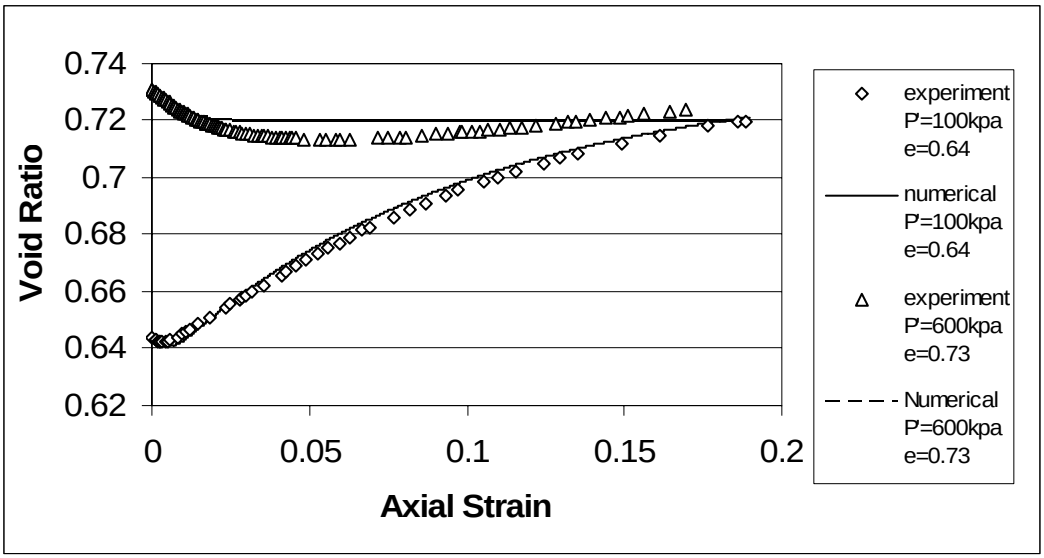

A. Void ratio response

Figure 6.6 Drained tests on Ottawa Sand

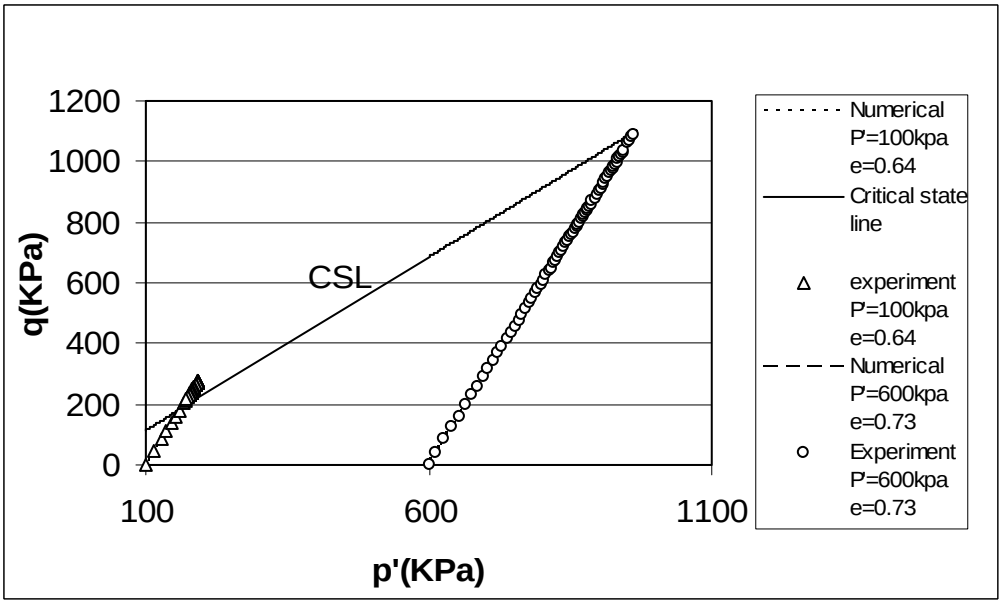

Figure 6.7 Stress path changes in Ottawa sand.

The predicted stress strain response and the stress path variation of the samples under triaxial compression are shown in Figures 6-6 and 6-7, respectively. It can be seen that the FLAC3D results match the test results well.

6.3 Fontainebleau Sand Tests

The full scale tests on micropiles by the FOREVER program were conducted on Fontainebleau sand. Since the critical state parameters were not available, it was decided to deduce them from basic index tests. The grain size distribution and the relevant characteristic of Fontainebleau sand are as shown in Figure 6-8 and Table 6-5 (Mendonca and Lopes, 2004). It was found that the grain size distribution and characteristics of Fontainebleau sand are very close to Toyoura sand (Table 6-5 and Figure 6-8). Since model parameters for Toyora sand were known already, it was decided to simulate Fontainbleau sand using the properties of the former.

Gaudin et. al. (2002) performed compression tests on Fontainebleau sand behavior carried out using a standard triaxial device in drained conditions with one or more cycles of unloading-reloading under initial effective mean stress of 90kPa, 60 kPa and 30 kPa. The initial relative density of the specimen was 71%. The stress strain response of the loading and unloading of this sand using the FLAC3D model is as shown in Figure 6-9. It is evident that the model with Toyoura sand properties captures Fontainbleau sand behavior well for all initial states.

Table 6-5. Comparison of Fontainebleau sand and Toyoura sand

	γ_s (kN/m^3)	e_{max}	e_{min}	D_{50} (mm)	C_u	Cc
Fontainebleau	26	0.844	0.527	0.17	1.57	0.64
Toyoura	26	0.973	0.609	0.19	1.25	1.01

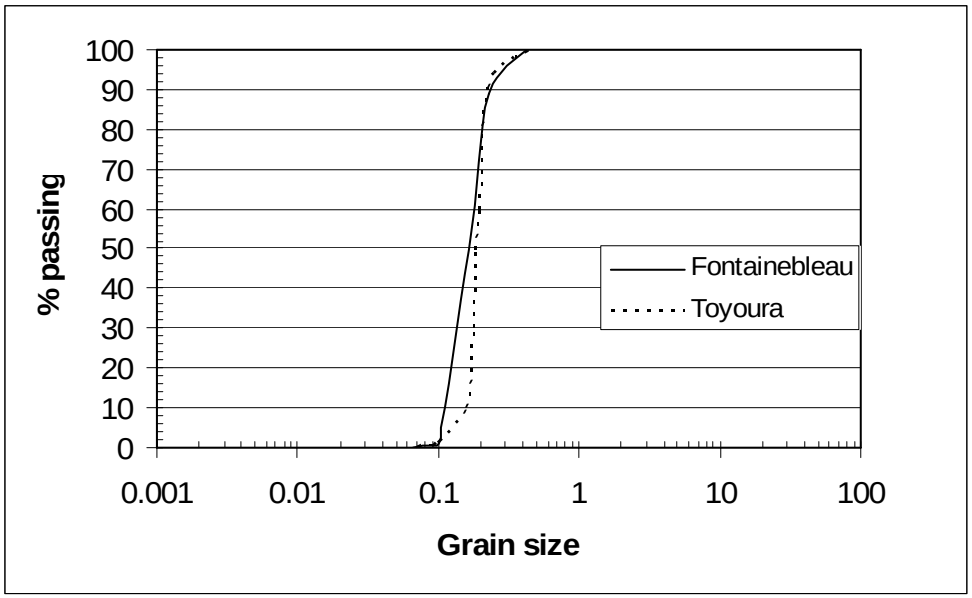

Figure 6.8 Grain size distribution of Fontainebleau sand and Toyoura sand

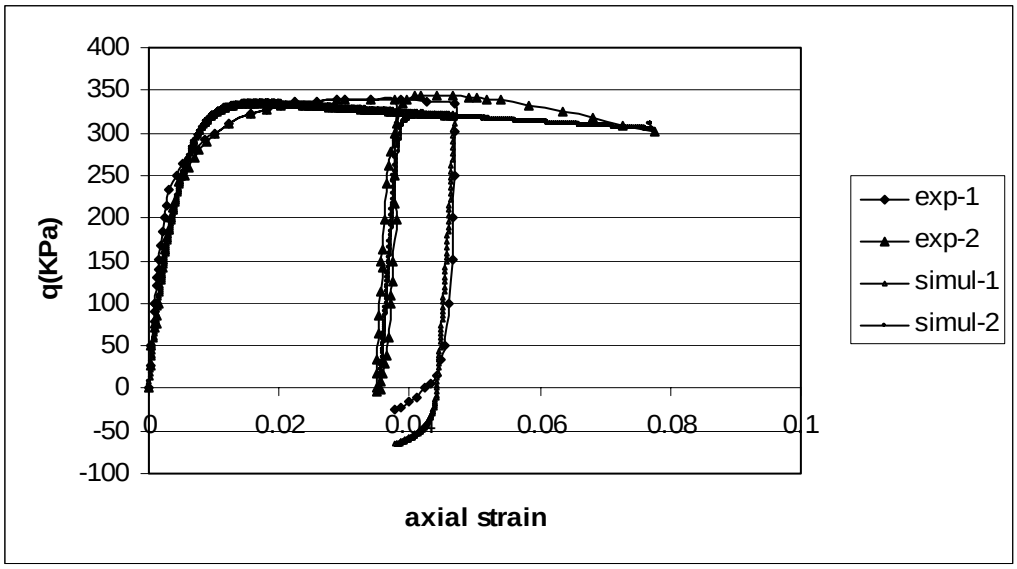

A. P=90 kPa

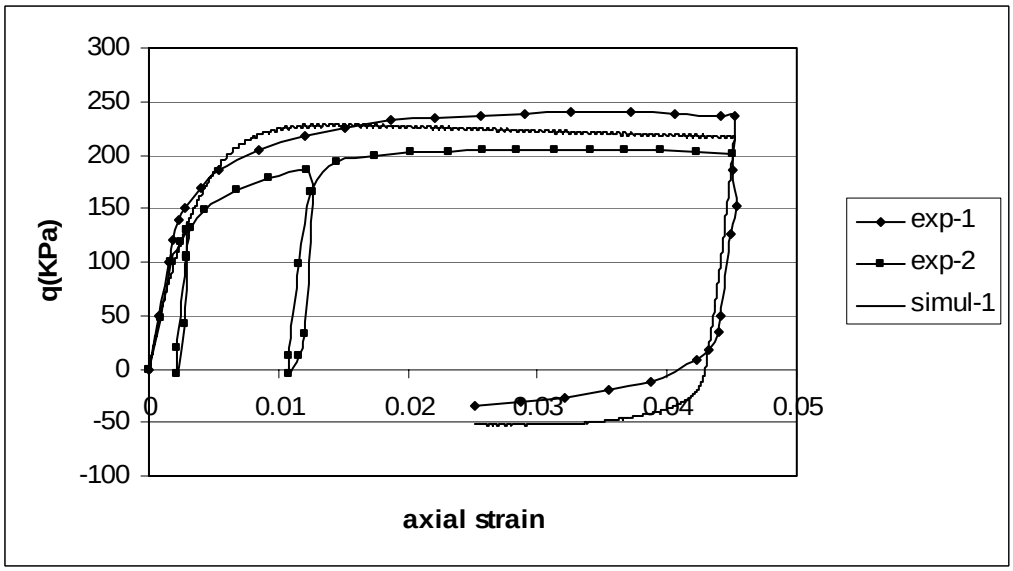

B. P=60 kPa

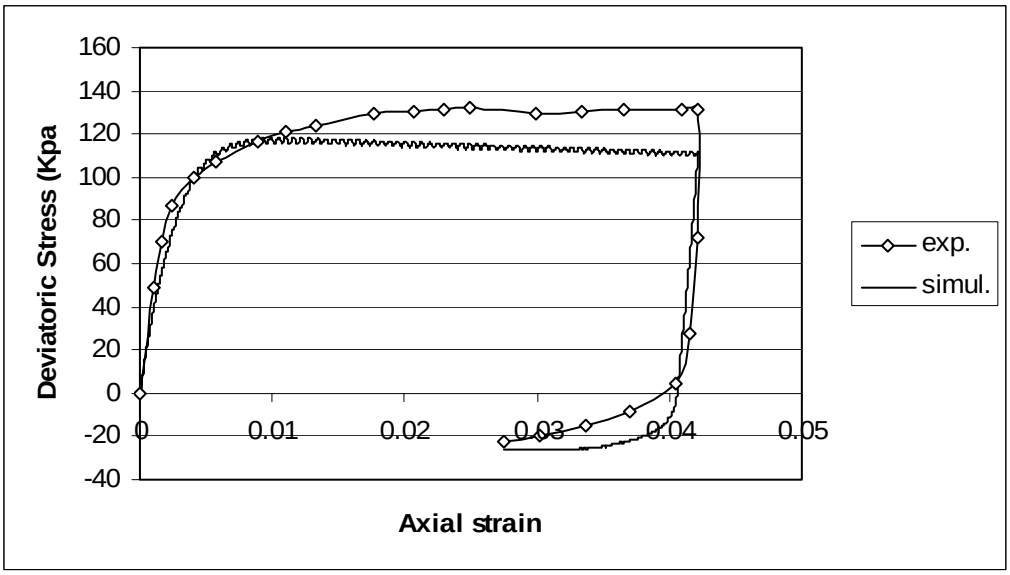

C. P=30 kPa

Figure 6.9. Response of deviatoric stress from experiments and simulation

6.4 Case Study of Micropiles

Full-scale load tests of micropiles were conducted by the French research program FOREVER. These tests, as mentioned before, were conducted on homogeneous Fontainebleau sand. The data corresponding to the group of 4 micropiles which were gravity grouted and tested under vertical loading was selected to verify the FLAC3D discretization.

The site was homogeneously backfilled to a height of 6m with Fontainebleau sand and the micropiles were installed as shown in Figure 6-10. The principal characteristics of the fine Fontainebleau sand and the micropiles are:

Fontainbleau Sand:

Dry Density: $14.4kN/m^3<\gamma_d<14.82kN/m^3$

Density Index: $0.53<I_D<0.62$

Water content: 7.9%<w<10.8%

Micropiles:

Anchored length: L=5m

Diameter: B=100mm

Steel tube: diameter 50/40mm

With $E_{steel}=2.10^5$MPa

$E_{grout}=10^4$Mpa

4 micropiles were distributed in a square pattern with a spacing of 2 diameters.

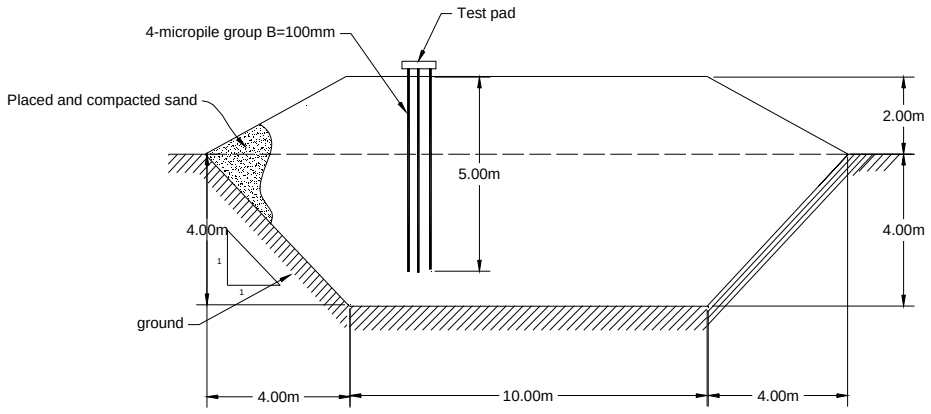

Figure 6-10. Micropile layout of the experiment (FOREVER, 2002)

The numerical simulation of the pile load test was performed using FLAC3D with the state-dependent sand model. A finite difference mesh including a 2×2 micropile group was prepared. Micropiles were simulated through the pile structure element provided by FLAC3D. The normal and shear properties of the soil-pile interface were buit-in as elastic-perfectly plastic in FLAC3D and cannot be altered by the users. The

parameters of the micropiles and the interfaces are shown in Table 6-4. The Fontainbleau sand was assumed to have the properties described earlier.

Table 6.6. Parameters of soil-pile interfaces and piles

Elastic modulus (piles, Pa)	Poisson ratio (pile)	Normal stiffness (N/m^2)	Shear stiffness (N/m^2)	Shear friction angle	Shear cohesion
2.71×10^{10}	0.3	1.5×10^{10}	7.5×10^{9}	20	0

The simulated displacement-loading relationship is plotted along with the in-situ experimental relation (Figure 6-11). It can be seen that the simulation captures the behavior well.

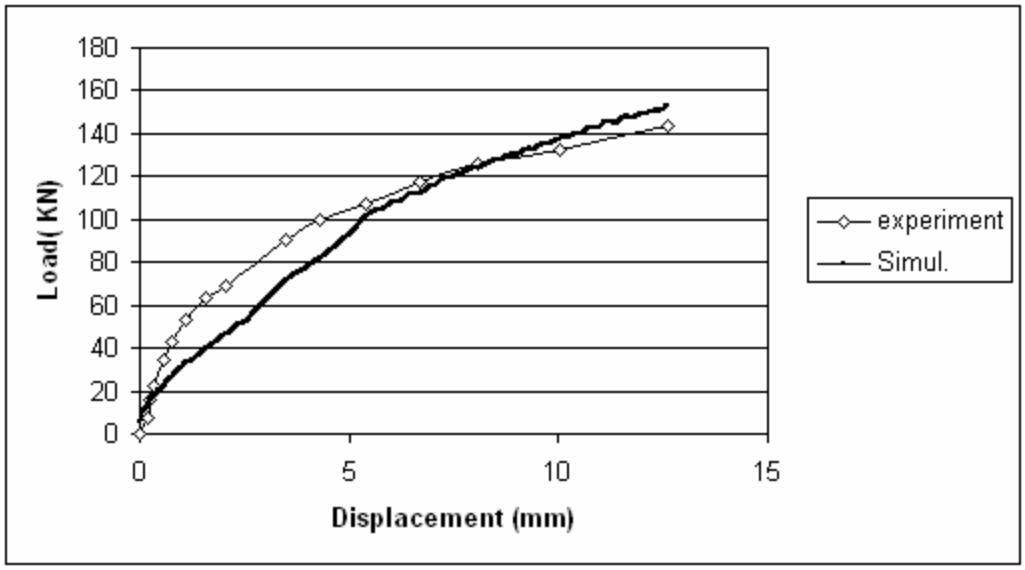

Figure 6.11. The experimental and simulated load-displacement relation of single micropile

CHAPTER 7

ANALYSIS OF MICROPILE PERFORMANCE

The state of sand around micropiles is determined by the combination of both density and effective mean pressure. However, the mechanical properties for sand in pile design are currently based only on the relative density alone. Use of this parameter alone in full scale test results cannot replicate the important effects of confinement. This has resulted in conflicting results with regard to the interpretation of test results. The use of the state parameter, ψ, a measure of the combination of density and effective stress, would provide a means of quantifying the results better. Sands with $\psi < 0$ are dilative and those with $\psi > 0$ are contractive under shear loading. Thus, their mechanical properties and their contribution to pile resistance will be different. Note that sand with $\psi = 0$ are at the critical state with no changes in volume and its mechanical properties are controlled by critical state friction only.

This chapter makes use of the state dependent sand model implemented in FLAC3D to study the performance of micropiles under vertical loading. The first set of analyses was performed for a single pile. The analyses were extended later to group of piles and a network group of piles, respectively. Attention is focused on external (i.e. ground-related) carrying capacity influenced by the sand state rather than the capacity controlled by the selection of the pile components and grouting process. It is noted that these latter processes have also been shown to be significant in micropile design (Juran 1999). Furthermore, micropiles are discretized as structural elements as in the case of conventional piles, but with a smaller diameter.

7.1 Effect of Sand State on Resistance of a Single Pile

7.1.1 Model Setup

The dimensions of the model were selected as $5\times5\times10m^3$ and the finite difference mesh utilized consisted of 8960 elements and 10404 nodes (Fig. 7.1). The pile is assumed to be installed in a homogenous profile of uniform Toyoura sand. The model parameters of Toyoura sand are as shown in Table 5-1. The initial state parameter of the sand is assumed to be uniform; hence, the void ratio distribution with depth is varied. Figure 7.2 shows the void ratio distribution for a $\psi = 0$ model as an example.

The micropile considered is of Case 1 with pile structure elements linked to the soil by normal and shear interface springs. The length and diameter of pile are chosen to be 6m and 200mm, respectively, corresponding to $L/D = 30$. Innovative drilling and grouting methods are utilized in modern micropile installation. This results in high grout/ground bond along the periphery of the micropiles. Thus, the normal and shear stiffness and strength of the interface in the FLAC3D model are preset with values large enough to ensure that the deformation and failure of a micropile is controlled by the surrounding soil and not by the interface when the micropile is subjected to vertical loads.

The vertical loads were applied by displacement control as specified in the FLAC3D manual. Small values of continuous vertical displacements were applied to the top node of the pile to trigger the side and tip resistance of micropiles from the surrounding soil. Note that since the L/D of micropiles is high, a major contribution to its

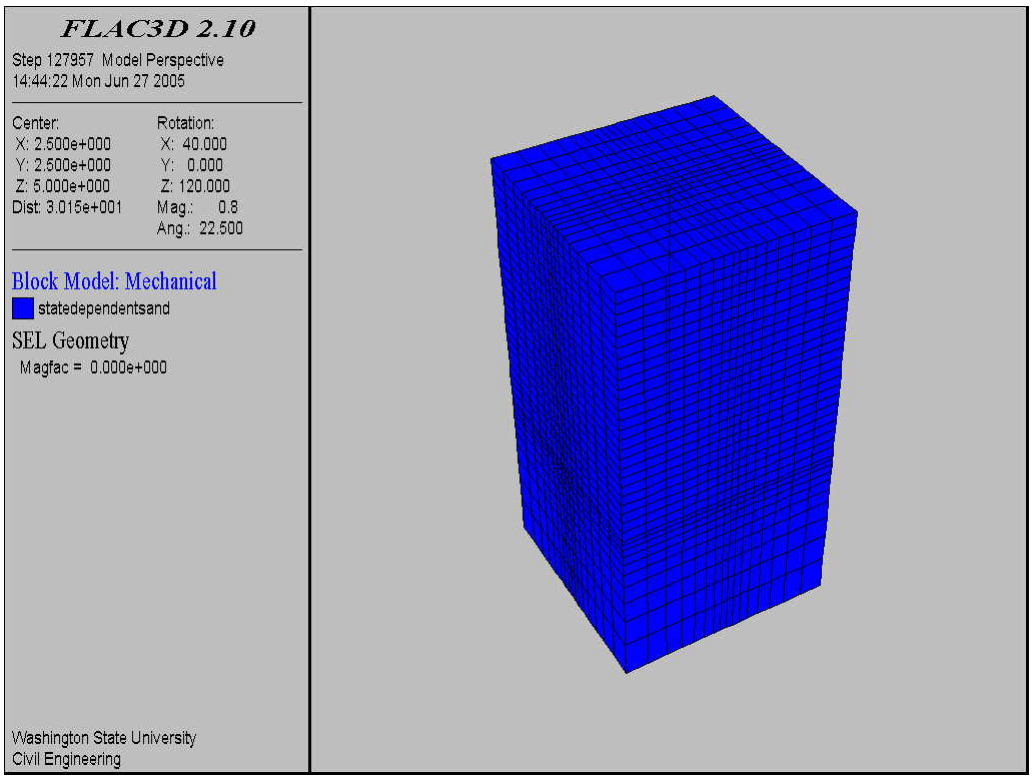

Figure 7.1 Finite difference mesh

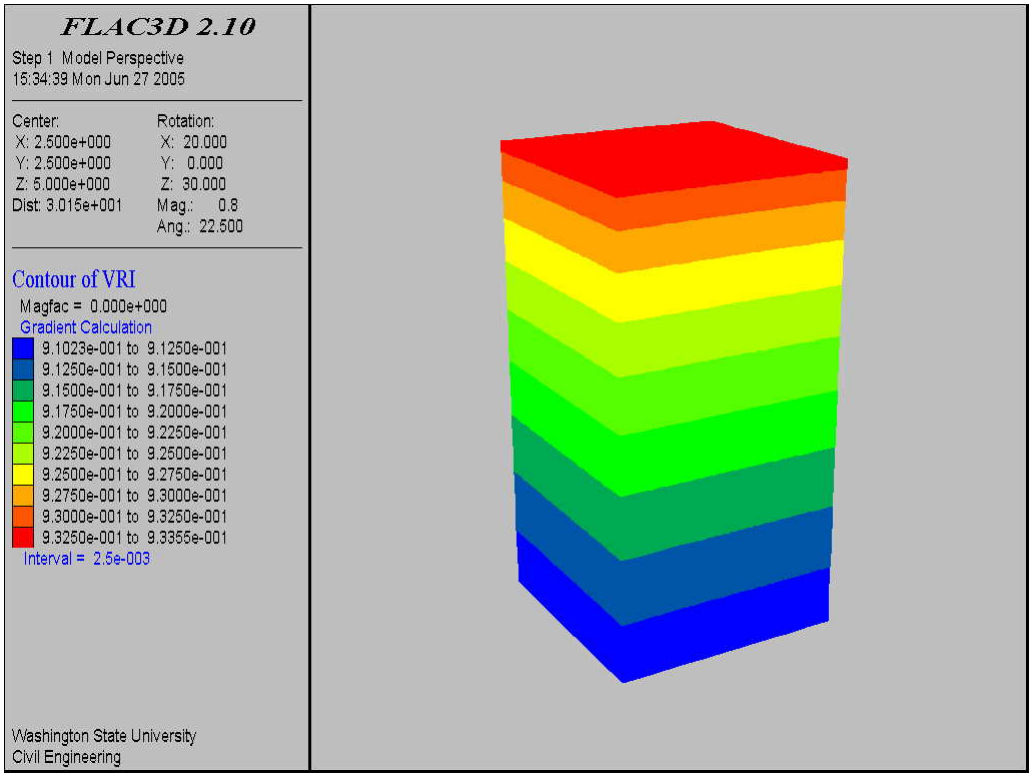

Figure 7.2 Void ratio distribution of TOYOURA sand model for ψ=0

capacity comes from friction. However, we also focus on tip resistance to examine the effects of state parameters on its variation.

7.1.2 Results

The variation of the side and tip resistance of the pile with displacement is as shown in Figures 7.3 and 7.4, respectively. The state parameter values of 0.1, 0.0, -0.1, and –0.2 were chosen to represent contractive as well as dilative behavior of sand. It can be seen that the both side and tip resistance are dependent on the state parameter values.

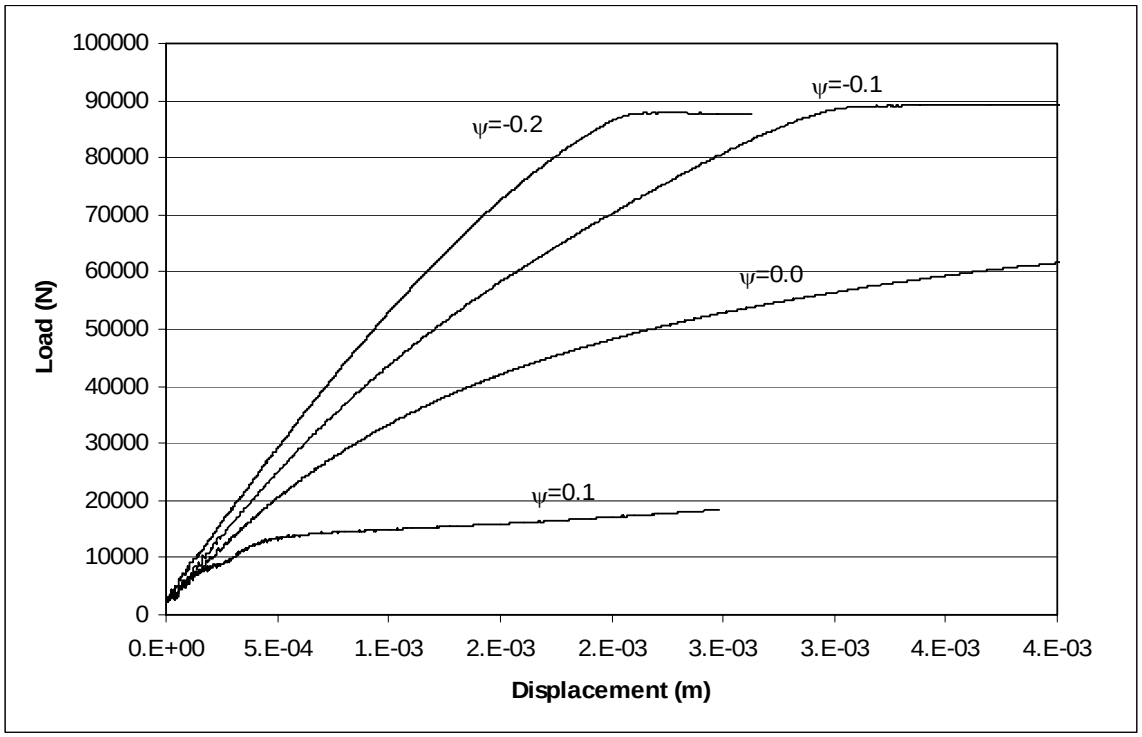

Figure 7.3: Side resistance of the pile against displacement under different sand states

The side resistance of the pile is determined by the normal stress on the interface between pile and sand and the critical state strength of sand. The critical state strength is frictional and depends only on the mineralogical and particle characteristics of the sand. It does not depend on the state of sand. However, the normal stress of the interface is dependent on the type of dilatancy when it is subjected to shearing. The dilative sand

with negative ψ values would expand under shearing but contractive sand with positive ψ values would contract. Since the pile is constrained from movement in the normal direction, volume changes in sand will be accommodated by variations of stress along the interface. Thus, the dilative behavior would result in an increase in normal stress whereas contractive behavior would result in a decrease in normal stress.

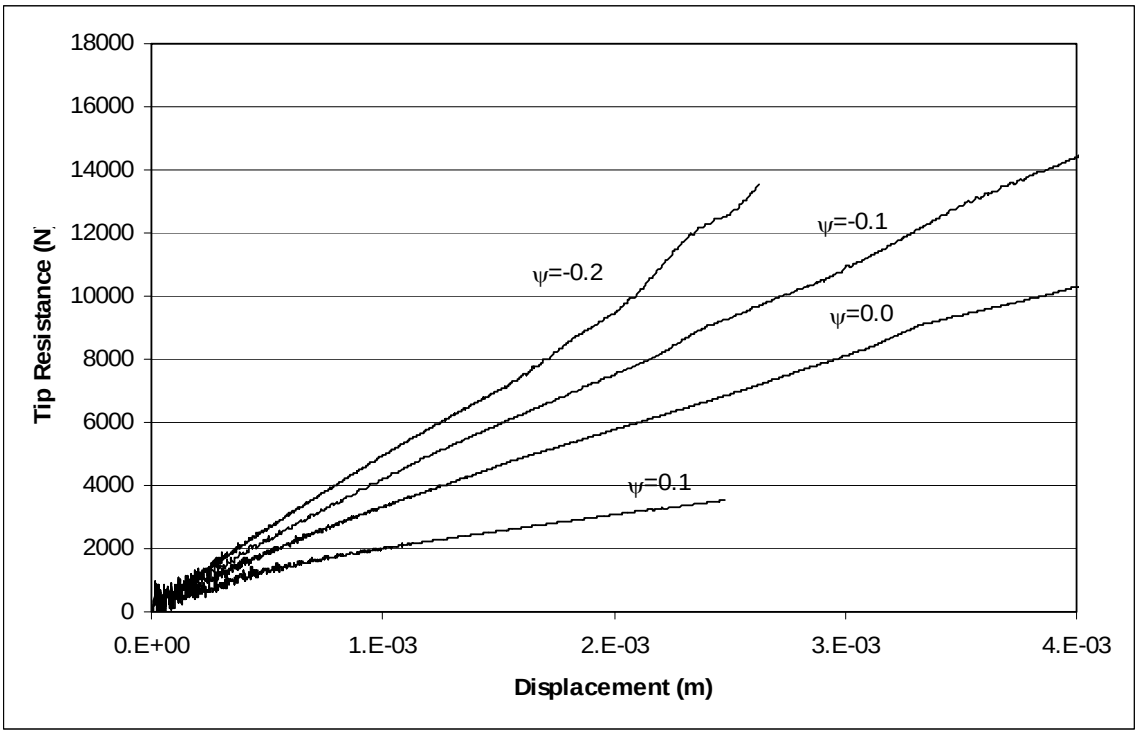

Figure 7.4: Tip resistance of the pile against displacement under different sand states

The typical variation of normal stress contribution is shown in Figure 7.5, where σ_{zi} is initial normal stress applied to the pile surface and $\Delta\sigma_z$ is the normal stress variation induced by sand expanding or contracting under shearing. For contractive sand, $\Delta\sigma_z$ would be negative and for dilative sand it will be positive. Based on the above discussion, it is evident that the side resistance will be related to the state parameter (Fig. 7.3).

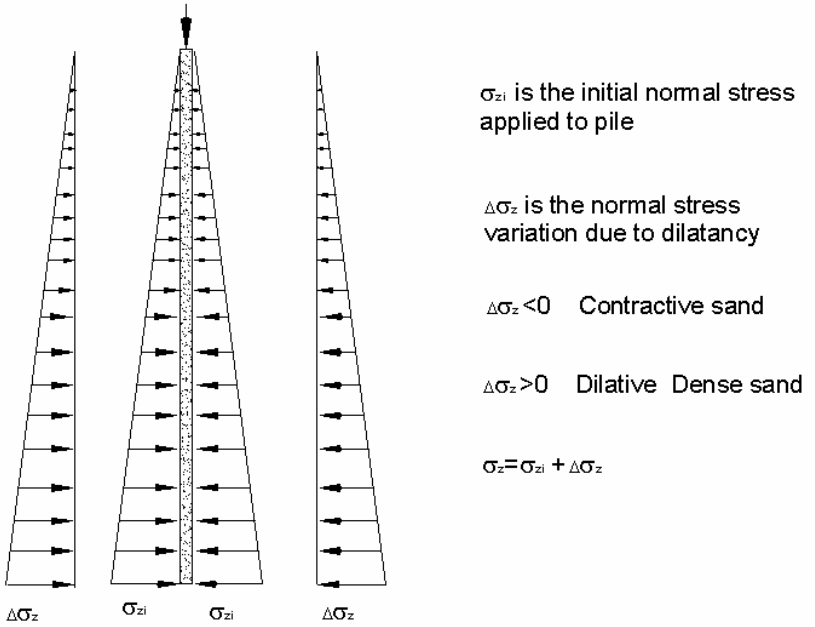

Figure 7.5 Normal stress contribution

The results show that the side resistances are completely mobilized when the pile penetration is between 0.5 mm and 3 mm, depending on the state of the sand. On the contrary, the sand deformation at the pile tip is elastic for all sand states except for the case ψ=0.1. Thus, that the tip resistance is not yet completely mobilized at this stage (Fig. 7.4). Juran et. al. (1999) gave a range of 20 to 40 times the ratio of displacement to fully mobilize the tip resistance over the displacement to fully mobilize the side resistance, but the value should change greatly with the value of *L/D* and soil properties.

Characteristics of both side resistance and tip resistance of the pile determine its total resistance. Both components increase from the contractive state to the dilative state. Therefore, the total resistance increases with a decrease in the state parameter, as shown in Fig. 7.6.

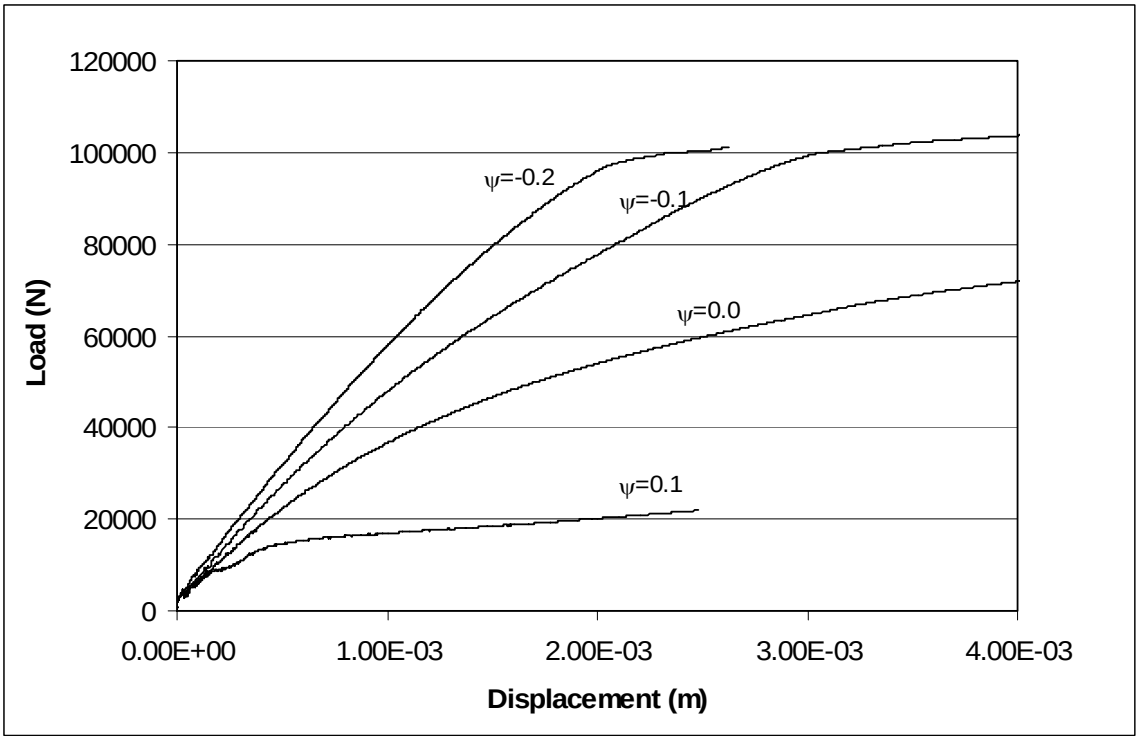

Figure 7.6: Total resistance of the pile against displacement under different sand states

7.2 Analysis of the Behavior of Groups of Piles

Several studies have been carried out in the past to investigate the behavior of a group of piles and micropiles in sand. However, as in the case of single piles, most of these studies were based on replicating the density of the sand and not the state. Thus, laboratory and full-scale experimental results reported by various investigators led to contradictory observations pertaining to the behavior of group and network micropile systems (Lizzi, 1978; Plumelle, 1984; Maleki, 1995). Therefore, FLAC3D analyses are extended here systematically to examine the effect of initial state on the behavior of groups of piles.

7.2.1 Group Pile Model Setup

The model dimensions and the sand are the same as in the case of a single pile. A 3-pile group with pile diameter of 200 mm and length 6 m were vertically installed in the center as shown in Figure 7.7. The normal and shear stiffness and strength of the interface between pile and sand are also set with values large enough to ensure that failure occurs in the surrounding sand.

The spacing of the piles is varied from 2*D* to 4*D*, where *D* is the pile diameter, to evaluate its effect on group behavior for a given state of sand. State parameters of 0.1, 0.0 and –0.1 were chosen to represent sands with contractive and dilative behavior. Small values of continuous vertical displacements were applied at the top nodes of the pile group to trigger side and tip resistances of micropiles from the surrounding sand. The side and tip resistance against displacement were recorded when the pile was pushed downward. The recorded curves are used to compare with those for a single pile.

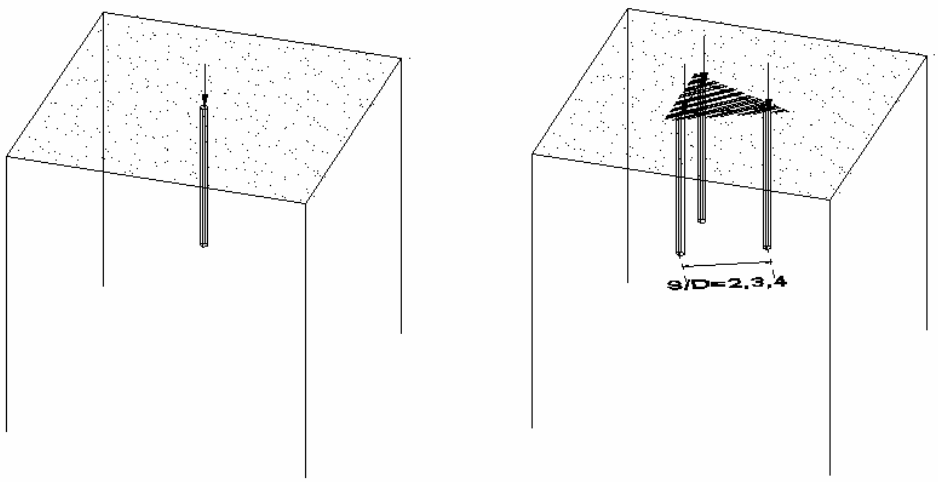

Figure 7.7 Setup for group effect

7.2.2 Results

The variations of side, tip, and total resistances of an individual pile in a group for initial state parameter -0.1, 0.0 and 0.1 are as shown in Figures 7-8, 7-9, and 7-10, respectively. There are several features associated with these variations as discussed below.

In all cases, the initial slope of the total and side resistance of the group piles, regardless of the spacing or state parameter, are lower than that of a single pile. The behavior changes with increase in displacement. All of the curves for side, tip and total resistance appear to reach an ultimate value that is higher or lower than that the single pile depending on spacing and initial state parameter. The variation of total resistance of group piles was not consistent. The ultimate total resistance was larger than 100 percent in most cases. However, the ultimate total resistance of group piles with spacing of 2D under ψ = 0.0 and 0.1 is observed to be lower than 100 % (Fig. 7.9(c) and 7.10(c)).

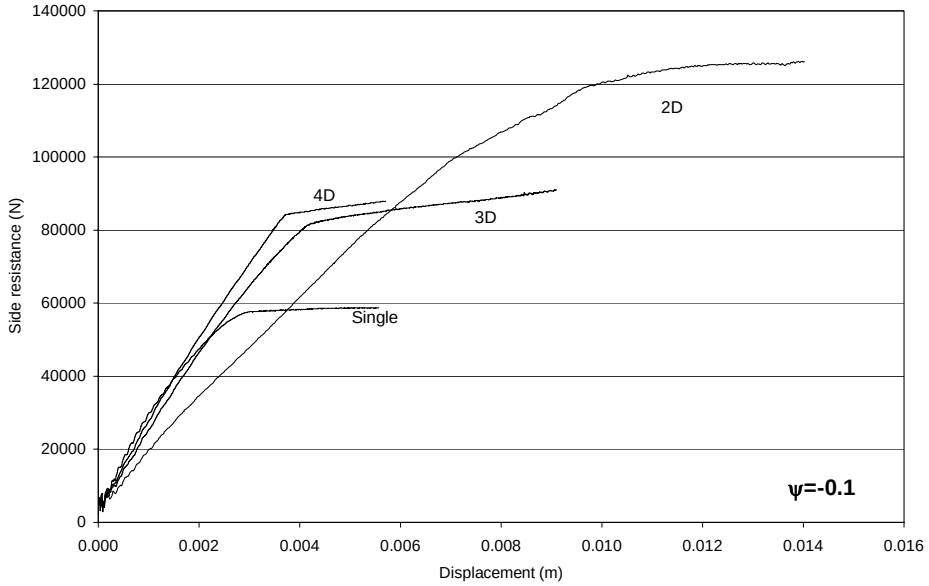

(a): Side resistance variation with Spacing

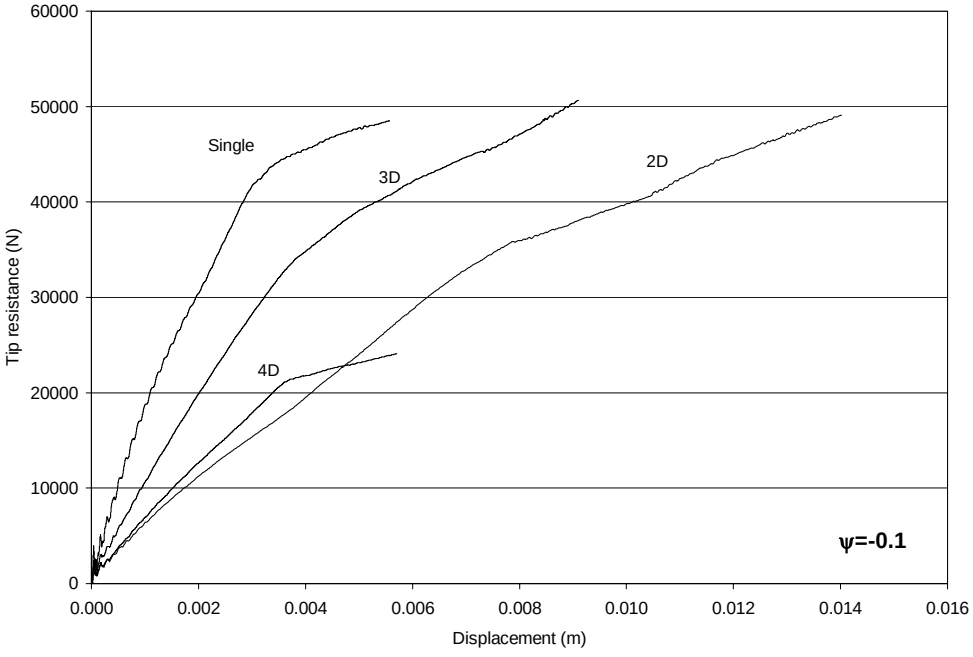

(b): Tip resistance variation with spacing

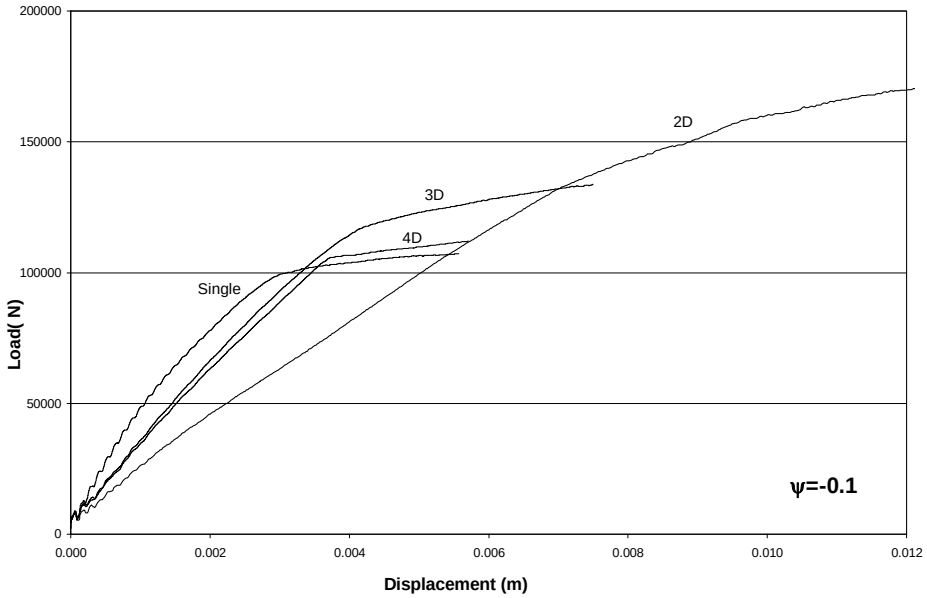

(c): Total resistance variation with spacing

Figure 7-8: Behavior of Group of Piles (ψ = -0.1)

Most past investigations on group effects on piles had only considered the total resistance in order to compare performance with a single pile and this led to similar inconsistencies. However, as shown later, a closer examination of the variations of side resistance and the tip resistance developed here enables us to put forward a concept that can better interpret the behavior of group piles.

The group effect of tip resistance in dilative sand is less than 100 percent or a negative contribution (Figure 7-8 (b)). However it is larger than 100% or a positive contribution for sands with ψ = 0.0 and ψ = 0.1 (Figures 7-9 (b) and 7-10 (b)).

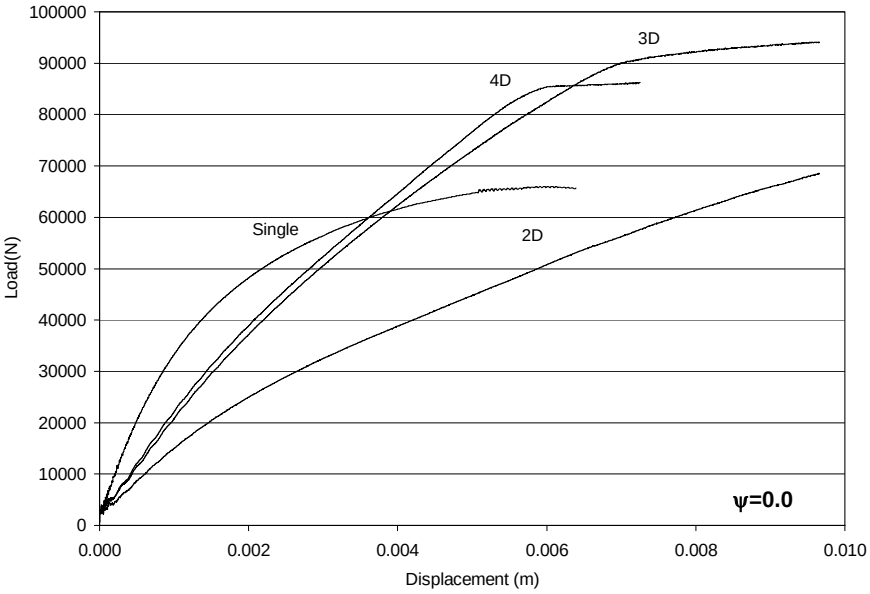

(a) Side resistance variation with spacing

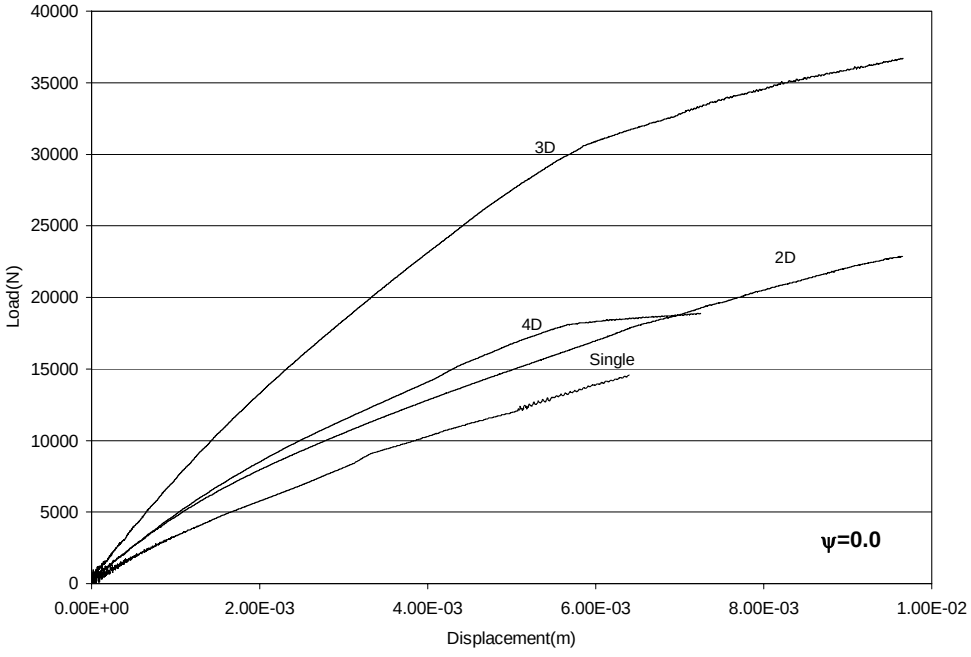

(b) Tip resistance variation with spacing

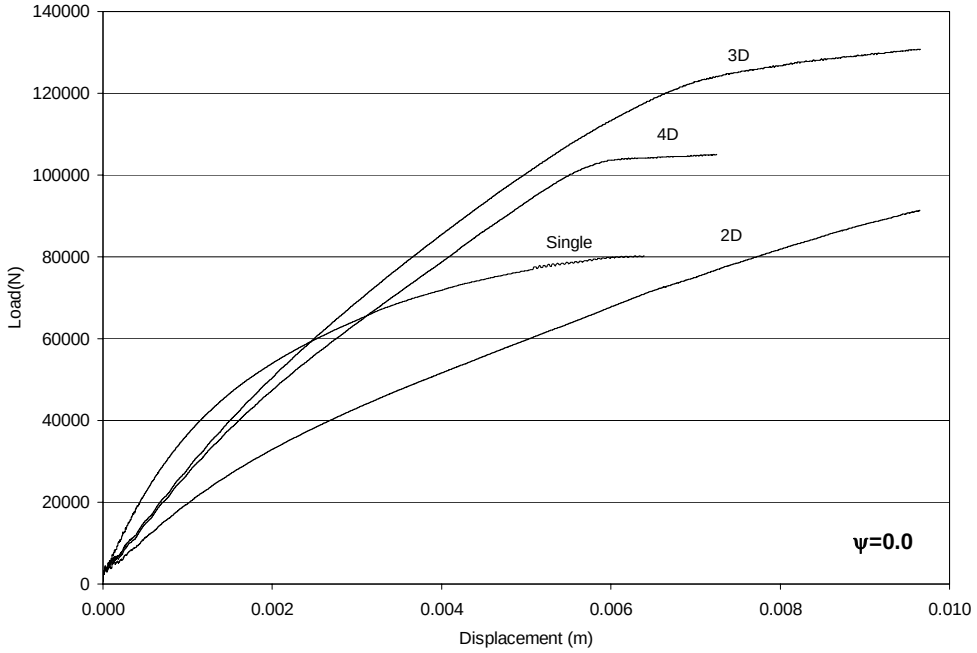

(c) Total resistance variation with spacing

Figure 7-9: Behavior of Group of Piles ($\psi = 0$)

The group effect of ultimate side resistance for dilative sand ($\psi = -0.1$) is larger than 100 percent resulting in a positive contribution. However, results are mixed for sands with $\psi = 0.0$ and $\psi = 0.1$ ((Figures 7-8 (a) 7-9 (a) and 7-10 (a))). While most groups had a positive contribution, piles with the closer spacing (2D) had a negative effect.

The total resistance or capacity of a pile under vertical loading is the sum of side and tip resistances. Thus, both components must be monitored in practice to understand the behavior of a group of piles. As mentioned before, most past studies did not do this except in a study conducted by Vesic (1969). Vesic reported the results of tests on model groups of four and nine piles. The tip resistance and the side resistance were measured separately. Vesic concluded that when the efficiency of closely spaced piles was greater

than unity, such increase was mainly registered in the shaft rather than in the tip resistance. These results were not theoretically supported nor verified by other subsequent researchers.

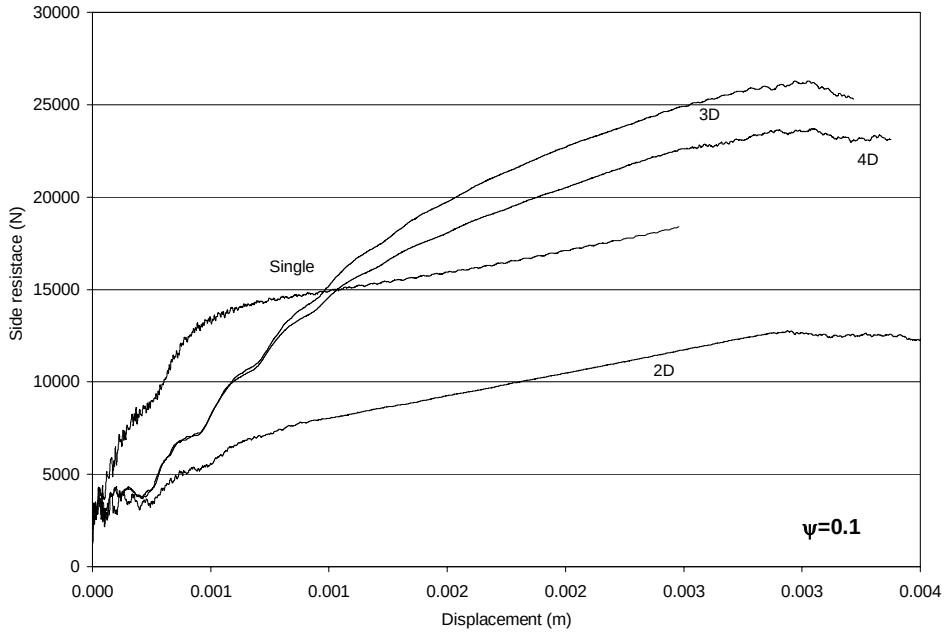

(a) Side resistance variation with spacing

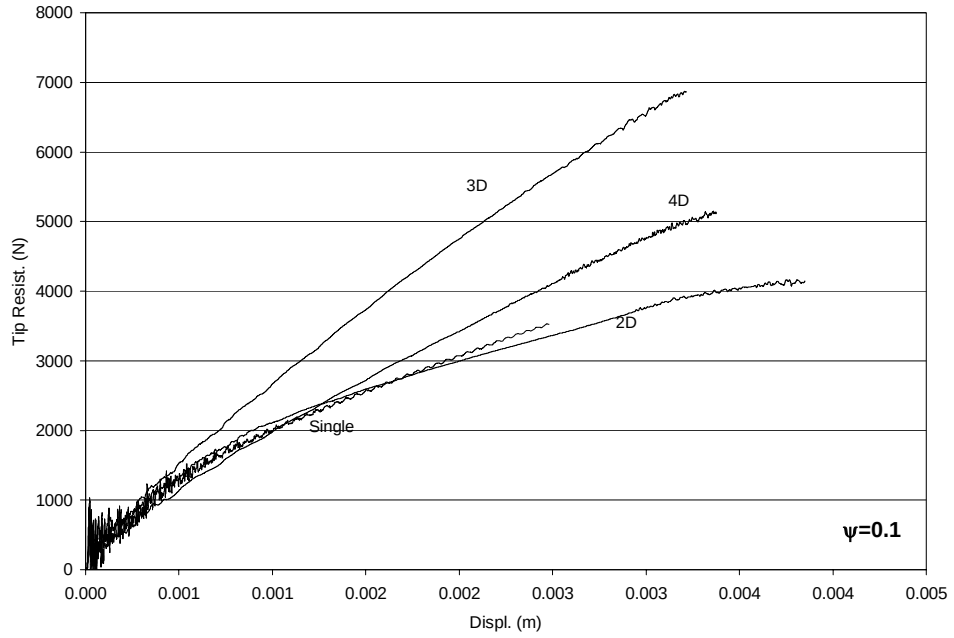

(b) Tip resistance variation with spacing

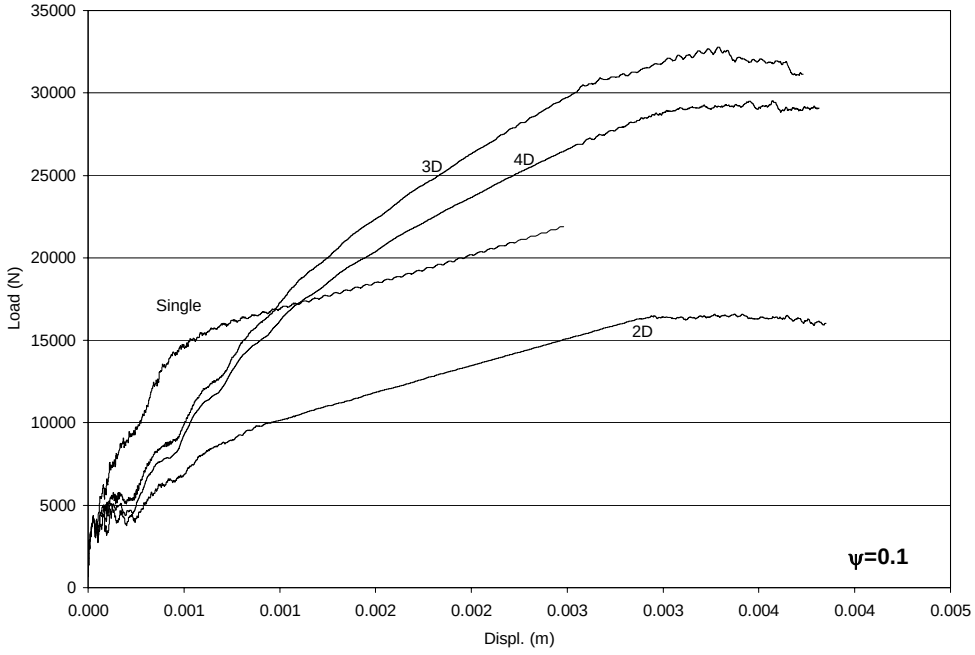

(c) Total resistance variation with spacing

Figure 7-10: Behavior of Group of Piles ($\psi = 0.1$)

7.2.3 Proposed mechanism of group pile behavior

It is proposed that the group effect of pile resistance is controlled by two mechanisms: one due to volume changes or dilatancy and the other due to an overlap of shear stresses from the presence of adjacent piles. The effect of dilatancy on group behavior is different for driven piles and bored piles. In driven or displacement piles, the installation process results first in the displacement of the surrounding sand in the normal direction followed by shearing as shown in Figure 7-11. Thus, the initial displacement would cause the dilative sand to loosen, thereby reducing its potential for dilatancy. On the contrary, displacement will densify contractive sand thus reducing its potential for further reduction in volume. The process of displacement can be represented in the state diagram, as shown in Fig. 7.12. Thus, in displacement type group piles, irrespective of the initial state, subsequent shearing will not change its state or volume changes very much.

Most bored piles are installed with little displacement in the normal direction (Figure 7-11). The boundary conditions imposed on the piles here resemble the case of bored piles. Thus, very little change will occur to its initial state during installation. The dilative or contractive nature of the initial state will in turn influence the development the side resistance as discussed in the case of a single pile. However, in the case of closely spaced group piles, geometric limitations will alter the effect of dilatancy from the case of a single isolated pile. In the case of contractive sands, group effects will result in the reduction of the normal stress and hence in the side resistance as compared to an isolated pile case. The opposite will be true in the case of dilative sands. The numerical results imply these observations as seen from Figures 7-8 (a). 7-9 (a) and 7-10

(a)), and the interpretation will be given subsequently, combined with a stress overlapping mechanism.

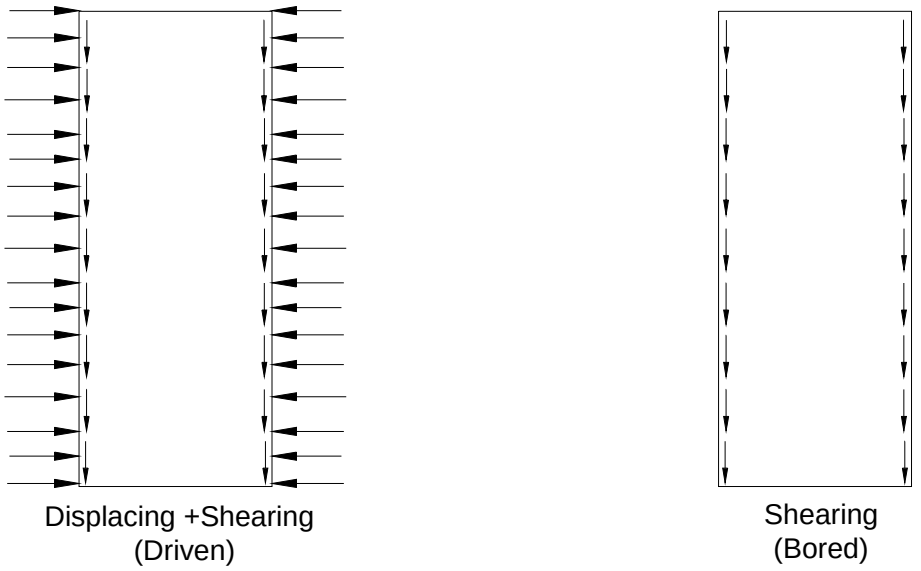

Figure 7-11 Schematic of driven and bored pile installation

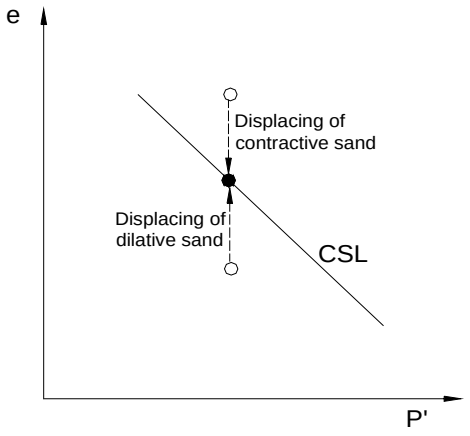

Figure 7-12 State variation of surrounding sand due to pile driving

The second mechanism of side resistance in group piles results from an overlap of shear stresses. The pile load induced shear stresses are shown in Figure 7-13. The variation of the shear stress with radial distance on a single pile is as shown in Fig. 7-14.

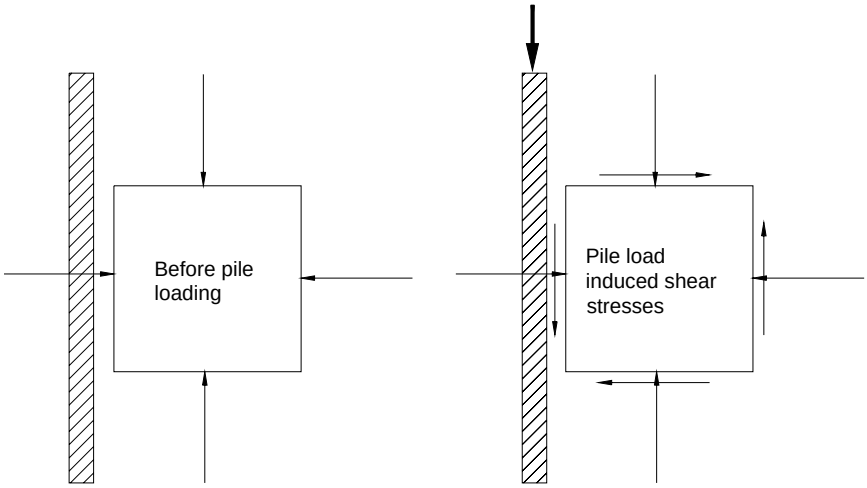

Figure 7-13 Schematic of pile load induced shear stresses

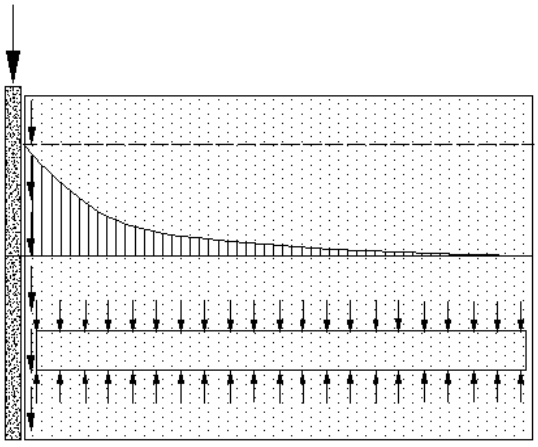

Figure 7-14 Schematic of shear stress distribution in sand for isolated pile

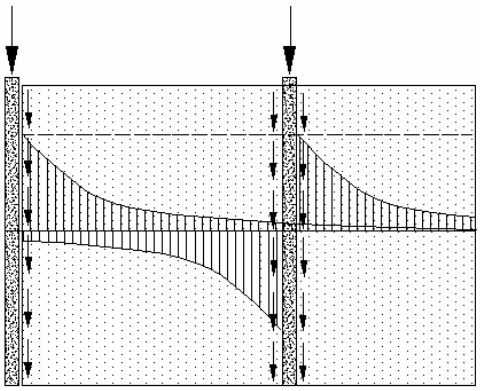

(a) Schematic of shear stress components induced by two piles (left side not shown)

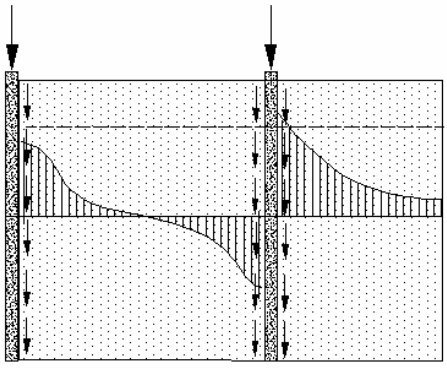

(b) Superposition of shear stress components induced by two piles

Figure 7-15: Overlap of shear stress in surrounding sand for pile group

It is seen that the shear stress decreases with distance to near zero values. The variation of individual shear stress with distance for two closely spaced piles is as shown in Figure 7-15 (a). Superposition of the individual shear stresses will result in the shear stress variation as shown in Fig. 7-15(b).

It can be seen that while the overlap of shear stresses from the two piles balance each other in the segment in between, they increase the shear stresses on the outside of the two piles. Thus, the overlap of shear stresses might contribute to positive increase in side resistance in group piles regardless of the state.

To verify the above overlap mechanism of shear stress contribution, group analyses were carried out on piles installed in an elastic sand (dilatancy effects were zeroed). The variations of side resistance with pile spacing are as shown in Figure 7-16.

It is evident that group piles reach a higher ultimate resistance than a single pile. Since there is no dilatancy involved, the increase must have come from overlap of stresses. It is also of interest to note that piles with the closest spacing (2D) reached the highest value whereas the ones with 3D and 4D reached only a moderate increase. This means that the overlap stress effect decays with an increase of pile spacing.

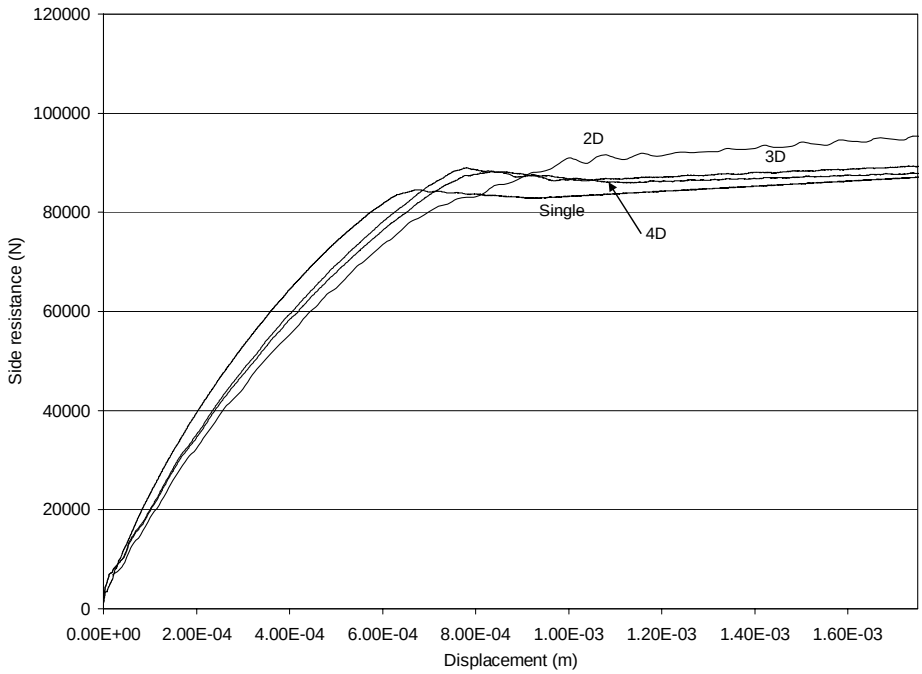

Figure 7-16 Side resistance due to overlap of stresses

The discussion supported by the above analyses shows that overall side resistance in group piles is dependent on both dilatancy (volume change) and stress overlap mechanisms. In the case of dilative sands, both mechanisms produce a positive effect resulting in increased overall side resistance as seen in Figure 7-8 (a). However, in the case of contractive sands, increase or decrease in the overall side resistance in group piles would depend on the dominant mechanism. It is believed that the volume change mechanism (contractive) is dominant in Figure 7-10 (a) resulting in a negative contribution for the closely spaced pile spacing of 2D. However, the mechanism of stress overlap dominates pile spacings of 3D and 4D, leading to positive side resistance effect.

The variation of the tip resistance of group piles in an elastic medium is as shown in Figure 7-17. It can be seen that when contributions from overlap of stresses are only considered, the tip resistance in group piles is positive for pile spacing of 3D and 4D but negative for pile spacing of 2D.

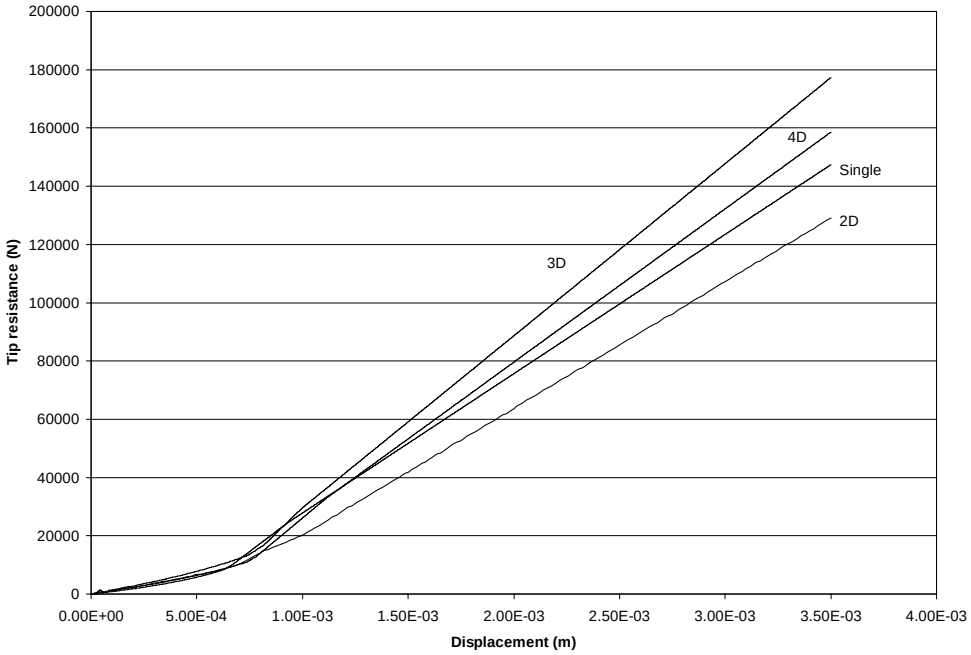

Figure 7-17 Tip resistance due to overlap of stresses

The dominance of the mechanism of volume change or overlap of stresses would also affect the overall variation of the tip resistance in group piles. When piles are pushed into dilative sands the increase in volume changes might result in a reduction in tip resistance. The effect will be opposite in the case of contractive sands.

In the case of the tip resistance variation in dilative sand, as in Figure 7-8 (b), both mechanisms combine and contribute to the reduction of the tip resistance. Figures 7-9 (b) and 7-10 (b) show that group effects of tip resistance for piles in contractive sand are larger than 100 percent or close to 100 percent, however, if considering that the group effect contributed to by the stress overlapping mechanism is negative for pile spacing of 2D, it is believed that the group effect contributed by the dilatancy mechanism are all positive for the piles in contractive sand.

7-3. Analysis of Inclined and Network Piles

A micropile network consists of a group of inward and outward inclined piles. As discussed previously, the model studies of Lizzi showed a substantial increase in the capacity of piles (220%) when arranged as a network. Plumelle (1984) investigated the effects of inclination on the performance of driven micropile groups and found that inclination of the micropile led to a network effect that significantly increased the ultimate axial loading capacity and decreased the movement of the micropile group. On the contrary, full scale tests conducted by the FOREVER program on Lizzi's network arrangement showed only moderate increase in capacity.

As in the case of vertical group piles, most previous full scale and model tests on the network effect of micropiles, except those that used centrifuge tests, did not account for the state of sand correctly. Model tests were performed on sands with replication of density alone. As discussed before, such replication is not sufficient to replicate the state of sand. This led to the contradictory observations. Thus, numerical analyses were extended here to study the performance of network groups of piles. Both inward and outward inclined piles are considered.

7.3.1 Network Model Setup

Figure 7-18 shows an inclined pile and a network of a 3-pile group. Note that when the inclination angle $\alpha = 0°$, the network is identical to the vertical group. $\alpha > 0°$ constitutes outward inclined piles and $\alpha < 0°$ consists of inward inclined piles. The latter is referred to as a "basket" group of micropiles following Lizzi (1985).

The individual piles were of the same dimension as in the previous analyses. The piles were placed at a constant spacing of 400 mm on center (2 diameters) at the top.

Note that network micropiles are often categorized in practice as reinforcement type (Case 2 in Chapter 2). However, in order to maintain consistency with the previous investigation of vertical group, freestanding micropiles (Case 1) was chosen here.

Very small values of continuous vertical velocity (less than 10^{-5} m/s), as the cases of single pile and pile group, were applied to the top nodes of the pile network to trigger the side and tip resistances of micropiles from the surrounding soil. The side and tip resistances against displacement were recorded when the pile was pushed downward.

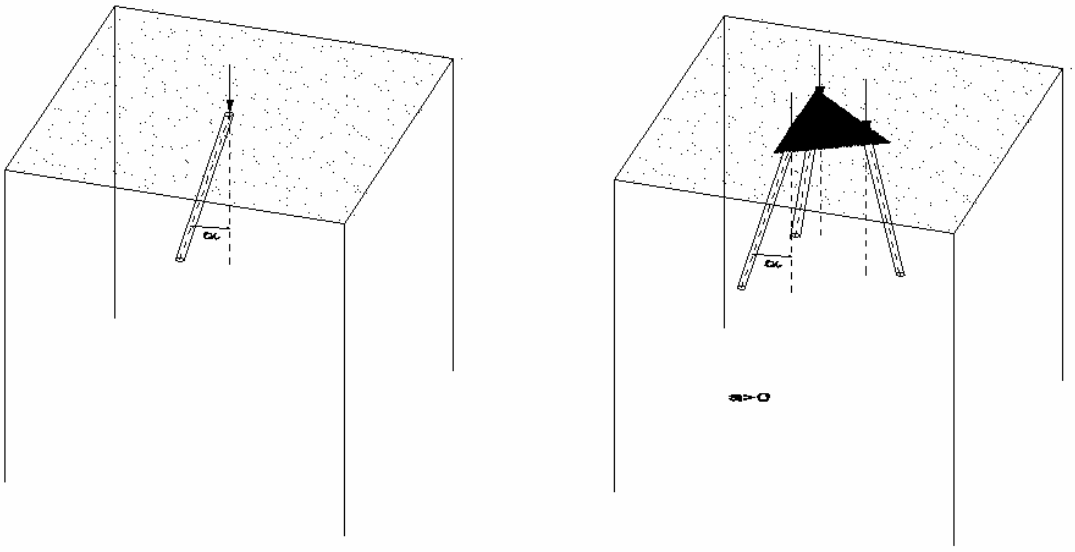

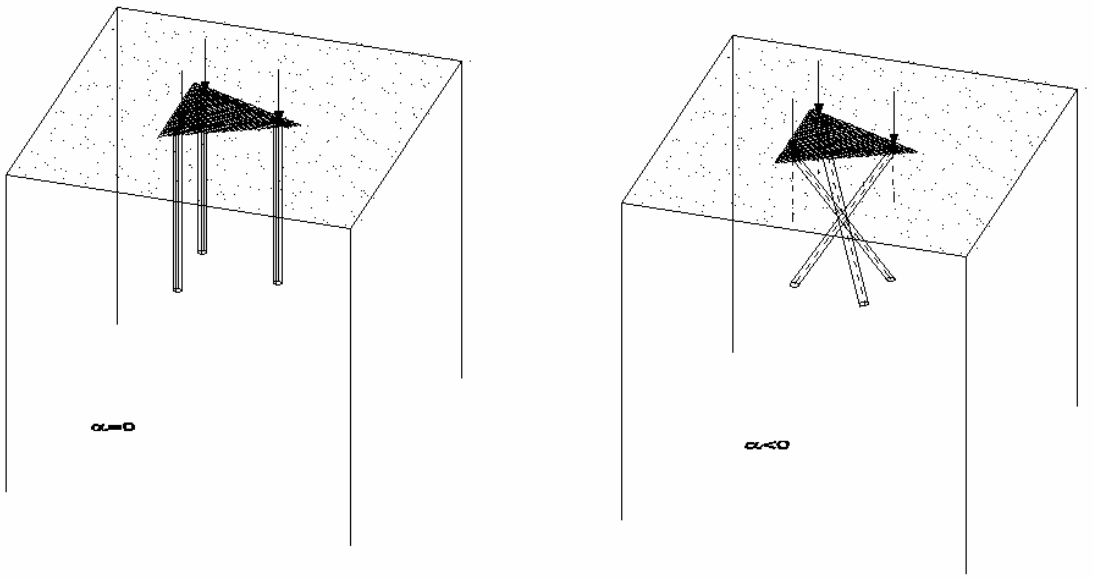

Figure 7-18 Model setup for network group

7.3.2 Performance of Inclined Pile

The first set of analyses was conducted on a single inclined pile. The chosen micropile inclination angles were 0°, 5°, 10°, and 15° and sand state parameters were 0.1, 0.0, and –0.1, corresponding to contractive, critical state, and dilative sands, respectively.

The variations of the side, tip, and total resistance with displacement of an inclined pile are as shown in Figures 7-19 to 7-21. It can be seen that the ultimate total resistance of an individual pile generally increases with increase in inclination angle for both dilative sand (ψ = -0.1) and contractive sand (ψ=-0.1) (Figure 7-19 (c), 7-20 (c) and 7-21 (c)). Exception to this behavior occurs for the pile with inclination angles of 5^0 and 10^0 in critical state sand (ψ = 0.0) where the total resistance of the former is found to be larger than that of the latter.

The ultimate side resistance of an inclined micropile in dilative sand is less than that of a vertical micropile (Figure 7-19 (a)). It is also evident that the ultimate side

resistance of inclined pile does not change much with inclination angle. On the contrary, the ultimate side resistance of an inclined micropile in contractive sand is larger than that of a vertical micropile (Figure 7-21 (a)). In addition, the ultimate side resistance is found to increase with pile inclination angle. The ultimate side resistance of a pile in the critical state sand also increases with inclination angle but with an exception for inclination angles of 5^0 and 10^0.

Tip resistance variation with pile inclination angles are as shown in Figures 7-19 (b), 7-20 (b), 7-21 (b). The ultimate tip resistance increases with pile inclination angle for all sands. Exception to this behavior, as observed previously in total and side resistances, is for piles in critical state sand with inclination angles of 5^0 and 10^0.

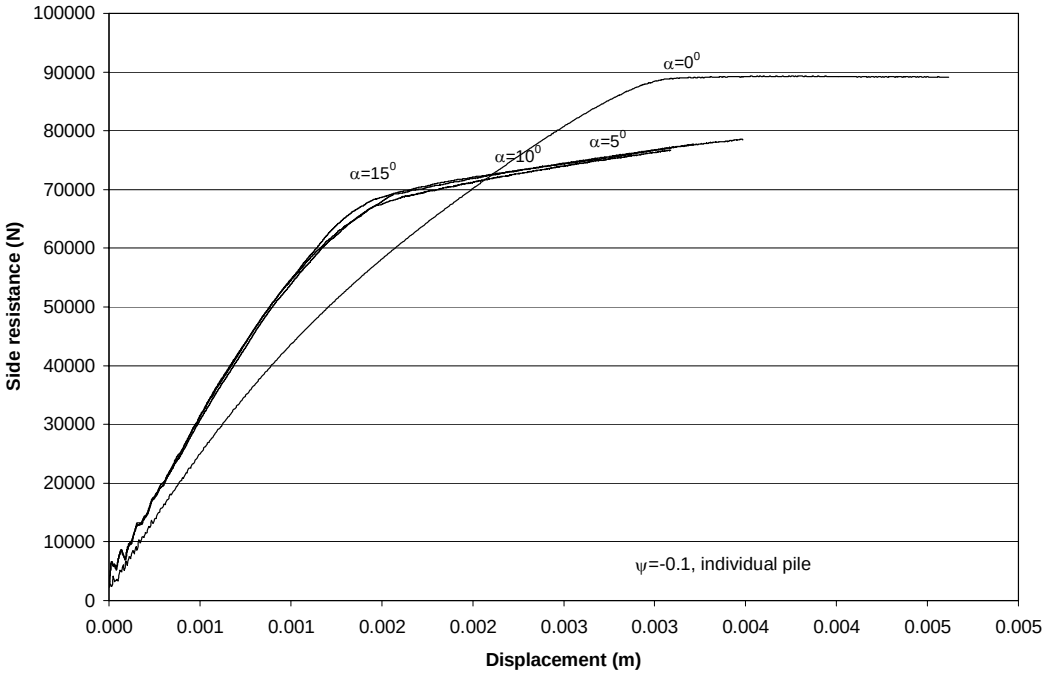

a) Side resistance variation with pile inclination

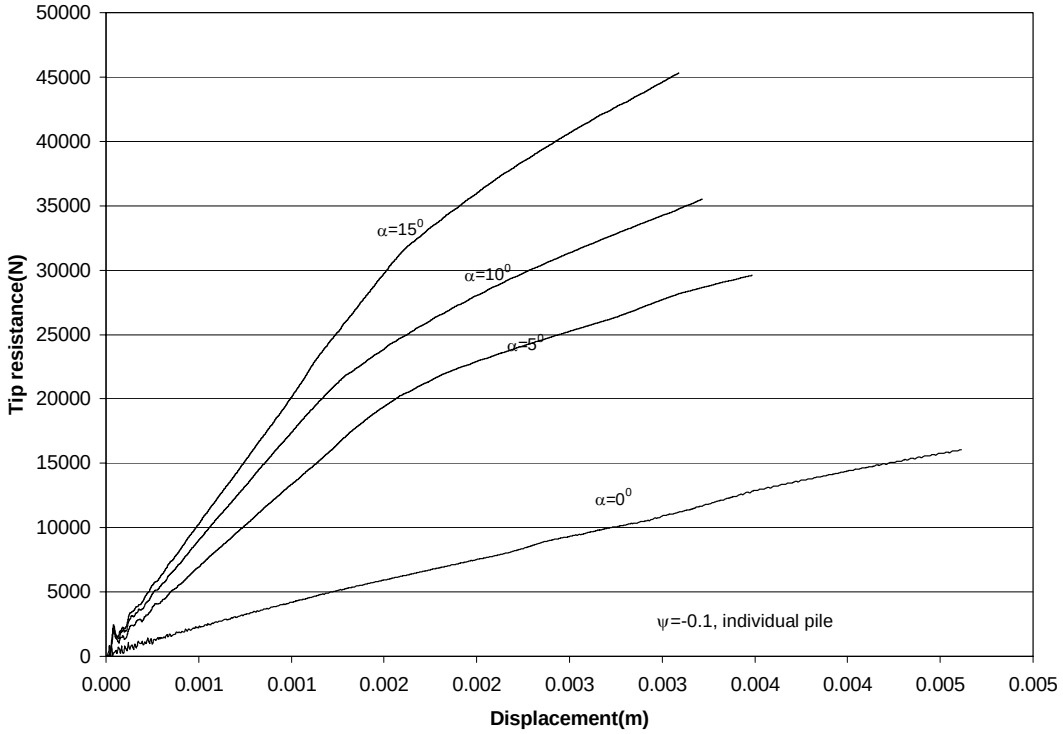

b) Tip resistance variation with pile inclination

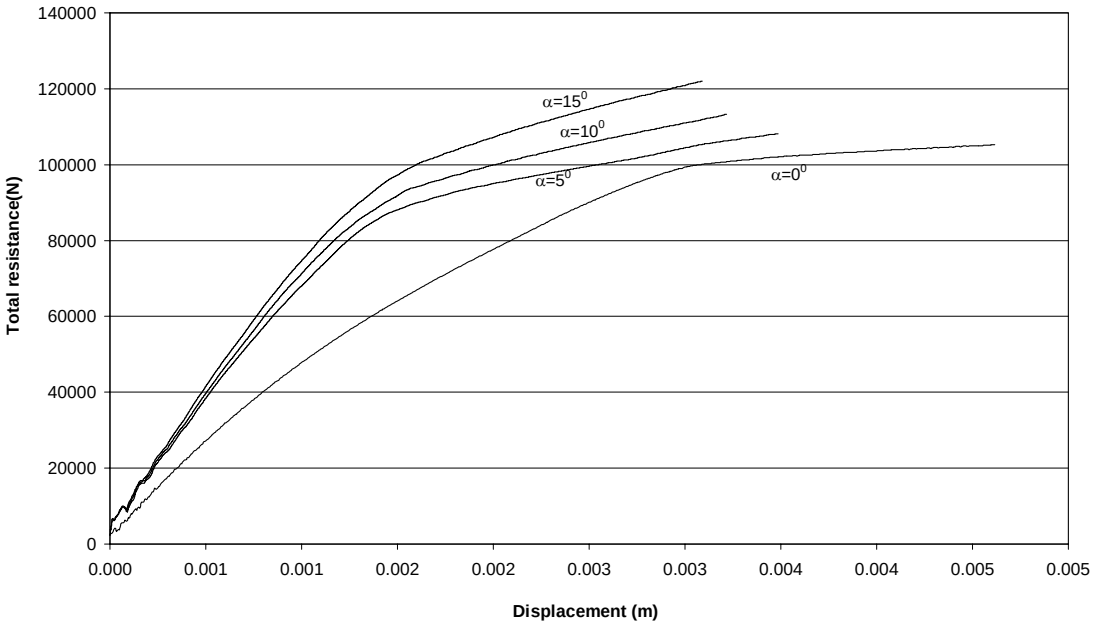

c) Total resistance variation with pile inclination

Figure 7-19 Inclination effect of an individual pile for ψ=-0.1

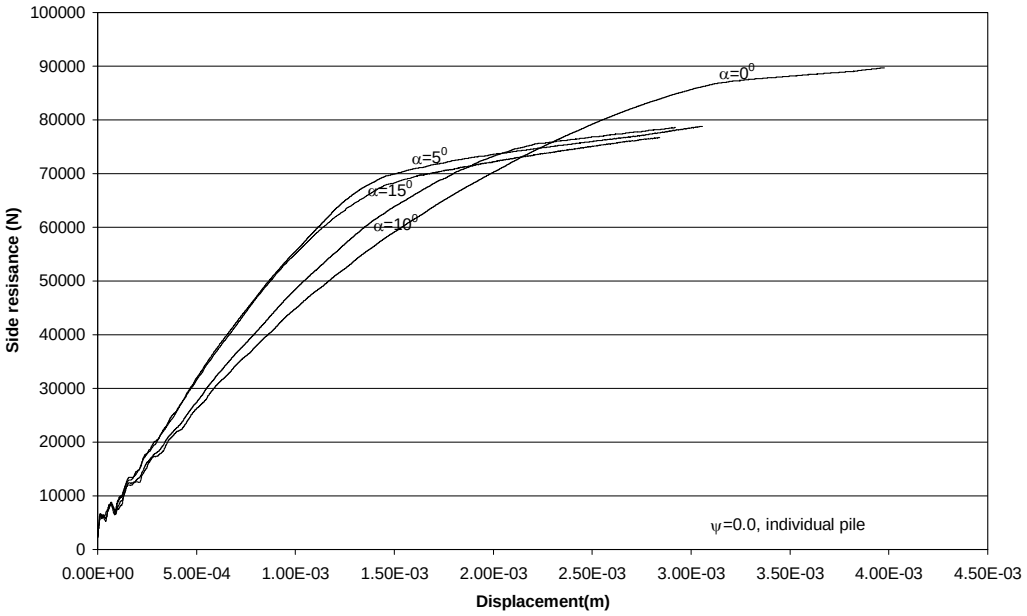

a) Side resistance variation with pile inclination

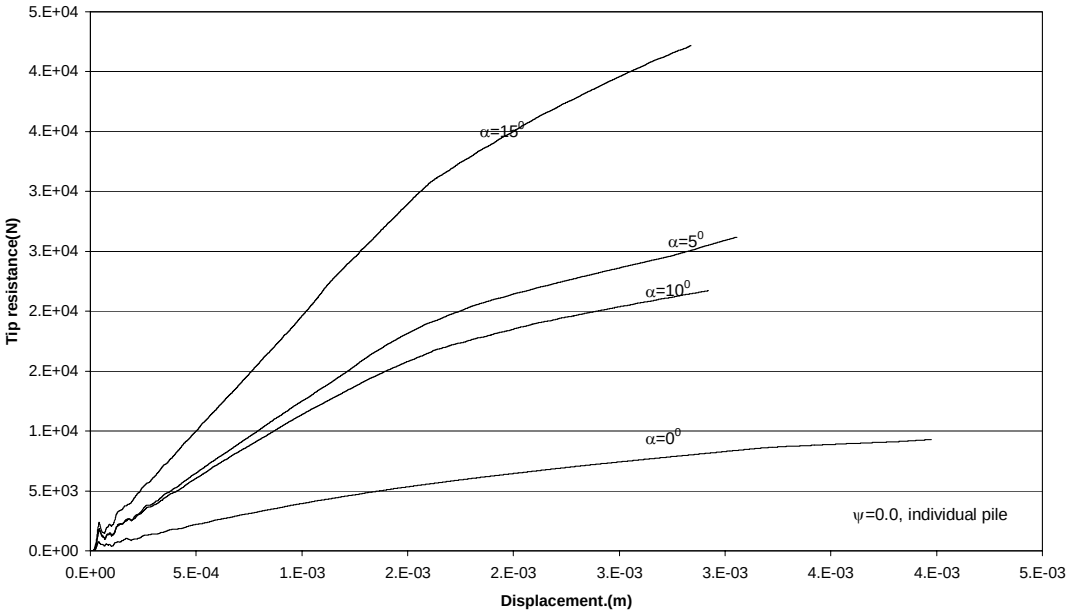

b) Tip resistance variation with pile inclination

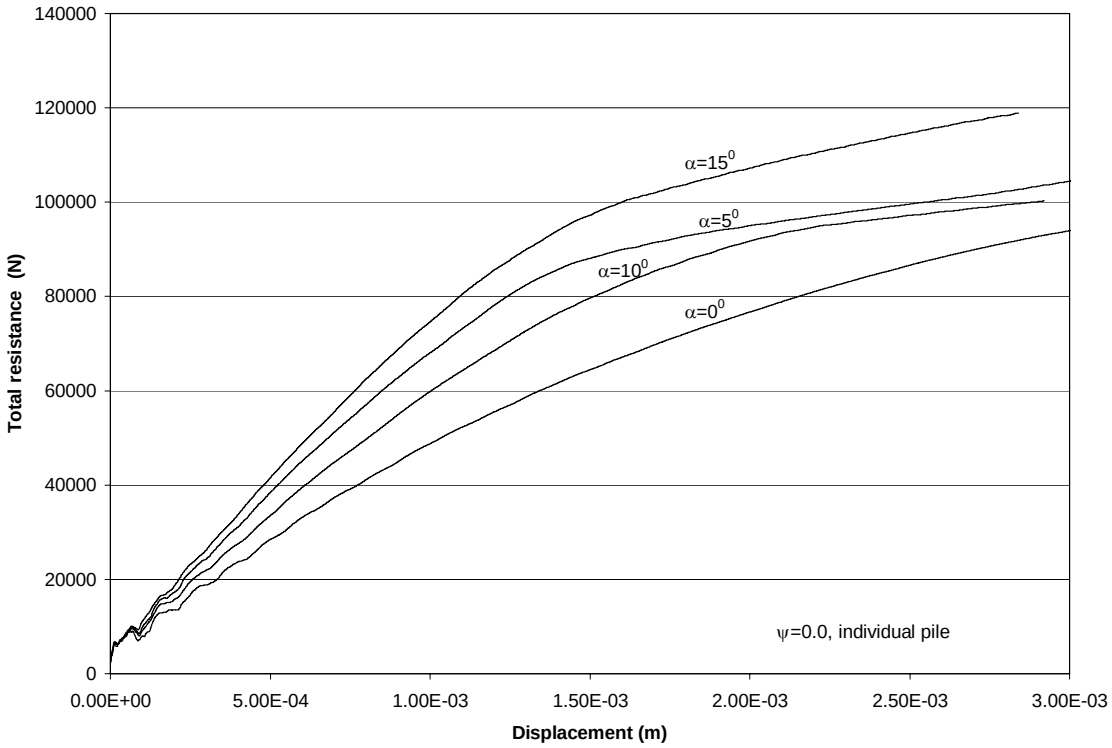

c) Total resistance variation with pile inclination

Figure 7-20 Inclination effect of an individual pile for ψ=0.0

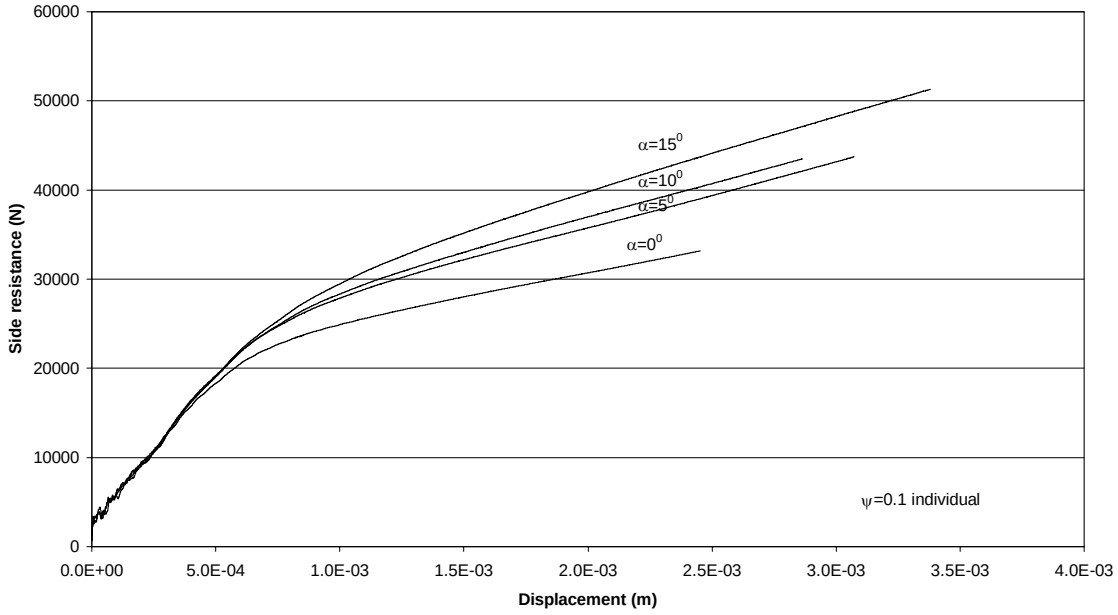

a) Side resistance variation with pile inclination

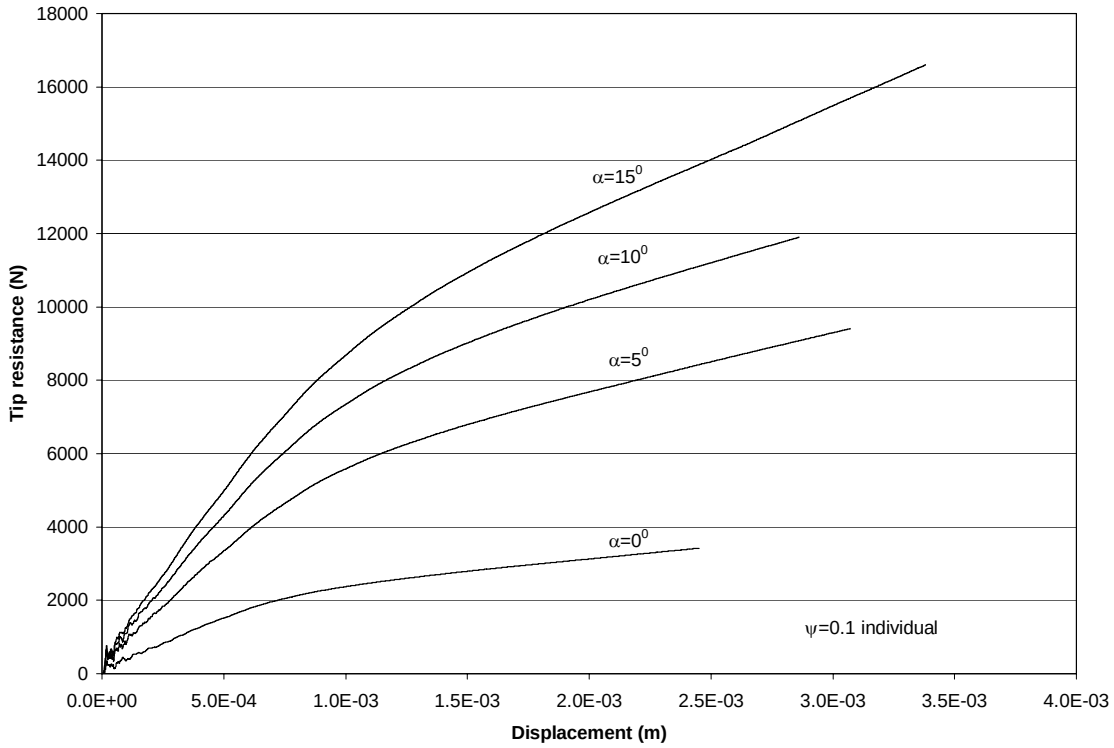

b) Tip resistance variation with pile inclination

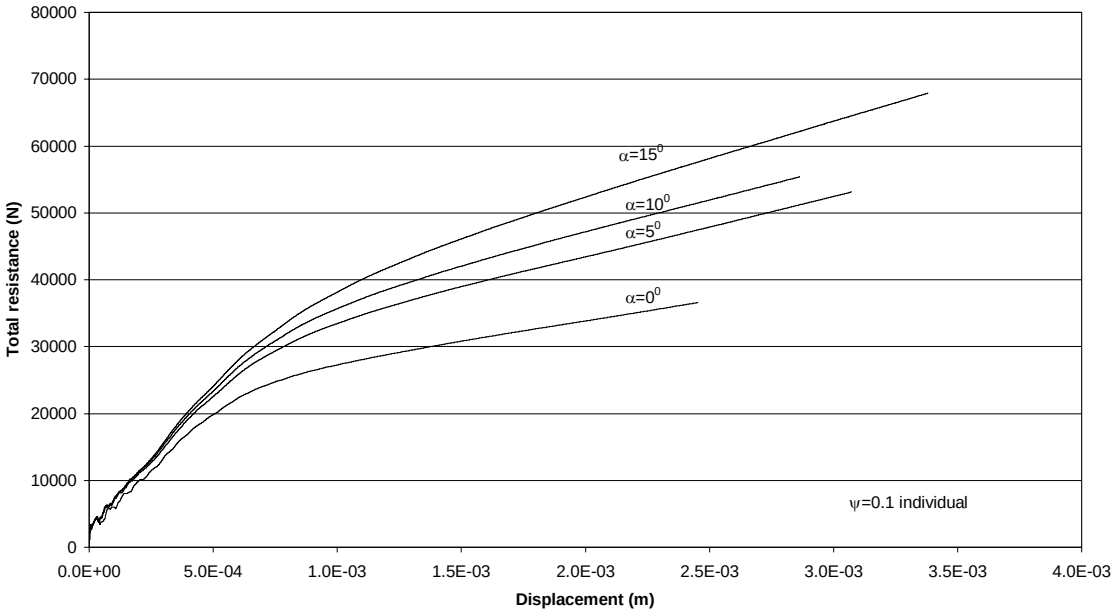

c) Total resistance variation with pile inclination

Figure 7-21 Inclination effect of an individual pile for ψ=0.1

7.3.3 Performance of Outward network Piles

Figures 7-22 to 7-24 show the variation of the side, tip and total resistance of outward inclined micropile group with inclination angle.

It is seen that for dilative sand the side resistance is a maximum in the case of a vertical pile. It decreases slightly with inclination angles from 5^0 to 15^0 (Fig. 7-20 a). However, for the same sand, all of the total resistance curves for inclined network piles plot above the vertical micropile group (α=0°). Moreover, the ultimate resistances of the piles reach a higher value with increased angle of inclination up to 10°. Further increase in angle of inclination, however, appears to result in a lower value for the ultimate total resistance as seen in the case for α = 15°. Note that this was not the case for a single pile where the total resistance increased with inclination for all cases. The variation of the tip resistance is similar to that of the total resistance with its maximum attained for an inclination angle of 10^0.

The variation of side resistance of piles installed in critical state sand with inclination is different from that in dilative sand in that it reaches a maximum at an inclination angle of 10^0(Figure 7-23 (a)). However, the total and tip resistance of piles installed in this sand show the same behavior as found in dilative sand (Figures 7-23 (b) and (c)).

In the case of piles installed in contractive sand, total, side and tip resistances increased with pile inclination angle (Figures 7-24 (a), (b) and (c)).

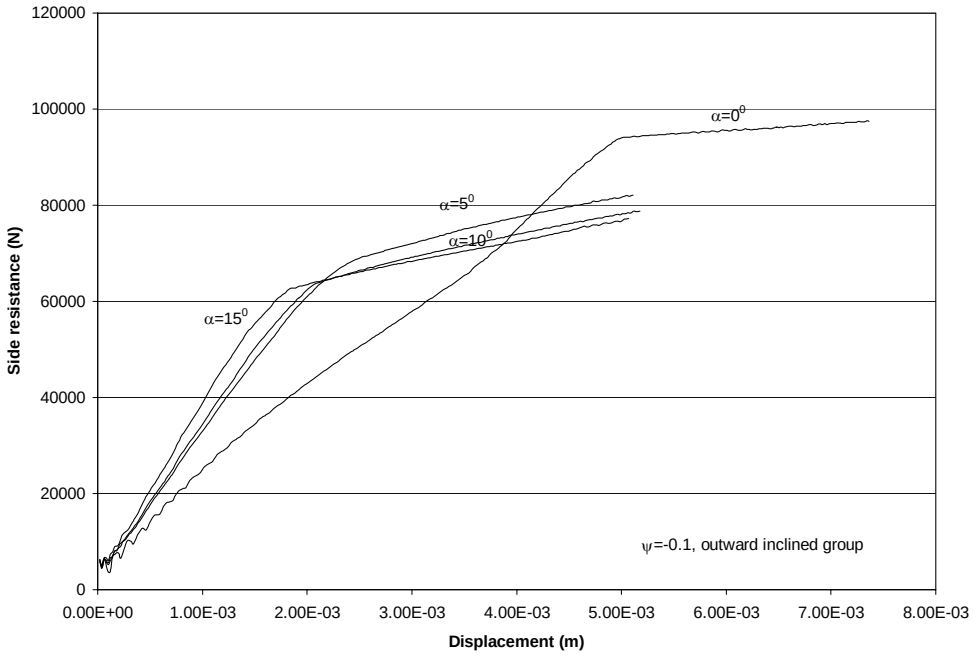

a) Side resistance variation with pile inclination

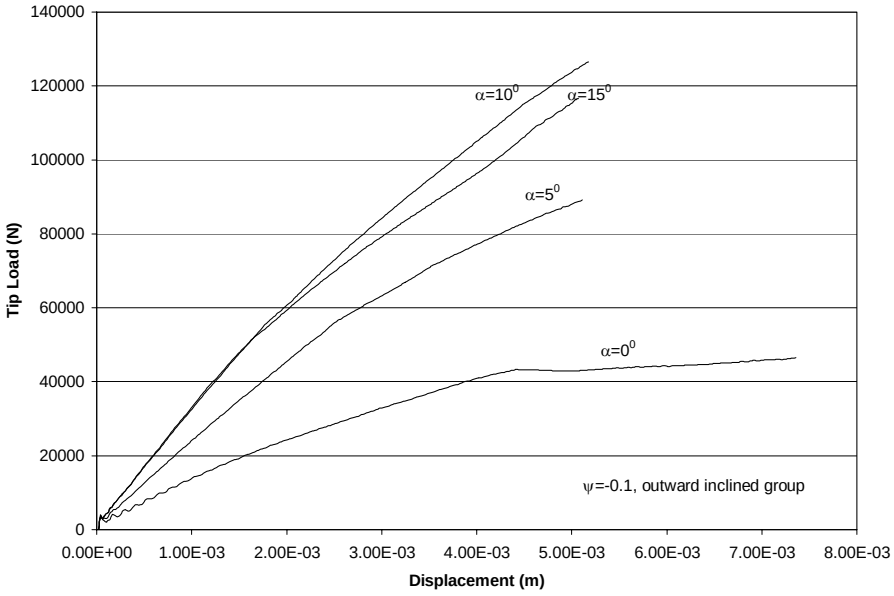

b) Tip resistance variation with pile inclination

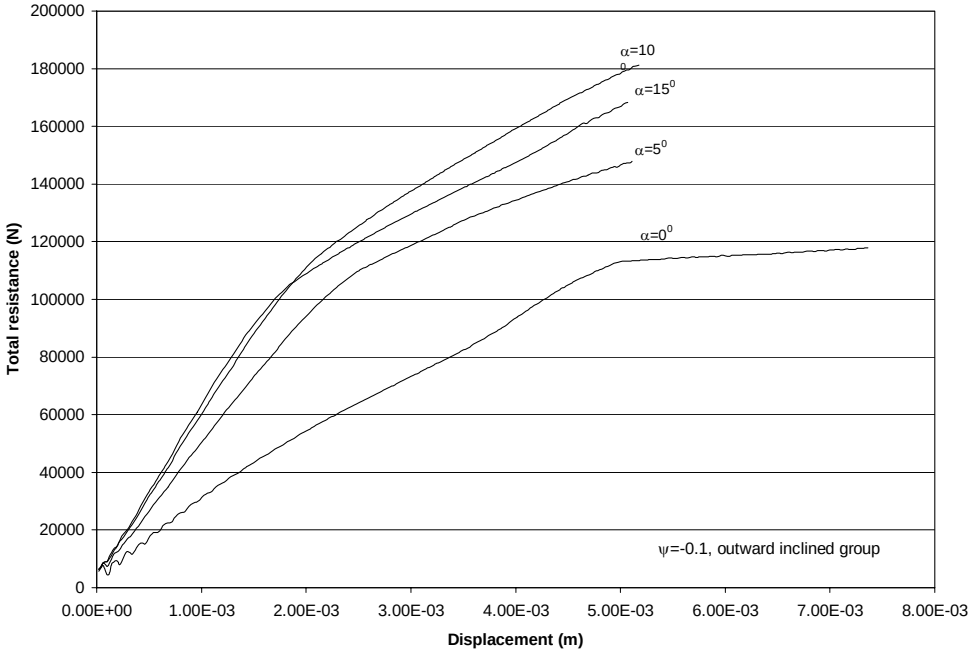

c) Total resistance variation with pile inclination

Figure 7-22 Inclination effect of outward inclined pile group for ψ=-0.1

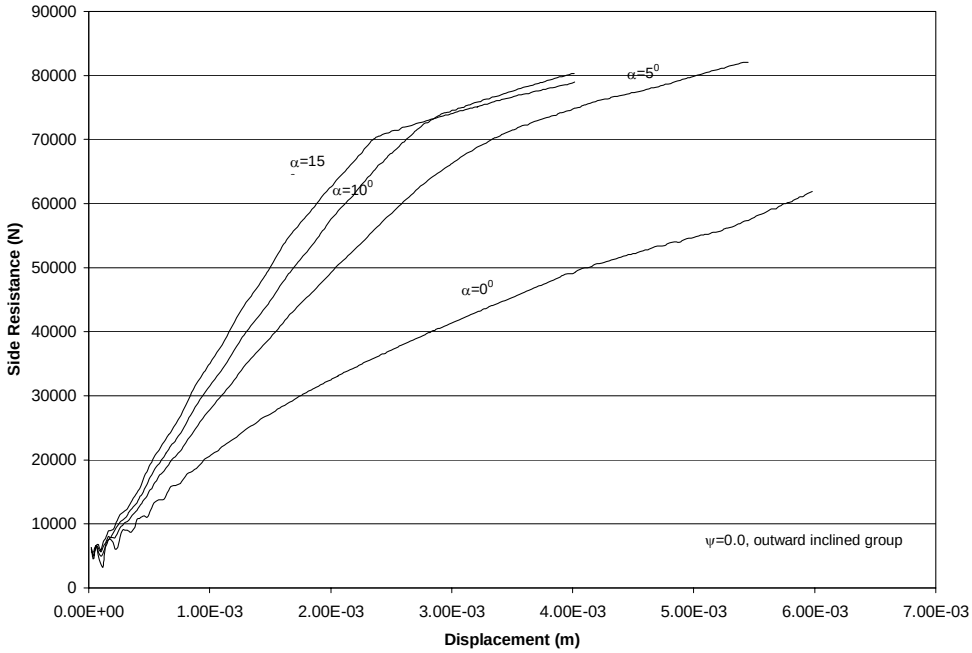

a) Side resistance variation with pile inclination

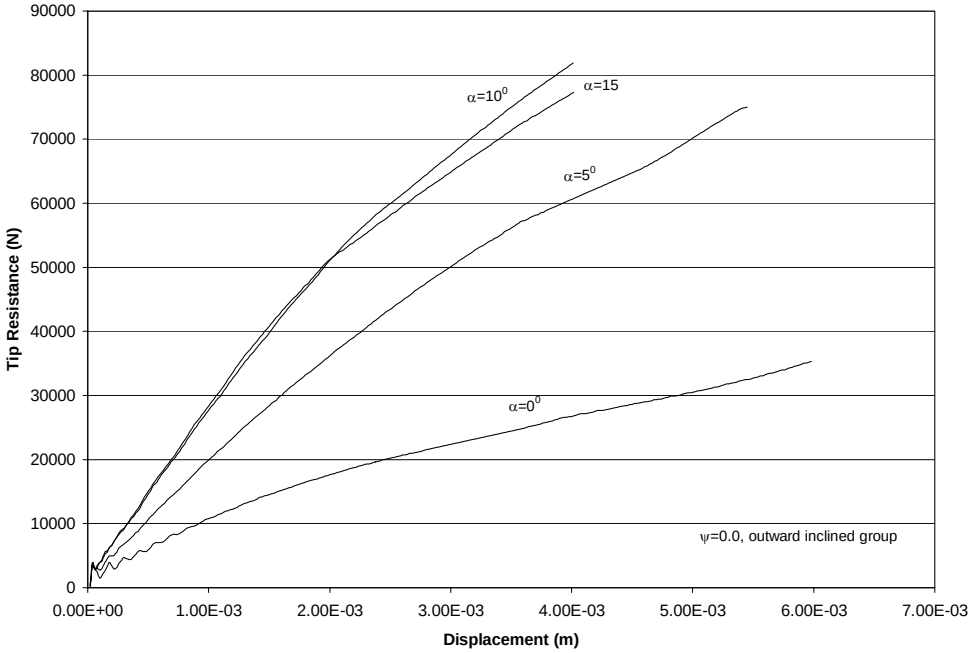

b) Tip resistance variation with pile inclination

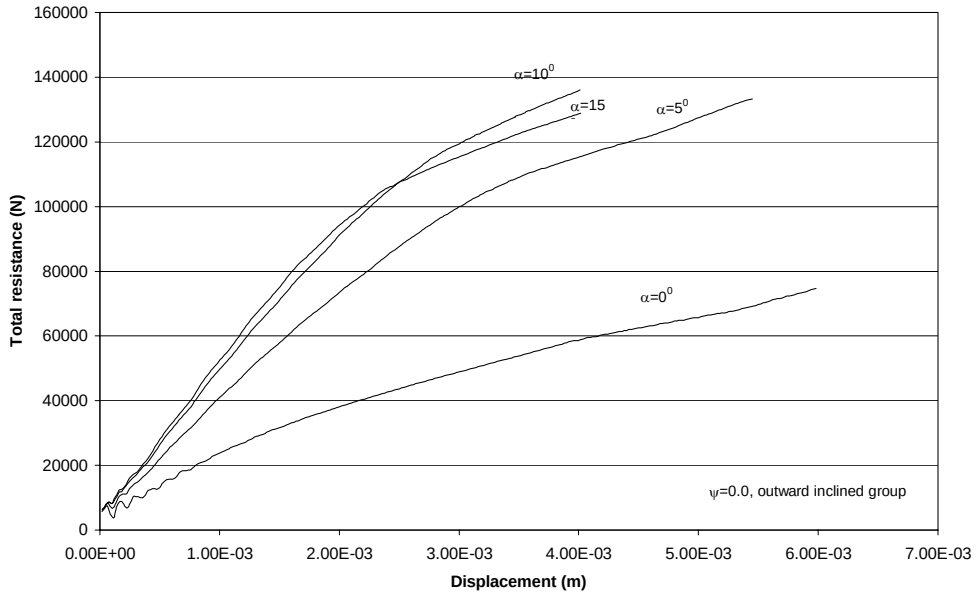

c) Total resistance variation with pile inclination

Figure 7-23 Inclination effect of outward inclined pile group for ψ=0.0

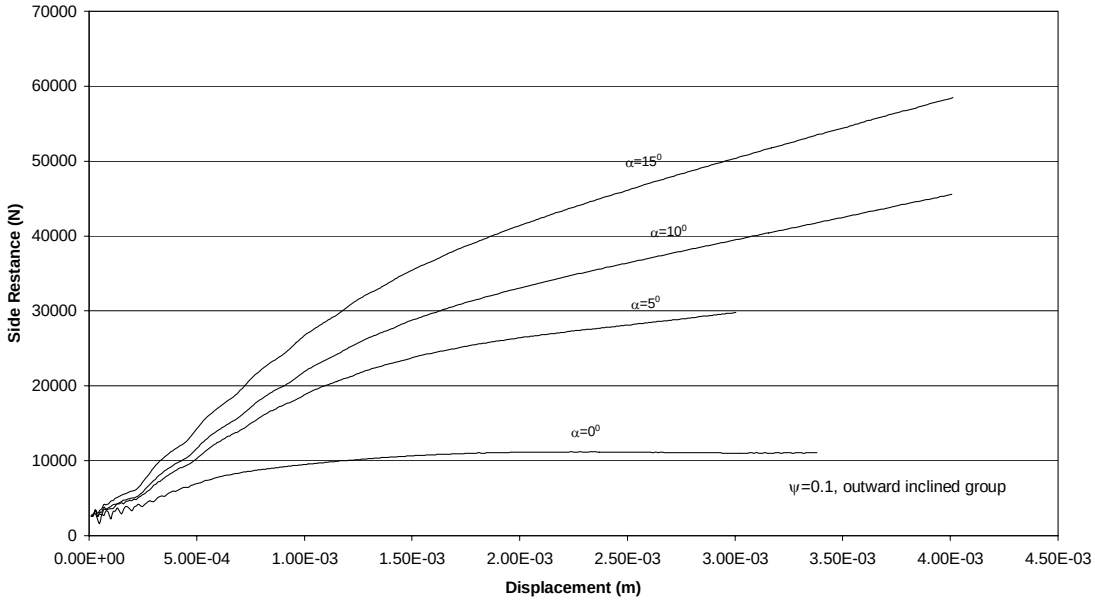

a) Side resistance variation with pile inclination

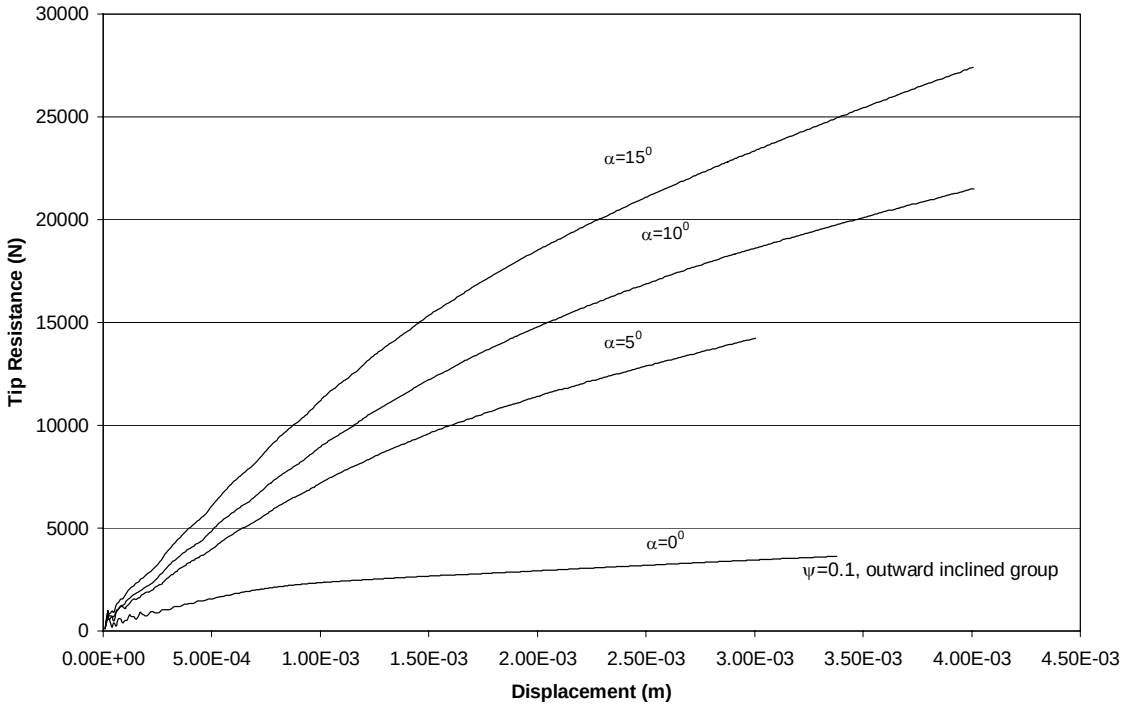

b) Tip resistance variation with pile inclination

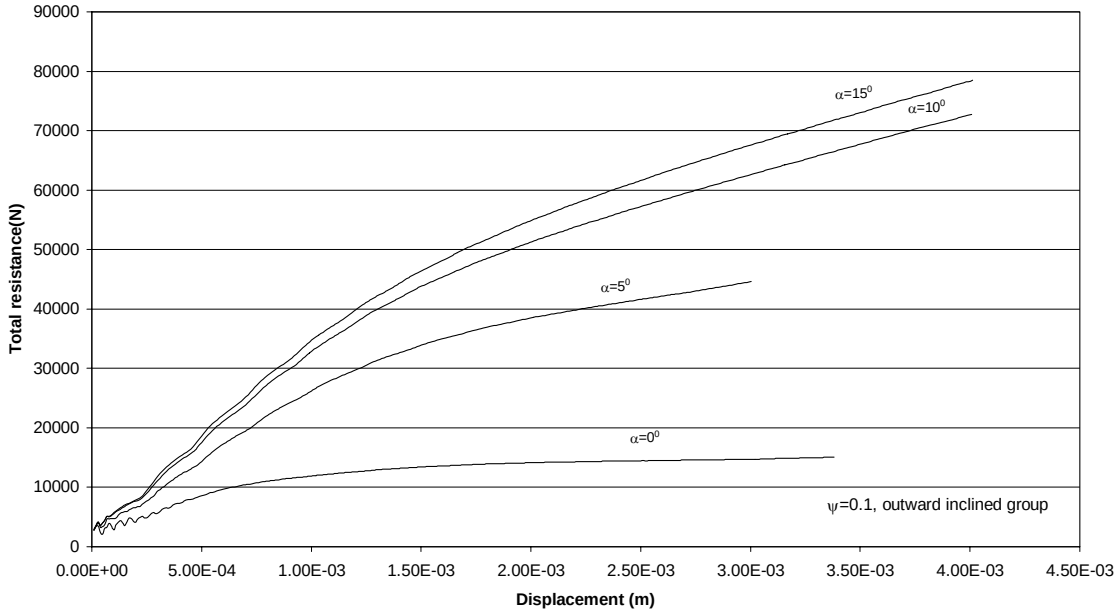

c) Total resistance variation with pile inclination

Figure 7-24 Inclination effect of outward inclined pile group for ψ=0.1

7.3.4 Performance of Inward Network Piles

Figures 7-25 to 7-27 show the variation of the side, tip and total resistance of inward inclined micropile group with inclination angle.

As observed in the cases of individual and outward group piles, the side resistance is a maximum in the case of a vertical pile for micropiles installed in dilative sand. The variation of the side resistance, however, does not show any consistent pattern with pile inclination angle (Figure 7-25 (a)). The total resistance of piles in dilative sand is observed to increase with pile inclination angle consistently (Figure 7-25 (c). The variation of tip resistance with inclination was not consistent (Figure 7-25 (b)).

The variation of side resistance of piles installed in critical state sand with inclination is mixed and different from that in dilative sand in that it reaches a maximum at an inclination angle of 10^0(Figure 7-26 (a)). The variation of the tip resistance of piles

installed in this sand was not consistent either Figure 7-26 (b). However, the total resistance of piles showed the same behavior as found in dilative sand (Figure 7-26(c)).

In the case of piles installed in contractive sand, total, side and tip resistances increased with pile inclination angle (Figures 7-27 (a), (b) and (c)).

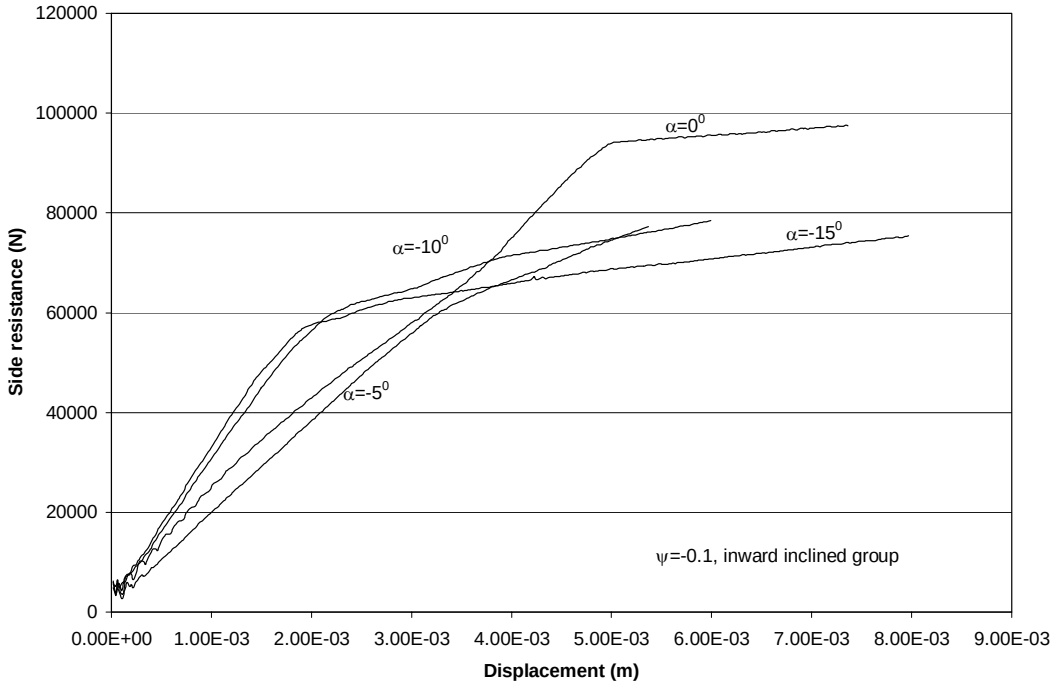

a) Side resistance variation with pile inclination

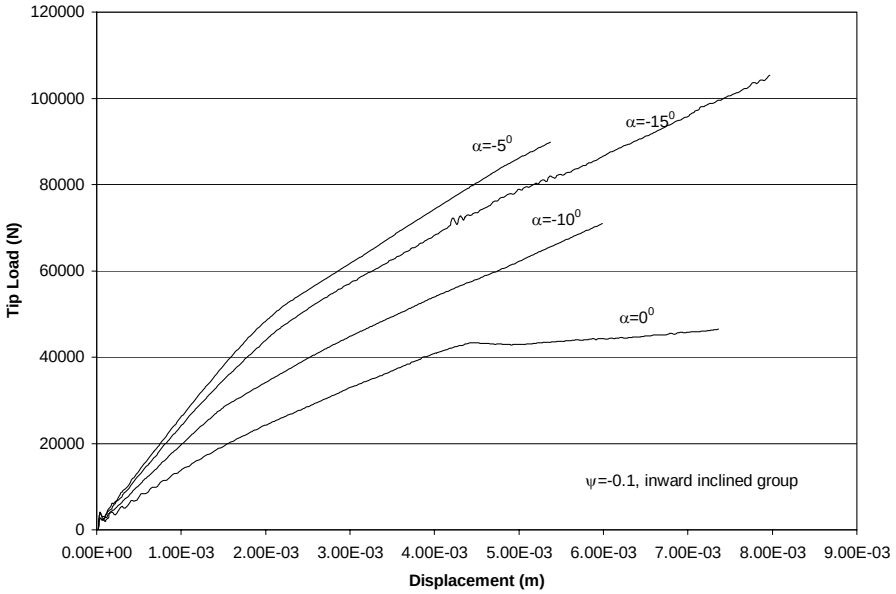

b) Tip resistance variation with pile inclination

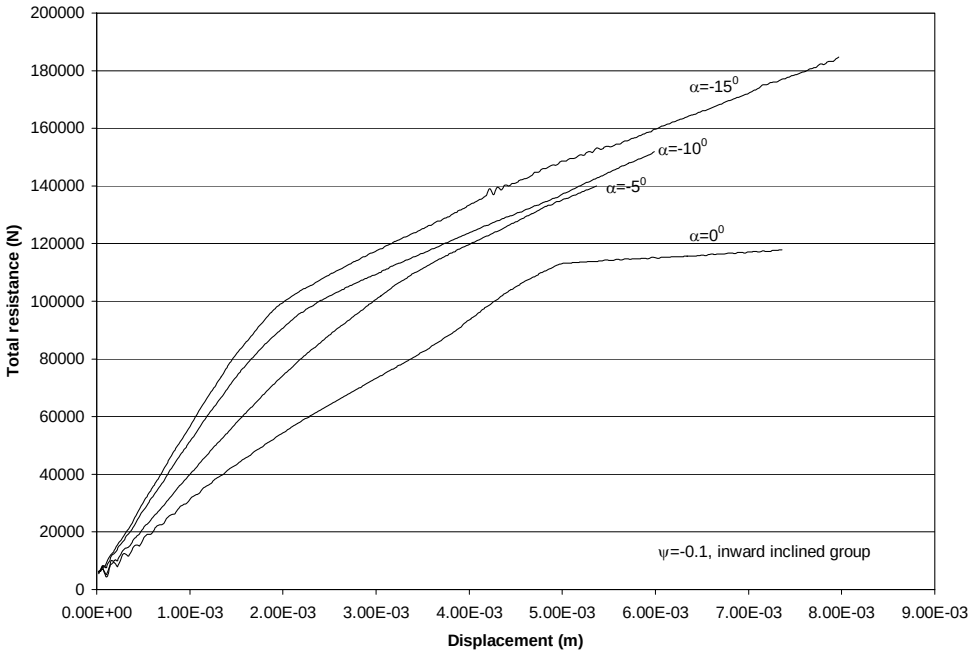

c) Total resistance variation with pile inclination

Figure 7-25 Inclination effect of inward inclined pile group for ψ=-0.1

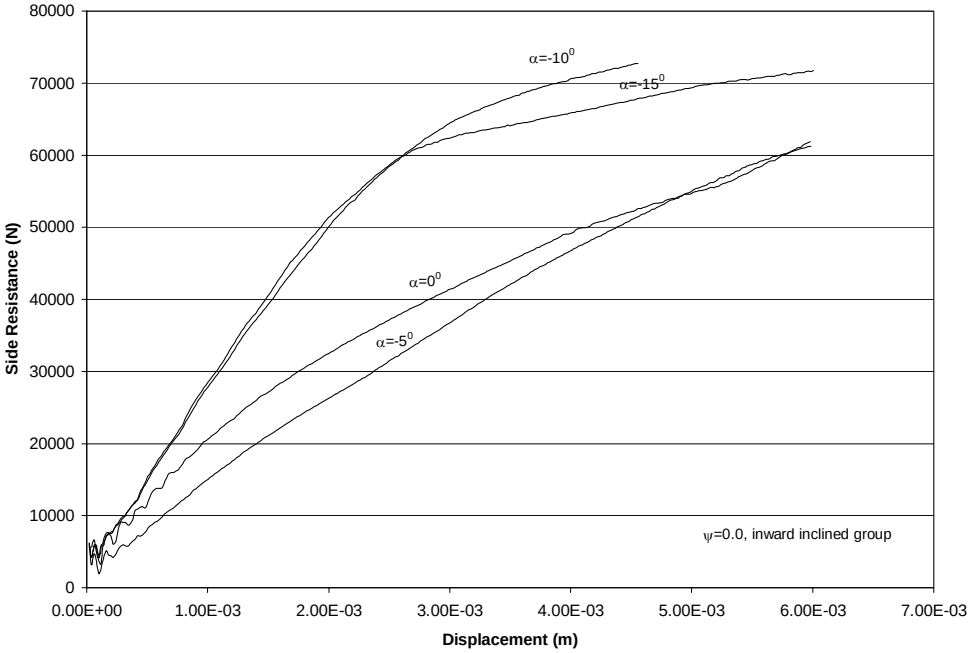

a) Side resistance variation with pile inclination

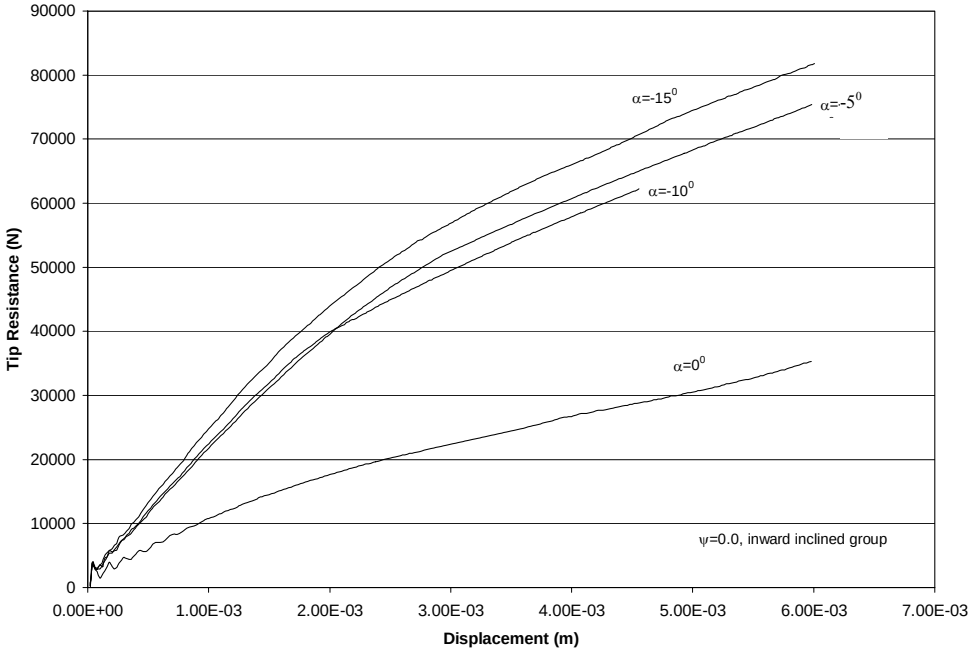

b) Tip resistance variation with pile inclination

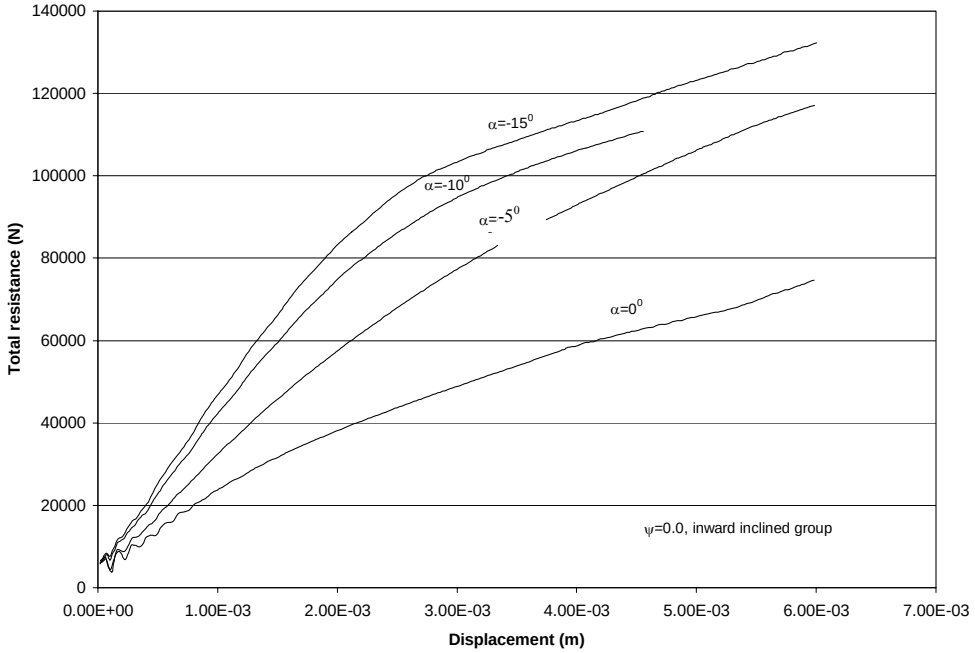

c) Total resistance variation with pile inclination

Figure 7-26 Inclination effect of inward inclined pile group for ψ=0.0

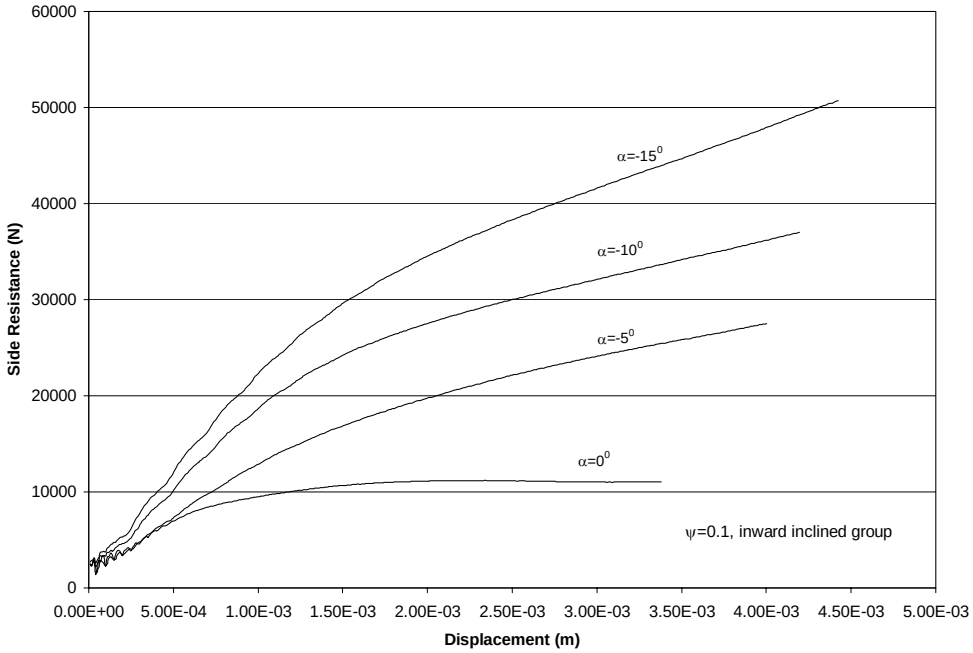

a) Side resistance variation with pile inclination

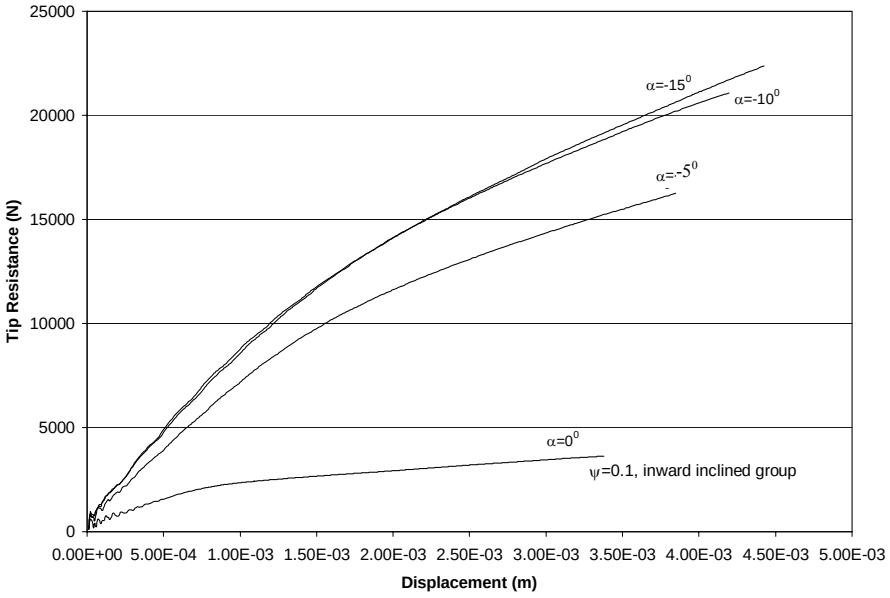

b) Tip resistance variation with pile inclination

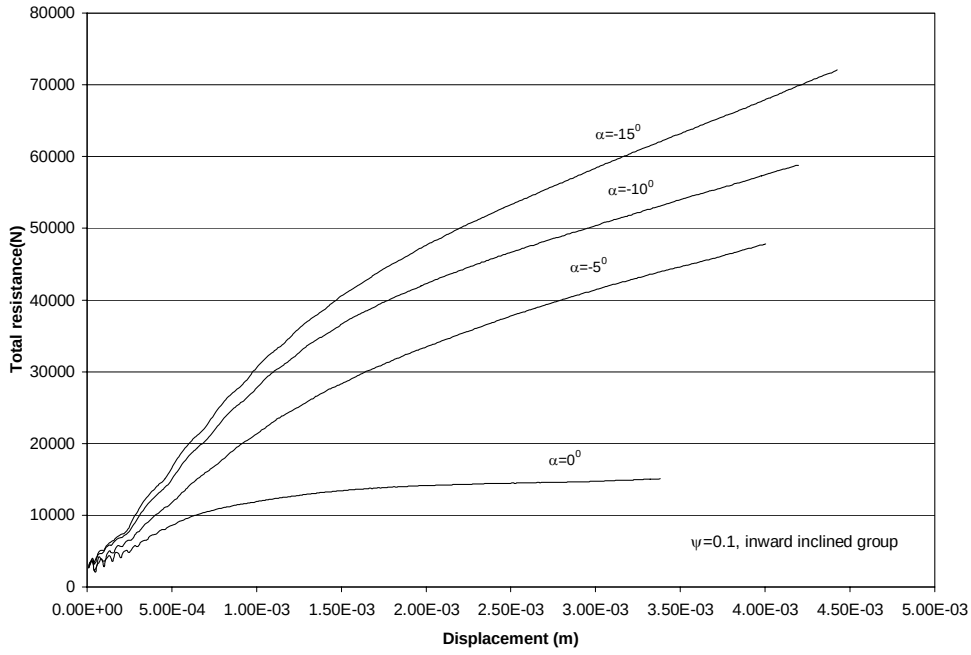

c) Total resistance variation with pile inclination

Figure 7-27 Inclination effect of inward inclined pile group for $\psi = 0.1$

7.3.5 Comparison of Inward and Outward Network Pile Performance

Figures from 7-28, 7-29 and 7-30 show comparison of the total resistance, side resistance and tip resistance of piles installed in dilative, critical state and contractive sands with same inclination angle but different inclination dip directions at inclination angles of 5^0, 10^0, and 15^0. It is seen that, without consideration of reinforcement effect by micropile network, side, tip and total resistances of outward inclined piles in all sand states are basically higher than those of inward inclined 'basket' micropile network. Exception to this occurs in the side resistance of the piles installed in critical state (ψ=0.0) sand with an inclination angle of 5^0 (Figure 7-29 (a)). It is noted that tip resistance of piles installed in contractive sand with an inclination angle of 15^0 and 5^0, dilative sand with an inclination angle of 5^0, and critical state sand with an inclination angle of 15^0 for both cases are very close (Figures 7-28 (a), 7-29 (c), 7-30 (a) and (c)).

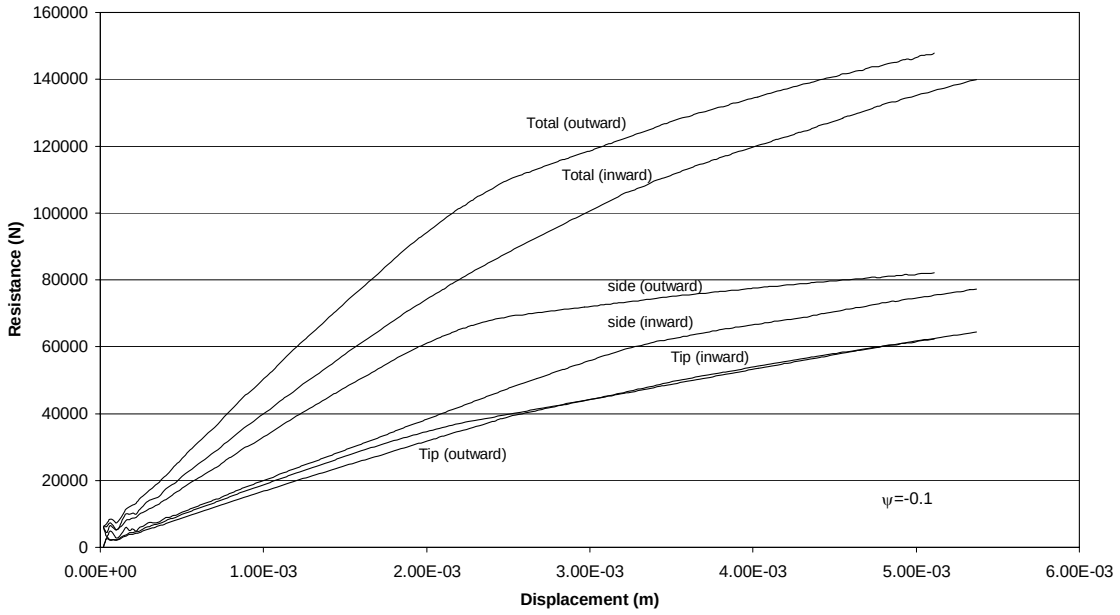

(a) $\alpha = 5^0$

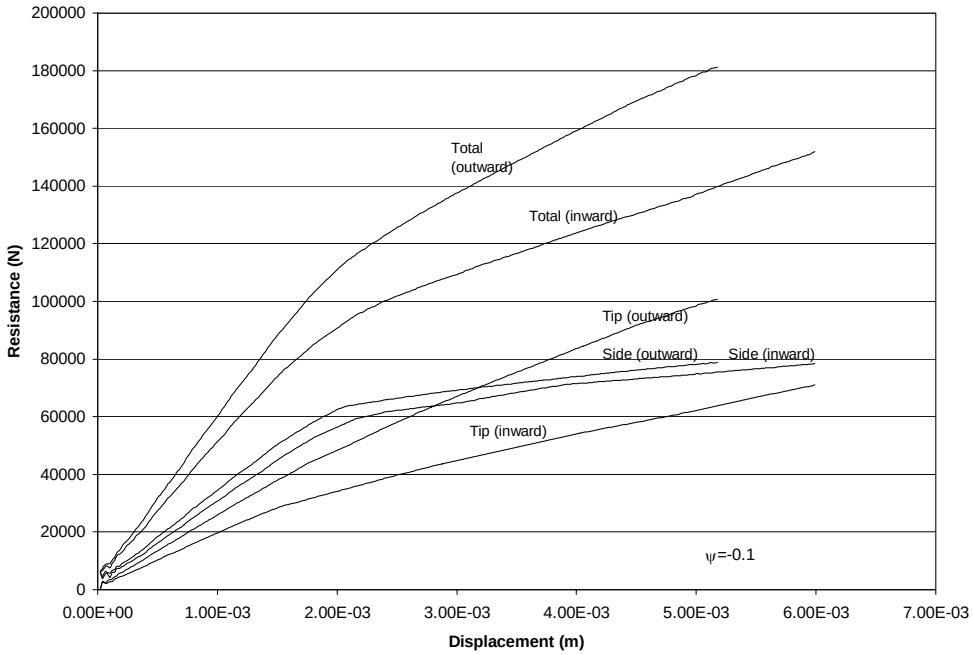

(b) $\alpha = 10^0$

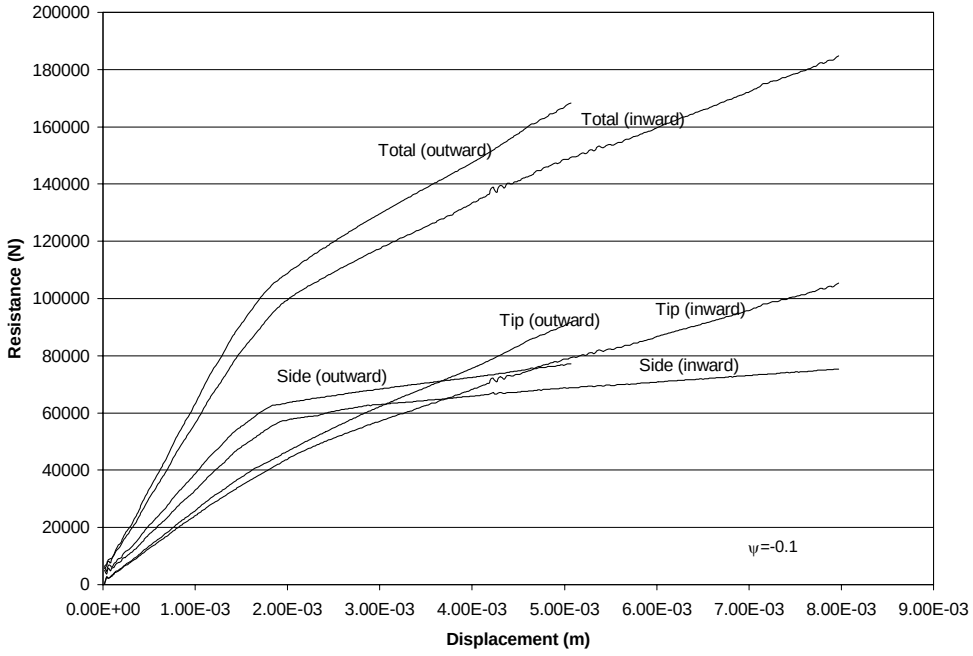

(c) $\alpha=15^0$

Figure 7-28 Comparison of inward and outward inclined pile network (ψ=-0.1)

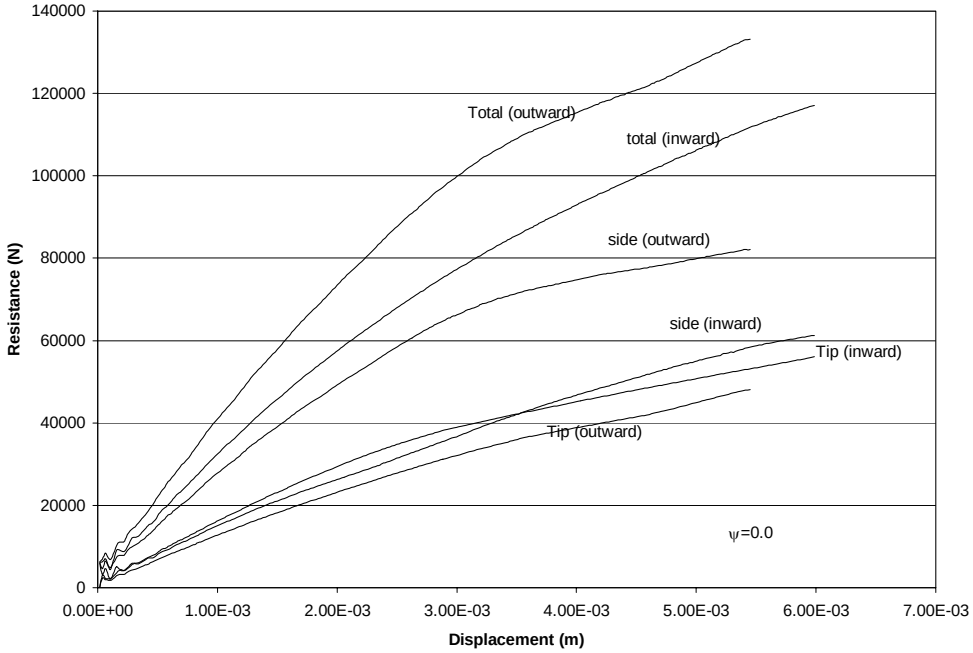

(a) $\alpha=5^0$

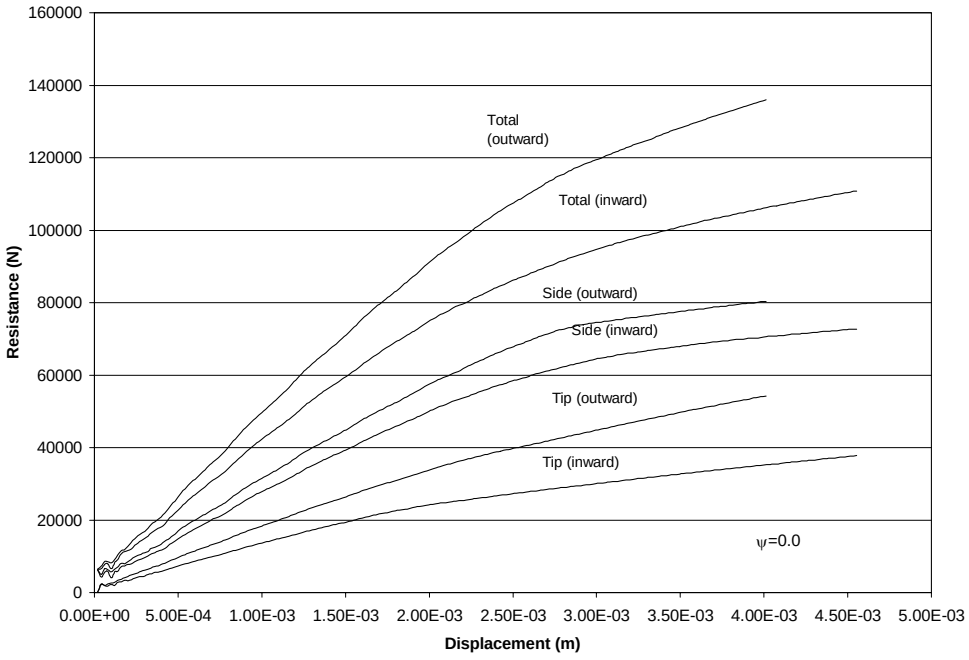

(b) $\alpha=10^0$

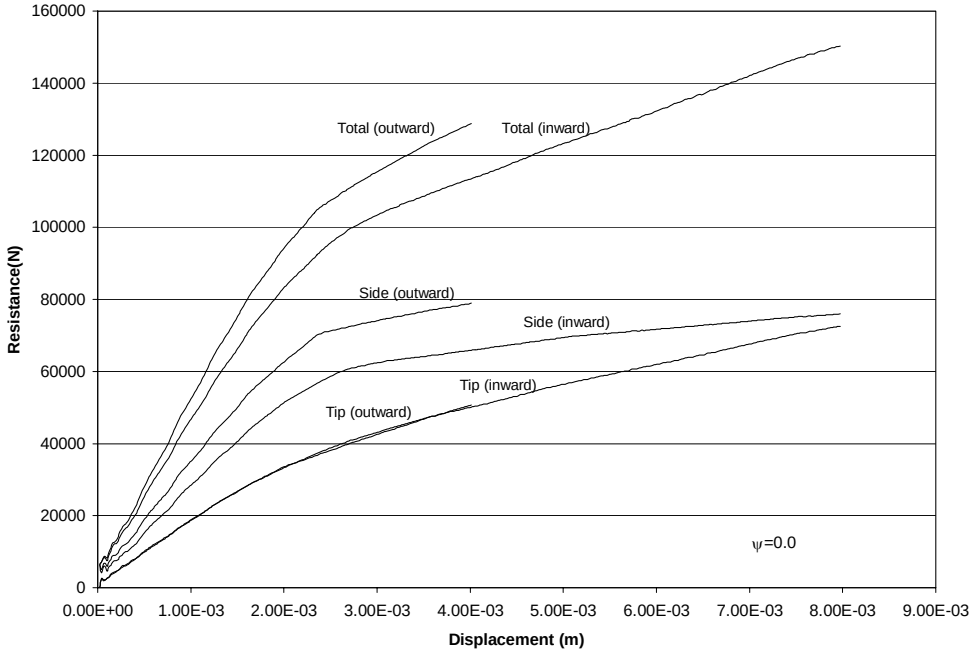

(c) $\alpha=15^0$

Figure 7-29 Comparison of inward and outward inclined pile network ($\psi=0.0$)

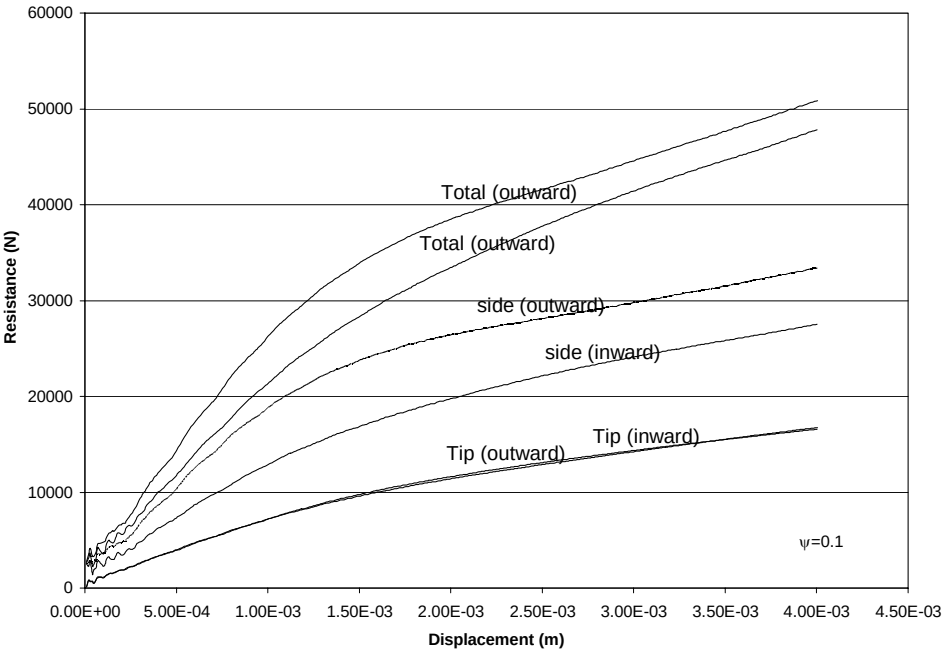

(a) $\alpha=5^0$

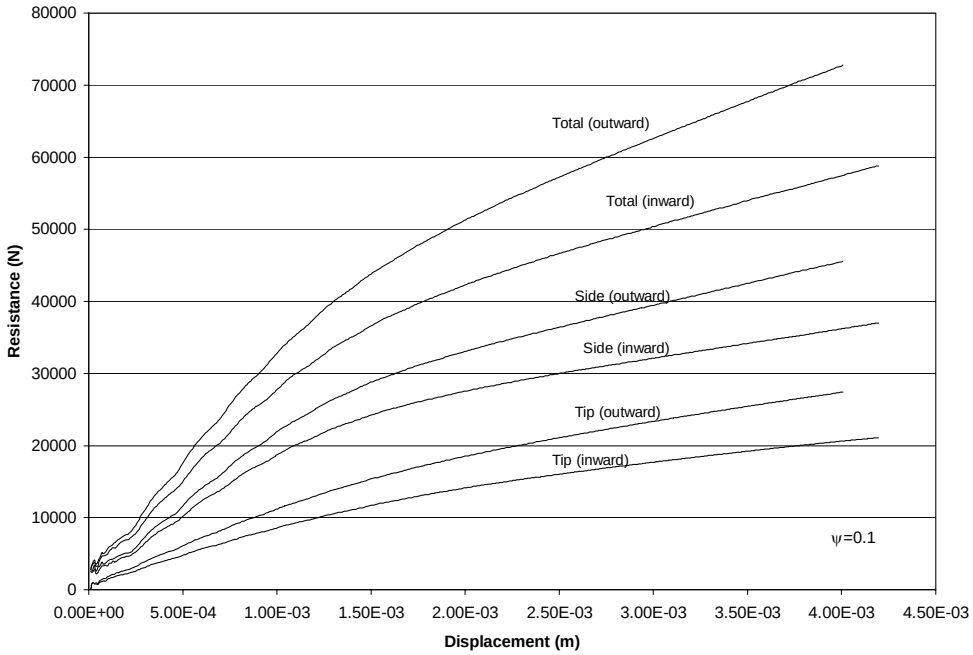

(b) $\alpha=10^0$

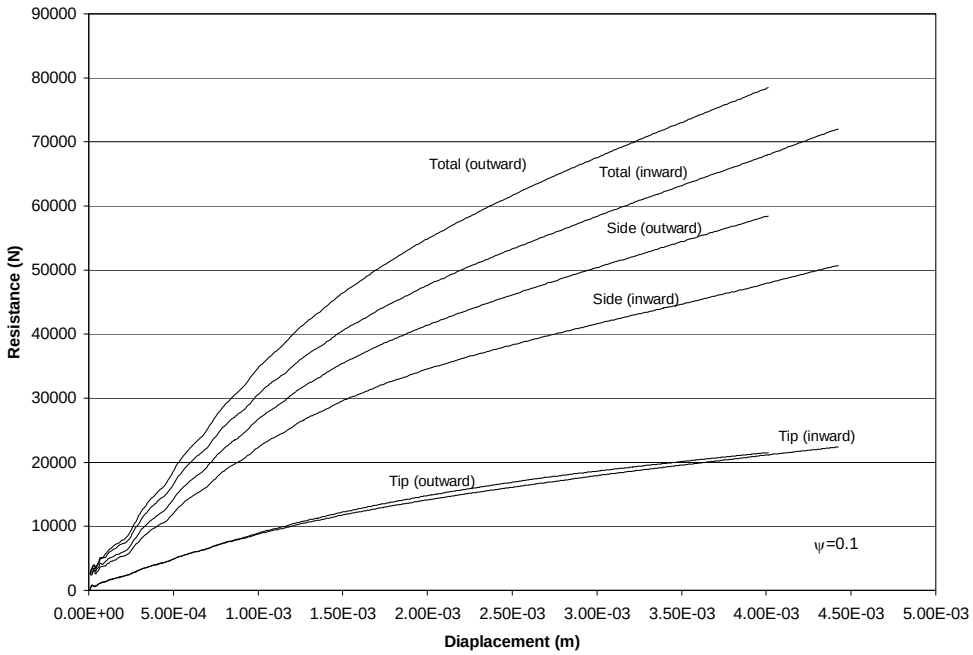

(c) $\alpha = 15^0$

Figure 7-30 Comparison of inward and outward inclined pile network (ψ=0.1)

7.3.6 Proposed Mechanisms of Load Transfer in Inclined and Network Piles

The numerical results of the performance of an inclined pile and network piles installed in sand under the three initial states, dilative, critical state, and contractive, enable us to put forward new mechanisms to describe the observed load transfer.

A vertical concentric load applied on an inclined pile or a pile group can be decomposed into two components: axial component parallel to the axis of the pile and a lateral component normal to it. The schematic of the initial distribution of normal stress due to the axial load on an inclined pile is as shown in Figure 7-31 (a). The distribution is approximated to be a linear for simplicity. Imposition of a lateral load component on the pile would alter the above distribution of the normal stress as shown in Figure 7-31 (b).

.

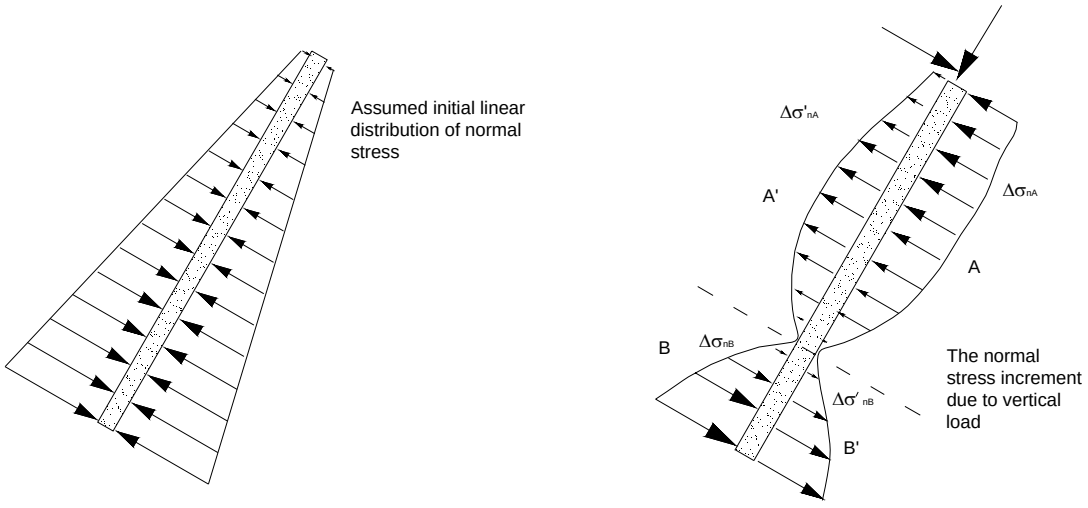

(a) (b)

Figure 7-31 Schematic of normal stress distribution on an inclined pile due to application of vertical load

The neighborhood of the pile is divided into 4 zones as shown in Figure 7-31 (b). Zones A and B are in passive state of pressure and zones A′ and B′ are in active state. The stress distribution is not symmetric due to the difference in passive and active earth pressure coefficients and development of potential gap along the interface.

The change in normal stress distribution would lead to corresponding changes in the load transfer of piles. First, it would result in a change of the shear strength along the pile. Second, it would alter the state of the sand surrounding the pile. The dilative sand in zone A would be loosened due to the squeezing but the contractive sand in zones A and B will be further densified. On the contrary, both contractive sand and dilative sand in zones A′ and B′ would be loosened. The alteration of sand state would lead to additional changes in the shear strength along the pile.

Since the passive earth pressure coefficient is much larger than the active earth pressure coefficient, the resulting normal stress change within the zones will be as follows:

$$\left|\Delta\sigma_{nA}\right| \geq \left|\Delta\sigma_{nA'}\right| \tag{7-1}$$

$$\left|\Delta\sigma_{nB}\right| \geq \left|\Delta\sigma_{nB'}\right| \tag{7-2}$$

where, $\left|\Delta\sigma_{nA}\right|$ is the absolute magnitude of normal stress increment applied to the pile in Zone A; $\left|\Delta\sigma_{nA'}\right|$ is the absolute magnitude of normal stress increment applied to the pile in Zone A'; $\left|\Delta\sigma_{nB}\right|$ is the absolute magnitude of normal stress increment applied to the pile in Zone B, and $\left|\Delta\sigma_{nB'}\right|$ is the absolute magnitude of normal stress increment applied to the pile in Zone B'.

As a result, the side resistance due to the variation in normal stress profile caused by the lateral load component would be increased. The lateral load is but a component of vertical load applied to the pile that is controlled by inclination angle. Increase in inclination angle will lead to a larger lateral component but a corresponding decrease in the axial load applied on the pile. However a large increase in inclination angle will decrease the depth of bottom of the pile, and make the total normal force applied the pile lower and decrease the side resistance.

The alteration of sand state due to lateral load will also change the side resistance along the pile. The normal stress and side resistance will be decreased when the surrounding sand is contractive, however the normal stress and side resistance will be increased when it is dilative. Figure 7-19 (a) shows that the side resistance is decreased when the pile is inclined in dilative sand. This is because the lateral component of the vertical load applied to the inclined piles would make the surrounding sand to dilate and loosen. This will in turn reduce the beneficial effect of shear induced dilation in the sand. Therefore, the ultimate side resistance of inclined pile group would be less than that of vertical pile group. Similar situation would occur in the sand with $\psi = 0.0$ (Figure 7-20 (a)).

In the case of contractive sand, however, the lateral component of the vertical load applied to the inclined pile would make the sand in zones A and B to be densified. Thus, shearing and contraction of the densified sand around the inclined pile would be less than that of contractive sand around a vertical pile. This would result in the ultimate side resistance of inclined pile to be larger than that of a vertical pile (Figure 7-21 (a)). The variation of ultimate side resistance with inclination angle of outward and inward

micropile groups would essentially follow the same variation as the individual pile with only a few exceptions as noted in case of the critical state sand. A summary of the observed behavior is tabulated in Table 7-1.

Table 7-1 Ultimate side resistance variation with pile inclination

	sand types			References
	ψ=−0.1	ψ=0.0	ψ=0.1	
Individual micropile	decrease	decrease	increase	Figures 7-19, 20, 21 (a)
Outward inclined micropile group	decrease	increase	increase	Figures 7-22, 23, 24 (a)
Inward inclined micropile group	decrease	mixed	increase	Figures 7-25, 26, 27 (a)

The tip resistance of inclined micropile increases with inclination angle regardless of the state of sand and the geometry of the pile installation (Figures 7-19, 20, 21, 22, 23, 24, 25, 26, and 27 (b)). Only few exceptions occur in outward inclined pile group and inward inclined pile group in both dilative and the sand with ψ = 0.0 (Figures 7-22 (b), 7-23 (b) and Figures 7-25 (b), 7-26 (b)).

It is of interest to find that the side resistance of outward inclined pile group for a given inclination angle is always larger than that of inward pile group regardless of the state of sand and pile geometry (Figures 7-28, 7-29 and 7-30). A plausible mechanism for this observation is described as follows.

Figure 7-32 shows two piles arranged in vertical, inward, and outward arrangement. The spacing between the mid points, D_{mid}, and the tip, D_{tip} of inclined piles are related to the spacing D of vertical piles as:

$$D < D_{mid}^{-\alpha} < D_{mid}^{\alpha} \tag{7-3}$$

$$D < D_{tip}^{-\alpha} < D_{tip}^{\alpha} \tag{7-4}$$

where –α indicates that the pile group inward inclined with an angle of α, but +α indicates that the pile group outward inclined with same angle of α..

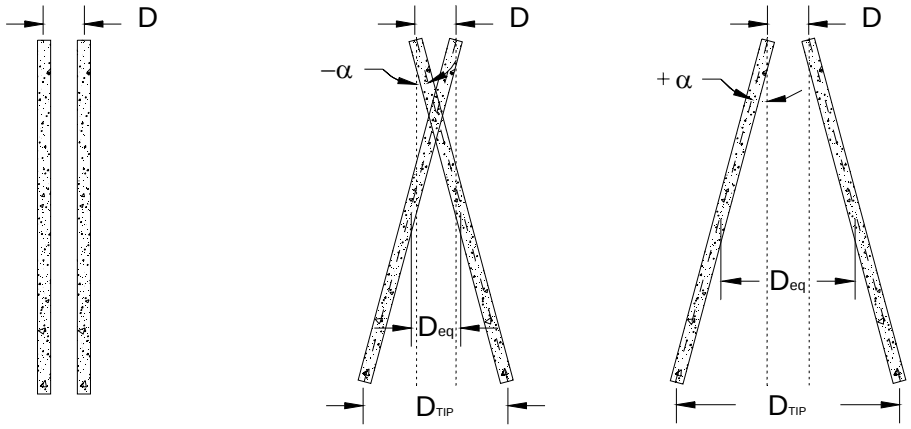

Figure 7-32 Pile spacing of vertical, inward inclined and outward inclined pile groups

The lateral component induced by the inclination of micropiles leads changes in normal stress and state as discussed before in the case of an inclined pile. In the case of dilative sand these changes would reduce the beneficial effect of shear induced dilation. The amount of decrease would be less for outward inclined pile group rather than for inward inclined pile group as D_{mid} of the latter is less. Thus, the sand within inward inclined pile group would be more prone to dilate than that in the outward inclined pile group after the beneficial effect of shear induced dilation is reduced.

The contractive sand within the inward inclined pile group would also be more susceptible to densification than that within an outward inclined group. This densification will increase the ultimate side resistance. However, the contractive sand within the inward inclined sand would be more susceptible to contract by shearing as well. The

contraction will reduce the ultimate side resistance. The ultimate side resistance is finally balanced by both the increase induced by densification and the reduction induced by contraction. From Figure 7-30, it is found that the ultimate side resistance may still be dominated by contraction resulting in a decrease in normal stress along the piles instead by densifying of contractive sand leading to increases in normal stress and shear strength along piles. Therefore, inward inclined pile group with less D_{mid} would be more susceptible to decrease in the normal stress and ultimate side resistance than an outward inclined pile group that had larger pile spacing between mid points.

The tip spacing (Equation 7-4) and the relative magnitudes of pile spacing for vertical, inward inclined and outward inclined pile group are same as those for side resistance case. Therefore, the tip resistance would not change much for both inward and outward inclined pile groups.

Finally it is noted that the above discussion on the mechanisms of load transfer was based on inclination angles in a range of 0-15°. Further studies are needed before the discussion can be extended for other inclinations.

CHAPTER 8
SUMMARY AND CONCLUSIONS

8.1 Summary

This study implemented a state parameter based constitutive model for sand. The state parameter is a combined measure of the void ratio and confining stress. Past studies have treated the effects of void ratio and confining stress separately. It had led to problems associated with the interpretation of sand behavior in many laboratory and field tests. The widely used terms of loose and dense sand behavior of sand was contrasted with contractive and dilative characteristics.

The bounding surface sand model was formulated within the critical-state framework following Li and Dafalias (2000) and Li (2002). The state parameter ψ, expressed as the difference between the current void ratio and the void ratio at the critical state at same confining stress was explicitly incorporated into this model. The model assumes the dilatancy of sand to be dependent not only on the stress ratio $\eta = q/p$, but also on the state parameter. The model was coded in C++ language and implemented into the widely used geotechnical finite difference code FLAC3D. The code was first verified by comparison with laboratory tests and then used to simulate the results of a full scale study on micropiles. The model highlighted the dependency of the shear behavior of sand on stress path and Lode angle.

FLAC3D model was subsequently used to investigate the effects of sand state on the performance of single, group, and network micropiles. The study focused on the variation of side and tip and resistance with pile displacement.

8.2 Conclusions

Based on numerical analysis of a laboratory element tests, single micropile and three-pile micropile group and network, the following conclusions are drawn:

1. Shear behavior of sand is very much dependent on state, stress path, and Lode angle. The constitutive model formulated in the study can capture the complex characteristics of sand shear behavior.
2. Sand resistance to a single pile and micropile consists of two components: one based on critical state friction and the other due to dilatancy. The critical state friction is dependent on mineral and particle characteristics and not on the initial state. Dilatancy on the other hand depends on state parameter. The normal stress imposed on the periphery of the pile is affected by dilatancy. Thus, the side resistance and total resistance are affected by initial state. The numerical simulations confirmed this important effect on resistance to pile.
3. The stress overlapping due to group effect in micropiles contributes to an increase in shaft resistance.
4. The group effect on shaft resistance of displacement piles in dilative sand would be either positive or negative. This is determined by both value of initial state parameter and the degree of displacement. On the contrary, in contractive sands the side resistance of piles in group is always positive and dominated by the amount of displacement.
5. For bored piles with good bond between pile and its surrounding sand, especially micropiles injected with high pressure, group effects of shaft resistance of piles in dilative sand contributed by both friction and dilatancy are positive; group effects

of shaft resistance of piles in contractive sand contributed by dilatancy is negative. Thus, the resultant group effect on shaft resistance of pile in contractive sand might be either positive or negative. The final values is determined by the relative magnitude of the positive group effect contributed by friction and the negative group effect contributed by dilatancy.

6. The total group effect of tip resistance is positive for contractive sand, but it is negative for dilative sand. As a result overlap of stress in group piles its contribution to tip resistance is positive when pile spacing large (3D or 4 D), but negative when the pile spacing is small (2D).
7. For piles installed in dilative sand with inclination angle less than 15^0 (individual, inward and outward network), ultimate shaft resistance is less than that of vertical piles. However, the behavior is opposite for piles installed in contractive sand.
8. The tip resistances of inclined piles are always larger than those of vertical piles for both contractive sand and dilative sand.
9. When micropiles are considered as structure elements, shaft resistances of outward inclined micropiles are higher than those of inward inclined micropiles regardless of the state of sand. However, the tip resistances are nearly the same for both inclined piles.
10. The group effect of micropiles and piles in sand depends on types of installation, sand state, pile spacing, ratio of length over diameter, properties of pile-sand interface. The FLAC3D model developed here is a useful means of quantifying the effects for design.

8.3 Suggestions for Further Research

The important effects of initial state identified by the numerical analyses on micropiles could be enhanced by the use of physical centrifuge models. Centrifuge is the only type of tests that can control of both density and confinement.

The computations using FLAC3D were limited by computer RAM. Thus, the number of piles in group and network was limited to only three piles. The analyses could be extended to a larger number of piles within a group and network using parallel processing computational algorithms.

The study focused on effect of vertical loads on the performance of piles. Recent problems with geotechnical infrastructure have brought forth the need to study the response of micropiles under lateral loads. Their response under lateral loads as a function of state remains unexplored. Since FLAC3D is a 3-D program it will be useful to extend the analyses to lateral loads as well. It is also necessary to extend the numerical analyses to micropiles under dynamic loading.

The study did not account for the reinforcement effect of inward network piles. Such effect would change the initial state of sand by changing both void ratio and confining stress. Thus, it is necessary to develop a model that can predict changes in initial state during installation of network piles.

Finally, even though the constitutive model used in the study is useful for modeling complex situations it uses a large number of parameters. It is necessary to examine the influence of the parameters on sand response and limit the numbers to only the most important ones. Such a model is currently under development at Washington State University.

REFERENCES

Atkinson J., 1993, An introduction to the Mechanics of Soils and foundations through Critical State Soil Mechanics, McGraw-Hill

Baker, R. and Desai, C. S., 1982, Consequences of deviatoric normality in plasticity with isotropic strain hardening. *Int. J. Numer. Anal. Methods Geomech.*, 6(3), 383-390.

Bardet, J. P., 1990, Hypoplasticity model for sand, Journal of engineering mechanics, 116 (9), 1973-1998.

Been, K. and Jefferies, M. G., A state parameter for sands, *Geotechnique*, 35(2),99-112.

Been, K., Crooks, J. H. A., Becker, D. E. and Jefferies, M. G., 1986, The cone penetration test in sands: part I, state parameter interpretation, *Geotechnique*, 36(2), 239-249.

Been, K., Jefferies, M. G., Crooks, J. H. A. and Rothenburg, L., 1988, The cone penetration test in sands: part II, general inference of state, *Geotechnique*, 37(3), 285-299.

Benslimane, A., Juran, I., and Bruce, D. A., 1995, Group and network effect in micropile design practice, Foundation upgrading and repair for infrastructure improvement, *Proceedings of the symposium* sponsored by the deep foundations committee of the grotechnical engineering division of American society of civil engineers in conjunction with the ASCE convention in San Diego, California, October 23-26, 1995.

Boulanger, R. W., 2003, Relating K_α to relative state parameter index, *Journal of geotechnical and geoenvironmental engineering*, 129(8), 770-773.

Bruce, D. A., DiMillio, A. F., and Juran, I., 1995, Primer on Micropiles, *Civil Engineering*, 65(12) 51-54.

Brown, D and Drew, C., 2000, Axial capacity of augured displacement piles at Auburn University, *Proceedings of Geo-Denver 2000*, Denver, CO, 397-403.

Bustamante, M. & Gianeselli, L. 1993, Design of auger displacement piles from in situ tests, *Proceedings of the 2th international geotechnical seminar on deep foundation on bored and auger piles*, Ghent, Belgium, 21-34.

Cantoni, R., Collotta, T., Ghionna, V. N. and Moretti, P. C., 1989, A design method for reticulated micropile structures in sliding slopes, *Ground Engineering*, No. 5, 41-47.

Carriglio, F., Ghionma, V. N., Jamiolkowski, M. and Lancellota, R., 1990, Stiffness and penetration resistance of sands versus state parameter, *Journal of geotechnical engineering*, 116(6), 1015-1020.

Dafalias, Y. F., and Popov, E. P., 1976, Plastic internal variables formalism of cyclic plasticity, *Journal of applied mechanics*, ASME, 43, 645-651

Dafalias, Y. F., 1981, A novel bounding surface constitutive law for the monotonic and cyclic hardening response of metals, *Transactions*, 6th international conference on SMIRT, Vol. 1, paper No. L 3/4,Paris, France, August, 1981.

Dafalias, Y. F., 1986, Bounding surface plasticity. I: Mathematical foundation and hypoplasticity, *Journal of Engineering Mechanics*, 112(9), 966-987.

Dafalias, Y. F., Papadimitriou, A. G., Li, X. S., 2004, Sand plasticity model accounting for inherent fabric anisotropy, Journal of Engineering Mechanics, 130(11), 1319-1333.

Drucker, D. C., 1988, Conventional and unconventional plastic response and representation, *Appl. Mech. Rev.*, 41,151-167.

Ellis, I., 1985, Piling for underpinning, *Symposium on building appraisal, maintenance and preservation*, at University of Bath, Bath, 88-96

Estephan R. et Frank R., 2001, Analyse du comportement de groupe et de réseaux élémentaires de micropieux sous chargement vertical et horizontal. Application aux essays de chargement du réseau de Saint-Rémy-lés-Chevreuse. Rapport interne N0FO/98-99/06.

Foerster, E. et Modaressi, H. 1995, Modélisation en elements finis des réseaux ou des groupes de micropieux. Rapport interne No. FO/94/04.

FOREVER, 2002, Synthesis of the results of the national project on micropiles. Research Report, IREX.

Garg, K. G., 1979, Bored pile groups under vertical load, *Journal of the geotechnical engineering division*, Proceedings of the American Society of Civil Engineers, 105 (GT80).

Gaudin C., Serratrice J.F., Thorel L., Garnier J. (2002) : Caractérisation du comportement d'un sol par essais triaxiaux pour la modélisation numérique d'un écran de soutènement. Symposium International Identification et détermination des paramètres des sols et des roches pour les calculs géotechniques, 2-4 Sept. 2002, Paris, France, 8 p (90%).

Hana, T. H., 1963, Model studies of foundation groups in sand, *Geotechnique*, 13, 334-351.

Hashiguchi, K.,1980, Constitutive equations of elastoplastic materials with elastic-plastic transition, *Journal of Applied Mechanics*, 47 (2), 266-272.

Hashiguchi, K.,1989, A mathematic modification of two surface model formulation in plasticity, *International journal of solids structure*, 25 (8), 917-945.

Hashiguchi, K., Saitoh, K., Okayasu, T. and Tsutsumi, S., 2002, Evaluation of typical conventional and unconventional plasticity models for prediction of softening behavior of soils, *Geotechnique*, 52(8), 561-573.

Hart, R. D., and C. Detournay, 2005, Geotechnical constitutive models in an explicit, dynamic solution scheme, Soil constitutive models: evaluation, selection and calibration (Proceeding of geo-frontiers 2005, Austin, Texas, January 2005), ASCE geotechnical special publication No. 128, pp. 185-203.

Herrmann, L. R., Kaliakin, V., Shen, C. K., Mish, K. D. and Zhu, Z. Y., 1987, Journal of engineering mechanics, 113 (4), 500-519.

Hill, R., 1950, *The mathematical theory of plasticit*y, The Oxford Engineering Science Series 11, Oxford University Press, Oxford, UK.

Ismael N.F, Axial Load Tests on Bored Piles and Pile Groups in Cemented Sands, *Journal of Geotechnical and Geoenvironmental Engineering* ,Vol.129 ,pp.184-185 ,February ,2001 .

Itasca Consulting Group, Inc. FLAC3D, Fast Lagrangian Analysis of Continua in 3 Dimensions User's Guide, Version 2.1, 2002.

Jovicic, V. and Coop, M. R., 1997, Stiffness of coarse grained soils at small strains, *Geotechnique*, 47(3), 545-561.

Juran, I., Bruce, D. A., Dimillo, A. and Benslimane, A., 1999, Micropiles: the state of practice. Part II: design of single micropile and groups and networks of micropiles, *Ground improvement*, 3, 89-110.

Klotz, E. U. and Coop, M. R., 2001, An investigation of the effect of soil state on the capacity of driven piles in sands, *Geotechnique*, 51(9), 733-751.

Konrad, J. M., 1996, In situ sand state from CPT: evaluation of unified approach at two CANLEX sites, *Canadian Geotechnical Journal*, 34,120-130.

Konrade, J. M., 1998, Sand state from cone penetraometer tests: a framework considering grain crushing stress, *Geotechnique*, 48(2), 201-215.

Krieg, R. D. 1975, A practical two-surface plasticity theory, *Journal of applied mechanics*, ASME, 42, 641-646.

Lee, C.J., Bolton, M. D. and Al-tabbaa, A., 2002, Numerical medalling of group effects on the distribution of dragloads in pile foundations, *Geotechnique*, 52 (5), 325-335.

Li, X. S., 1997, Modeling of dilative shear failure, *Journal of geotechnical and geoenvironmental engineering*, 123(7), 609-616.

Li. X. S., Dafalias, Y. F. and Wang, Z. L., 1999, State-dependent dilatancy in critical-state constitutive modeling of sand, *Canadian Geotechnical Journal*, 36, 599-611.

Li, X. S. and Dafalias, Y. F, 2000, Dilatancy for cohesionless soils, *Geotechnique*, 50(4), 449-460.

Li, X. S., 2002, A sand model with state-dependent dilatancy, *Geotechnique*, 52(3), 173-186.

Lizzi, F., 1978. Reticulated root piles to correct landslides, Proceedings, ASCE Annual Meeting, Chicago.

Lizzi, F., 1985, 'Pali radice' (root piles and ' reticulated pali radice', *Underpining*, Glasgow [Lanark]: Surrey University Press, 84-151.

Lo,1967, Discussion to paper by Y.O. Beredugo. *Canadian Geotechnical Journal*, Volume 4, pp.353-354.

Sadek, M and Shahrour, I., 2004, A three dimensional embedded beam element for reinforced geomaterials, *Int. J. Numer. Anal. Meth. Geomech.*, 28:931-946.

Sadek, M., 2002, Three-dimensional finite element modeling of reinforced soil by micrpiles. Ph.D. Thesis, University of Sciences and Technologies of Lille, France.

Manzari, M. T. and Dafalias, Y. F., 1997, A critical state two-surface plasticity model for sand, *Geotechnique*, 47(2), 255-272.

Masad, E. A. and Muhunthan, B. 2000, Three-Dimensional Characterization and Simulation of Anisotropic Soil Fabric, *Journal of Geotechnical and Geoenvironmental Engineering*, ASCE, Vol. 126, No. 3, pp. 199 - 207.

Ming, H. Y. and Li, X. S., 2003, Fully Coupled analysis of failure and remediation of lower San Fernando Dam, Journal of geotechnical and geoenvironmental engineering, 129 (4), 336-349.

Misra, A. and Chen, C. H., 2004, Analytical solution for micropile design under tension and compression, *Geotechnical and geological engineering*, 22, 199-225.

Mroz, Z., 1967, On the description of anisotropic workhardening, Journal of the mechanics and physics of solids, 15, 163-175.

Nair, K. Gray, H and Donovan, N. C., 1969, Analysis of pile group behavior,

Performance of deep foundations, ASTM STP 444, 118-159.

NeSmith, W. M., 2002, Static capacity analysis of augered, pressure-injected displacement piles, Proceedings, Deep Foundations 2002: An International Perspective on Theory, Design, Construction, and Performance, Orlando, Florida.

Nusier, O. K. and Alawneh, A. S., 2004, Micropile technique to control upward movement of lightweight structures over expansive soils, *Geotechnical and geological engineering*, 22, 89-104.

O'Neil,1983, Group action in offshore piles. Proceedings. ASCE Conference, Geotechnical Practice in Offshore Engineering , Austin,pp. 25-64.

Pillai, V. S. and Muhunthan, B., 2002, Discussion on 'An investigation of the effect of soil state on the capacity of driven piles in sands, *Geotechnique*, 52(8), 620-621.

Pearlman, S. L., cambell, B. D. and Withiam, J. L., 1992, Slope stabilization using in situ earth reinforcements, *ASCE specialty conference on stability and performance of slopes and embankments-II*, June 29-July 1, Berkeley, California.

Plumelle, C., 1984, ''Improvement of the Bearing Capacity of Soil by Inserts of Group and Reticulated Micropiles,'' *Proceedings,* International Conference on In-situ Soil and Rock Reinforcement, Paris, France, pp. 83–89.

Randolph, M. F., 2003, Science and empiricism in pile foundation design, *Geotechnique*, 53 (10), 847-875.

Richart, F. E. Jr., Hall, J. R. & Woods, R. D. (1970). Vibrations of soils and foundations. International Series in Theoretical and Applied Mechanics, Englewood Cliffs, NJ: Prentice-Hall.

Rowe, P. W., 1962, The stress-dilatancy relation for static equilibrium of an assembly of particles in contact. *Proc. Roy. Soc. Lond*. A269, 500-527.

Rosco, K. H., Schofield, A. N. and Wroth, C. P., 1958, On the yielding of soils, *Geotechnique*, 8(1), 22-53.

Russo, G., 2004, Full-scale load tests on instrumented micropiles, Proceedings of the institution of civil engineers, *Geotechnical engineering 157*, Issue GE3, 127-135.

Sadek, M. and Shahrour I., 2001, Finite element modeling of inlined micropiles, *International workshop on micropiles- IWM 2001*, France.

Schofield, A.N. and Worth, P. (1968). *Critical State Soil Mechanics*, McGraw-Hill.

Shahrour, I. And Juran I., 2004, Seismic behaviour of micropile systems, *Ground*

improvement, 8 (3), 109-120.

Sharma, S., 2001, Micropile design and construction guidelines, Implementation Manual, CD Version, Publication No. FHWA-SA-97-070.

Vesic, 1969, Experiment with instrumented pile groups in sand. ASTM Special Technical Publication No. 444, pp. 172-222.

Wang, Z. L., Dafalias, Y. F. and Shen, C. K., 1990, Bounding surface hypoplasticity model for sand, *Journal of engineering mechanics*, 116(5), 983-1001.

Wang, Z. L. & Makdisi F. I., 1999, Implementing a bounding surface hypoplasticity model for sand into the FLAC program, FLAC and numerical modeling in geomechanics, Detournay, C. and Hard, R., eds, Balkema, The Netherlands, 483-490.

Wang, Z. L., Dafalias, Y. F., Li, X. S. and Makdisi, F. I., 2002, State pressure index for modeling sand behavior, *Journal of geotechnical and geoenvironmental engineering*, 128 (6), 511-519.

White, D. J. and Bolton, M. D., 2004, Displacement and strain paths during plane-strain model pile installation in sand, *Geotechnique*, 54(6), 375-397.

White, D. J. and Lehane, B. M., Friction fatigue on displacement piles in sand, *Geotechnique*, 54 (10), 645-658.

Wroth, C.P., Bassett, R.H., 1965. A stress–strain relationship for the shearing behavior of a sand. *Geotechnique*, 15, 32–56.

Wood , D. M., Belkher, K. and Liu, D. F., 1994 1984, Strain spftening and state parameters for sand modeling, *Geotechnique*, 44(2), 335-339.

APPENDIX A

A.1 Bounding Surface Plasticity

The bounding surface concept proposed by Dafalias (1986) was motivated by the observation that any stress-strain curve for monotonic loading or for loading-unloading process eventually converges to certain "bounds" in the stress-strain space. Description of plastic deformation within the bounding surface is achieved through a variable plastic modulus, which is often defined as a continuous function of the distance from the current stress to a properly defined image stress on the bounding surface. Figure A1 describes this concept on the uniaxial stress-plastic strain space. The plastic modulus, E_p, depends upon the distance, δ, between the current state of stress and a corresponding stress on the bounding line. In the elastic region, *CD*, the plastic modulus, E_p, is infinite. *At Point B*, E_p has a finite value, which decreases as the process goes to *C*. The zone *CC′* represents a plastic behavior during which E_p is assumed to remain constant. The stress-strain response is thus bounded by the two lines

Figure A2 shows the schematics of the bounding surface concept in a two-dimensional stress space. The outer surface is the bounding surface and the inner surface is the loading surface. The bounding surface always encloses the loading surface inside of which represents the elastic behavior. Any given stress state within or on the bounding surface is projected onto a "image" stress point on bounding surface by proper mapping rule. And the plastic strain modulus at current stress state is specified based on: i) a measure of distance between current stress state and it's corresponding "image" stress state at bounding surface, ii) the plastic modulus at the "image" stress state. Thus, the bounding surface plasticity can be viewed as a generalization of the yield surface

plasticity or conventional plasticity when the plastic moduli function with the bounding surface takes such large values through the adoption of certain model parameters that the actual deformation within the bounding surface is dominated by elastic strain and the bounding surface acts as a yielding surface.

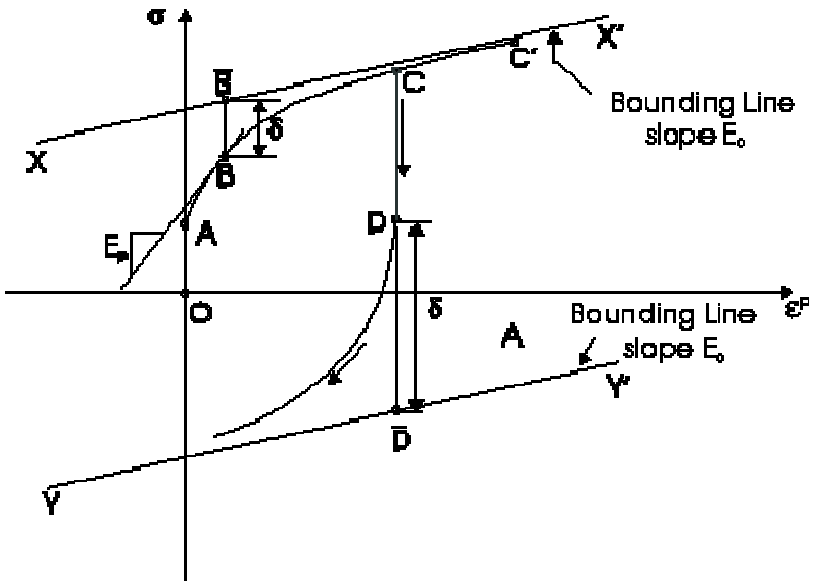

Figure A.1: Schematic illustration of the bounding surface in uniaxial stress-strain space

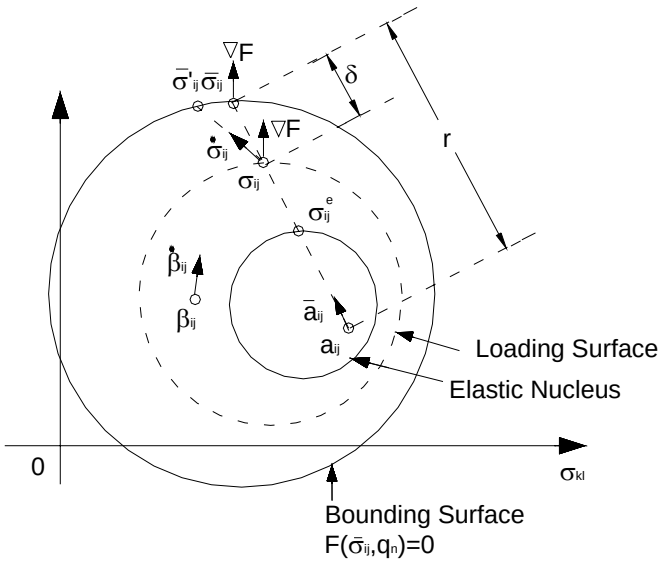

Figure A.2 Schematic Diagram of Bounding Surface and Related Concepts

The total strain rate is decomposed into elastic and plastic parts according to:

$$\dot{\varepsilon}_{ij} = \dot{\varepsilon}^{e}_{ij} + \dot{\varepsilon}^{p}_{ij} \tag{A.1}$$

where a superposed dot indicates the rate; ε_{ij} is the strain component; and the superscripts e and p denote the elastic and plastic parts, respectively. The rate form of elastic equations is given by:

$$\dot{\varepsilon}^{e}_{ij} = C_{ijkl}\dot{\sigma}_{ij} \quad or \quad \dot{\sigma}_{ij} = E_{ijkl}\dot{\varepsilon}^{e}_{ij} \tag{A.2}$$

where the summation convention over repeated indices applies. The fourth order tensor of elastic tangent compliance C_{ijkl} and modulus E_{ijkl} (inverse of C_{ijkl}) are assumed to be functions of the stress tensor σ_{ij} and directional properties. If we define L_{ij} as the loading direction, R_{ij} as the flow direction of plastic strain, and r_n as the direction of the evolution of internal variables, the plastic rate equations of evolution and the total strain rate - stress rate relations for an elastic plastic state can be expressed by (Dafalias, 1986):

$$\dot{\varepsilon}_{ij}^{p} = \langle L \rangle R_{ij} \tag{A3}$$

$$\dot{q}_n = \langle L \rangle r_n \tag{A.4}$$

$$\dot{\varepsilon}_{ij} = D_{ijkl}^{-1} \dot{\sigma}_{ij} \tag{A.5}$$

$$D_{ijkl} = E_{ijkl} - h\langle L \rangle B^{-1} P_{ij} Q_{kl} \tag{A.6}$$

$$Q_{kl} = E_{klrs} L_{rs} \; ; \; P_{ij} = E_{ijab} R_{ab} \tag{A.7}$$

$$B = K_p + L_{ab} E_{abcd} R_{cd} \tag{A.8}$$

$$L = \frac{1}{K_p} L_{ij} \dot{\sigma}_{ij} = \frac{1}{B} Q_{kl} \dot{\varepsilon}_{kl} \tag{A.9}$$

where K_p is the plastic modulus; L is the loading index; $h(L)$ is the Heavyside step function defined as zero at $L = 0$, and the Macauley brackets define the operation of Heavyside step function. L_{ij} is along the gradient of a loading surface $f = 0$ passing through the point σ_{ij} in stress space, i.e.

$$f(\sigma_{ij}, q_n) = 0; \quad L_{ij} = \frac{\partial f}{\partial \sigma_{ij}}; \quad K_p = \frac{\partial f}{\partial \sigma_{ij}} r_n \tag{A.10}$$

A bounding surface in stress space and its stress gradient direction are defined by:

$$\overline{\mathrm{F}}(\overline{\sigma}_{\mathrm{ij}}, \mathrm{q}_{\mathrm{n}}) = 0; \quad \overline{\mathrm{L}}_{\mathrm{ij}} = \frac{\partial \mathrm{f}}{\partial \overline{\sigma}_{\mathrm{ij}}} \tag{A.11}$$

Where a bar over stress quantities indicates their association with $F = 0$, which always encloses the loading surface $f = 0$ or it may contact it at a point tangentially or even become identical with it but never intersects it. The analytical description of the foregoing requires the following steps:

i) A unique "image" stress on $F = 0$ is defined for any σ_{ij} on $f = 0$ by a proper, noninvertible continuous mapping rule as:

$$\overline{\sigma}_{ij} = M_{ij}(\sigma_{kl}, q_n) \tag{A12}$$

which together with Equations (A.10) and (A.11) must satisfy the identity conditions $\bar{\sigma}_{ij} = \sigma_{ij}$ and $\bar{L}_{ij} = L_{ij}$ when the σ_{ij} lies on $F = 0$ in a continuous manner. The identity conditions guarantee that f and F cannot intersect, and hence, they impose restrictions on their relative evolution. Notice that for σ_{ij} inside $F = 0$, $\bar{L}_{ij}$ may be different from L_{ij} in size and/or direction.

ii) For any $\dot{\sigma}_{ij}$ such that $L \geq 0$, a corresponding $\dot{\bar{\sigma}}_{ij}$ occurs at the image stress point due to the change of σ_{ij} and the hardening of $F = 0$ as determined by the q_n. Since σ_{ij} must always remain on $F = 0$, use of Equations (A.4), (A.9) and (A.11) in the consistency condition $F = 0$ yields:

$$L = \frac{1}{K_p} L_{ij} \dot{\sigma}_{ij} = \frac{1}{\bar{K}_p} \bar{L}_{ij} \dot{\bar{\sigma}} \tag{A.13}$$

$$\bar{K}_p = -\frac{\partial F}{\partial q_n} r_n \tag{A.14}$$

in which, K_p is the bounding plastic modulus at the "image" stress $\bar{\sigma}_{ij}$. It is given from Equation (A.14) for known values of r_n.

iii) The actual plastic modulus K_p, instead of being given by Equation (A.10), is related to $\bar{K}_p$ via the Euclidian distance $\delta = \left[(\bar{\sigma}_{ij} - \sigma_{ij})(\bar{\sigma}_{ij} - \sigma_{ij})\right]^{\frac{1}{2}}$ between $\dot{\bar{\sigma}}_{ij}$ and σ_{ij} by an equation of the general form

$$K_p = \hat{K}(\bar{K}_p, \delta, \sigma_{ij}, q_n) \tag{A.15}$$

Such that $\hat{K} > \bar{K}_p$ for $\delta > 0$, $\hat{K} = \bar{K}_p = K_p$ for $\delta = 0$, and $\partial \hat{K} / \partial \delta > 0$. With K_p known from Equation (A.15), Equation (A.9) becomes a restriction on the remaining quantities

for the consistency condition $f = 0$ to be satisfied. Equation (A.15) embodies the salient feature of the bounding surface formulation, namely that plastic deformation may occur within $F = 0$ with a magnitude dependent on δ via the value of K_p.

A.2 Bounding Surface Hypoplasticity

Dafalias (1981, 1986) further advanced the bounding surface concept with another class of constitutive formulations called hypoplasticity. The main distinguishing feature of hypoplasticity is the dependence of the plastic strain rate and the rate of the internal variables on the stress rate direction in addition to the overall dependence on the stress rate. Thus, hypoplasticity defines an incremental nonlinearity of the stress-strain rate relations. In the frame of hypoplasticity, the functions L_{ij}, R_{ij}, r_n and K_p in the previous section depend on the state variables σ_{ij}, q_n and the direction not only on the magnitude of stress rate $\dot{\sigma}_{ij}$, but also on $\dot{\sigma}_{ij} \Big/ \left|\dot{\sigma}_{ij}\right|$. So Equation (A.5) implies incrementally nonlinear relations in the frame of hypoplasticity.

Wang et. Al. (1990) presented a bounding surface hypoplasticity model for sand. It was developed in the space of deviatoric stress ratio (r_{ij}) and mean effective stress (p). The deviatoric stress ratio (r_{ij}) plays a very important role sand behavior and is defined as:

$$r_{ij} = \frac{s_{ij}}{p} \tag{A.16}$$

$$s_{ij} = \sigma_{ij} - p\delta_{ij} \tag{A.17}$$

where σ_{ij} is effective stress components, s_{ij} is deviatoric stress components, p is mean effective stress and δ_{ij} is kronecker delta function.

The isotropic invariants are therefore introduced $J=\left(\frac{s_{ij}s_{ij}}{2}\right)^{\frac{1}{2}}$, $S=\left(\frac{s_{ij}s_{ik}s_{kj}}{3}\right)^{\frac{1}{3}}$, $R=\left(\frac{1}{2}r_{ij}r_{ij}\right)^{\frac{1}{2}}=\frac{J}{p}$, $\cos 3\alpha=\frac{3\sqrt{3}}{2}\left(\frac{S}{J}\right)^{3}$. The α is different from the classic Lode angle. Here, $\alpha=0^0$ and $\alpha=60^0$ correspond to triaxial compression and extension, respectively.

The rate form of $\dot{\sigma}_{ij}$ using Eq. (A.16) becomes:

$$\dot{\sigma}_{ij}=\dot{s}_{ij}+\dot{p}\delta_{ij}=p\dot{r}_{ij}+\dot{p}\frac{\sigma_{ij}}{p} \tag{A.18}$$

Using Equation (A.18) and the decomposition of the elastic strain rate $\dot{\varepsilon}^e$ into deviatoric and volumetric parts $\dot{e}^e$ and $tr\dot{\varepsilon}^e$, respectively, leads to:

$$\dot{\varepsilon}_{ij}{}^{e}=\dot{e}_{ij}{}^{e}+\frac{1}{3}\left(\dot{\varepsilon}_{kk}{}^{e}\right)\delta_{ij}=\frac{1}{2G}\dot{s}_{ij}+\frac{1}{3K}\dot{p}\delta_{ij}=\frac{1}{2G}p\dot{r}_{ij}+\left(\frac{1}{2G}r_{ij}+\frac{1}{3K}\delta_{ij}\right)\dot{p} \tag{A.19}$$

The G and K are incremental elastic shear and bulk moduli.

The incrementally irreversible response is attributed by the two different mechanisms; the first associated with $p\dot{r}$ and the second with $\dot{p}$. Each mechanism will, in turn, produce a deviatoric and volumetric part. Thus, the total plastic strain rate can be written as:

$$\dot{\varepsilon}_{ij}{}^{p}=\left(\frac{1}{H_r}n_{ij}^{D}+\frac{1}{3K_r}\delta_{ij}\right)\left(p\dot{r}_{kl}n_{kl}^{N}\right)+\left(\frac{1}{H}r_{ij}+\frac{1}{3K_p}\delta_{ij}\right)h\left(p-p_m\right)\left\langle\dot{p}\right\rangle \tag{A.20}$$

Where H_r and K_r are plastic shear and bulk moduli, respectively, associated with $\dot{r}_{ij}$; H_p and K_p are plastic shear and bulk moduli, respectively, associated with $\dot{p}$. n_{ij}^{D} is a unit vector in the stress space along the direction of the deviatoric part of $\dot{\varepsilon}_{ij}{}^{p}$ caused by

$\dot{r}_{ij}$, and n_{ij}^N is the associated deviatoric unit loading direction. Both n_{ij}^D and n_{ij}^N depend on the direction of $\dot{r}_{ij}$, thus, introducing the hypoplastic character and incremental nonlinearity of the formulation (Dafalias, 1986). Due to the foregoing dependence, the term $p\dot{r}_{ij}n_{ij}^N$ will always be nonnegative, in contrast to classical plasticity with loading/unloading. However, the values of H_r and K_r change according to a loading criterion. p_m is the maximum value of p experienced in the past loading. Note that the heavyside step function $h(p-p_m)$ and the Macauley brackets $\langle \dot{p} \rangle$ indicate that the plastic mechanism due to $\dot{p}$ operates only when $p = p_m$ and $\dot{p} > 0$.

Stress rate tensor and strain rate tensor is related by Equation (A.21)

$$\dot{\sigma}_{ij} = \Lambda_{ijkl}\dot{\varepsilon}_{ij} \tag{A.21}$$

$$\Lambda_{ijkl} = E_{ijkl} - \frac{p_{ij}{}^{r} \otimes Q_{kl}{}^{p} - p_{ij}{}^{p} \otimes Q_{kl}{}^{r}}{A_r B_p - A_p B_r} \tag{A.22}$$

where

$$E_{ijkl} = K\delta_{ij}\delta_{kl} + G\left(\delta_{ik}\delta_{jl} + \delta_{il}\delta_{jk} - \frac{2}{3}\delta_{ij}\delta_{kl}\right) \tag{A.23a}$$

$$p_{ij}{}^{r} = \frac{2G}{H_r}n_{ij}^D + \frac{K}{K_r}\delta_{ij}; \quad p_{ij}{}^{p} = \left(\frac{2G}{H_p}r_{ij} + \frac{K}{K_r}\delta_{ij}\right)h(p-p_m)h(\dot{p}) \tag{A.23b}$$

$$Q_{ij}{}^{r} = A_p n_{ij}^N - A_r\delta_{ij}; \qquad Q_{ij}{}^{p} = B_p n_{ij}^N - B_r\delta_{ij} \tag{A.23c}$$

$$A_r = \frac{1}{2G} + \frac{1}{H_r}n_{ij}^D n_{ij}^N; \quad A_p = \frac{1}{K_r} \tag{A.23d}$$

$$B_r = \left[\frac{1}{2G} + \frac{1}{H_p}h(p-p_m)h(\dot{p})\right]r_{ij}n_{ij}^N; \; B_p = \frac{1}{K} + \frac{1}{K_p}h(p-p_m)h(\dot{p}) \tag{A.23e}$$

The above hypoplasticity model (Wang, et. al 1990) was developed on the basis of bounding surface ideal and can simulate the sand response under very complex and diversified loading conditions. However this model was not developed within the framework of critical state soil mechanics (Li, et. al., 1999). It also does not capture the some important behaviors of sand, such as shear-induced dilatancy and state dependence of dilatancy.

A.3 Critical State Two-surface Plasticity Sand Model

Manzari & Dafalias (1997) coupled the two-surface formulation of plasticity with the state parameter ψ within the critical state soil mechanics framework to construct a constitutive model for sand in a general stress space. In this model, the operation of the two-surface model in the deviatoric stress-ratio space is as in Wang's (1990) hypoplasticity model but the state parameter is used to define the peak and dilatancy stress ratios of sand. It makes us of a modification to the proposal made by Wood et al. (1994) in that a "virtual" peak or bounding stress ratio is related to the critical stress ratio M by way of ψ. Denoting the bounding stress ratio by M_c^b for compression and M_e^b for extension, and with M_c the critical stress ratio in compression and M_e the critical stress ratio in extension, we can write:

$$M_c^b = \alpha_c^b + m = M_c + k_c^b \langle -\psi \rangle \tag{A-24a}$$

$$M_e^b = \alpha_e^b + m = M_e + k_e^b \langle -\psi \rangle \tag{A-24b}$$

where k_c^b, k_e^b are positive quantities and the Macauley brackets $\langle\ \rangle$ define $\langle -\psi \rangle = -\psi$ if $-\psi > 0$ and $\langle -\psi \rangle = 0$ if $-\psi \le 0$. The word 'virtual' is used because M_c^b or M_e^b is not actually the peak stress ratios that will be reached by the current stress ratios η, but it

changes with ψ until it is met by η at a different value, where it becomes the peak. The effect of α_c^b and α_c^b is the equivalent of a back-stress for a given *m* corresponding to bounding stress ratio in compression and extension and ensuing kinematic hardening in plasticity.

Manzari & Dafalias (1997) defined the phase transform line M^d described in Ishihara et al. (1975) as dilatancy line and assumed it to vary with the state parameter ψ. Similarly, a proposition to formulate the dilatancy lines M_c^d in compression and M_e^d in extension was adopted.

$$M_c^d = \alpha_c^d + m = M_c + k_c^d \langle -\psi \rangle \tag{A-25a}$$

$$M_e^d = \alpha_e^d + m = M_e + k_e^d \langle -\psi \rangle \tag{A-25b}$$

where k_c^d, k_e^d are positive quantities. Equations (A-25) give a dilatancy ratio below M_c or M_e for $\psi < 0$ (denser than critical) and above M_c or M_e for $\psi > 0$ (looser than critical), while $M_c^d = M_c$ and $M_e^d = M_e$ at $\psi = 0$. Also Equations (A-25) introduce the corresponding back-stress dilatancy ratio a_c^d, a_e^d as a function of ψ.

From Equations (A-24) and (A-25), the critical back-stress ratio a_c^c, a_e^c for $\psi = 0$ are defined according to:

$$M_c = \alpha_c^c + m \tag{A-26a}$$

$$M_e = \alpha_e^c + m \tag{A-26b}$$

Equations (A-24, A-25, A-26) interrelate the bounding dilatancy and critical back-stress ratios through ψ.

The yield surface, which appears as a circular cone in stress space with its apex at the origin, is given by the equation (Manzari and Dafalias 1997):

$$f = [(r_{ij} - \alpha_{ij})(r_{ij} - \alpha_{ij})]^{1/2} - \sqrt{2/3}m = 0 \tag{A-27}$$

Where the back-stress ratio deviatoric tensor α_{ij} determines the position of the axis of the cone and the stress ratio scalar variable m determines the 'size' of the cone.

The loading direction, which is normal to yield surface, is given by:

$$L_{ij} = \frac{\partial f}{\partial \sigma_{ij}} = n_{ij} - \frac{1}{3} N \delta_{ij} \tag{A-28a}$$

$$n_{ij} = \frac{r_{ij} - \alpha_{ij}}{\sqrt{2/3}m} \text{ and } N = \alpha_{ij} n_{ij} + \sqrt{2/3}m = n_{ij} r_{ij} \tag{A-28b}$$

where n_{ij} is the unit deviatoric stress-ratio tensor, that is, $n_{ij} n_{ij} = 1$.

The plastic strain rate is given by:

$$\dot{\varepsilon}^p = \langle L \rangle R_{ij} \tag{A-29a}$$

$$R_{ij} = n_{ij} + \frac{1}{3} D \delta_{ij} \tag{A-29b}$$

where R_{ij} is the 'direction' of $\dot{\varepsilon}^p$ consisting of a deviatoric part n_{ij} and a volumetric part $\frac{1}{3} D \delta_{ij}$ with D the dilatancy coefficient. L is the loading index and is defined by

$$L = \frac{1}{K_p} L_{ij} \sigma_{ij} = \frac{1}{K_p} p n_{ij} \dot{r}_{ij} = \frac{1}{K_p} \left[n_{ij} \dot{s}_{ij} - N \dot{p} \right] = \frac{2G n_{ij} \dot{e}_{ij} - KN \dot{\varepsilon}_v}{K_p + 2G - KDN} \tag{A-30}$$

Where K_p is the plastic modulus.

By considering $\dot{\varepsilon}_{ij} = \dot{\varepsilon}_{ij}^e + \dot{\varepsilon}_{ij}^p$, $\dot{e}_{ij}^{\ e} = \frac{\dot{s}_{ij}}{2G}$ and $\dot{\varepsilon}_v = \frac{\dot{p}}{K}$ and manipulation of Equations (A-29) and (A-30) leads to:

$$\dot{\sigma}_{ij} = 2G\dot{e}_{ij} + K\dot{\varepsilon}_v\delta_{ij} - \langle L\rangle\left(2Gn_{ij} + KD\delta_{ij}\right) \tag{A-31}$$

Note that L can be expressed in terms of $\dot{e}_{ij}$ and $\dot{\varepsilon}_v$ as shown in Equation (A-30), one can write Equation (A-31) in the form $\dot{\sigma}_{ij} = E^{ep}_{ijkl}\dot{\varepsilon}_{kl}$ with E^{ep}_{ijkl} the elastoplastic tangent stiffness moduli, used in a numerical implementation.

Hardening variables α_{ij} and m evolving according to

$$\dot{m} = \langle L\rangle\overline{m} \tag{A-32a}$$

$$\dot{\alpha}_{ij} = \langle L\rangle\overline{\alpha}_{ij} \tag{A-32b}$$

The consistency condition $\dot{f} = 0$ together with Equations (A-27) (A-30) and (A-32) implies

$$K_p = -\frac{\partial f}{\partial \alpha_{ij}}\alpha_{ij} - \frac{\partial f}{\partial m}\overline{m} = p\left(n_{ij}\overline{\alpha}_{ij} + \sqrt{2/3}\overline{m}\right) \tag{A-33}$$